ELECTRON TRANSPORT & ION ACOUSTIC DYNAMICS IN LASER-PRODUCED PLASMAS

A Thesis Submitted
to the College of Graduate Studies and Research
in Partial Fulfillment of the Requirements
for the Degree of Doctor of Philosophy
in the Department of Physics & Engineering Physics
University of Saskatchewan

by

Frank Detering

Saskatoon, Saskatchewan, Canada
Spring 2003

PERMISSION TO USE

In presenting this thesis in partial fulfillment of the requirements for a Postgraduate degree from the University of Saskatchewan, it is agreed that the Libraries of this University may make it freely available for inspection. Permission for copying of this thesis in any manner, in whole or in part, for scholarly purposes may be granted by the professors who supervised this thesis work or, in their absence, by the Head of the Department of Physics and Engineering Physics or the Dean of the College of Graduate Studies and Research at the University of Saskatchewan. Any copying, publication, or use of this thesis, or parts thereof, for financial gain without the written permission of the author is strictly prohibited. Proper recognition shall be given to the author and to the University of Saskatchewan in any scholarly use which may be made of any material in this thesis.

Request for permission to copy or to make any other use of material in this thesis in whole or in part should be addressed to:

Head of the Department of Physics and Engineering Physics
116 Science Place
University of Saskatchewan
Saskatoon, Saskatchewan, Canada
S7N 5E2

ACKNOWLEDGEMENTS

I would like to express my gratitude to my supervisor, Professor Andrei I. Smolyakov, for his support and guidance. I thank the fellow members of the Plasma Physics Laboratory for their continuous support and insightful discussions that helped in successful completion of this work.

I am indepted to Prof. W. Rozmus and Prof. R. Sydora and visiting scientist V. Bychenkov and the University of Alberta for their hospitality where part of this work was performed.

A special thanks goes out to my friends at the International Student Advisors Office for their encouragement and assistance throughout my stay in Saskatoon at the University of Saskatchewan.

ABSTRACT

In this thesis laser-plasma processes are studied at transport and ion time scales. In order to study these processes the particle-in-cell code QN-PIC with one spatial dimension and three dimensions in velocity space was developed. Collisional effects are included by a Monte Carlo procedure, and an electric field solver based on the quasineutrality condition has been implemented. This allows long time scale simulations without having to resolve the electron plasma frequency. Collisional heating of the electrons in the laser electric field is one of the major restrictions on the time step in particle-in-cell codes. We have developed a collisional heating procedure that is based on a Langevin equation. It utilizes a Fokker-Planck equation that describes heating time averaged over the laser frequency. This procedure, in conjunction with the fast field solver and procedures to represent collisions, allows simulation of long time scale in laser-plasma interactions without the need to resolve the short time scales to ensure numerical stability and suppress numerical artifacts. We have studied in detail homogeneously heated plasmas and the effects of electron-electron collisions and collisional heating on the electron distribution function. We have suggested a nonlocal, nonlinear heat transport model based on a earlier self-consistent nonlocal transport theory that is formally restricted to small (linearized) temperature perturbations. Our model extends this model to the case of finite temperature perturbations. The model is tested successfully in simulations of hot spot relaxation of an initial temperature distribution that corresponds to the instantaneous release of heat into a spatially Gaussian temperature profile and Maxwellian velocity distributions of the electrons.

In simulations of collisionally heated hot spots we qualitatively describe the effects of non-Maxwellian velocity distributions on the heat flux and the change of the distribution function due to transport in nonheated regions. For the representation of ion dynamics in QNPIC we have conducted studies of the two stream instability with counterstreaming electrons and ions. Predicted growth rates of ion sound waves are recovered and we find it possible to study anomalous heating and resistivity in 1D ion sound turbulence. In laser plasmas ion sound turbulence due to the return current instability is thought to be one of the factors in the reduction of heat flux from hot spots. Since this instability is of kinetic nature it cannot be reproduced by hydrodynamic simulations. Our preliminary results of the return current instability in electron temperature gradients using QNPIC indicate the feasibility of particle codes to treat this problem.

For the analytic description of ion dynamics we have developed kinetic closures of the ion fluid equations that allow a single representation of the dynamics over all regimes of collisionalities. We employ a Chapman-Enskog like procedure for the closure and use a 21-moment representation for the collisional terms which ensure that the classical collisional limit of the transport coefficients is recovered. Ion sound like waves, transverse to a nonlinear perturbation, are investigated in a cold ion fluid model. We demonstrated the applicability of a stability analysis from the study of solitons to an ion sheath and a double layer potential. In case of the double layer we find transverse ion oscillations with phase velocities approaching zero.

Table of Contents

List of Figures

1. Introduction

The sun produces solar energy by means of fusion in its core where reactions have been sustained for several billions of years. Due to the high density and pressure, the centre of the sun is mostly composed of a gas of ions and electrons, commonly called *plasma*. Controlled fusion reactions, as a virtually inexhaustible and safe energy source, have been the object of research of plasma scientists for the last five decades. A possible approache to fusion reactors is inertial confinement of hot plasma. In the inertial confinement fusion (ICF) concept a deuterium-tritium filled target is irradiated by a short pulse of a high energy laser in order to implode the target such that very high density and temperature of the fuel plasma results [1]. Alternative ICF concepts consider ion beams instead of laser irradiation to create the high pressures on the target.

Originally ICF has been the main driving force in laser plasma research. However, the results have inspired other useful applications such as the use of laser plasma as an intense source of X-ray radiation or as a medium for X-ray lasers. For recent results see e.g. [2, 3]. Yet other applications include the possibility of ion acceleration in the high electric fields that are excited in the laser-plasma/solid interaction. Finally, the high-density, high-temperature plasmas encountered in ICF experiments provide means to study equations of state of high-density matter, and are also of great

interest in modern cosmology and stellar physics.

Perhaps one of the most important characteristics of plasmas is the abundance of collective degrees of freedom. This expresses itself in processes like waves, turbulent eddies and shock waves and many other dynamical processes occurring on a multitude of different time scales and length scales. Within the long time and length scales with which this thesis is mainly concerned, the phenomena of interest cover collisional heating, heat transport and ion dynamics. Understanding these processes is important for a number of aspects of laser plasma interaction as shall be explained below, but due to the general formulation they are also of great interest to the wider plasma physics community. Schematically, the interaction physics can be divided into three different layers (see Figure1.1). In most experiments the intensities of the laser in the focal spot are extremely high with electric field strengths of the same order of magnitude as the fields binding the electrons in their atomic orbits. As a result, a surface layer in the irradiated target is immediately ionized and becomes a hot, expanding plasma. The laser energy is deposited in the underdense expanding plasma region (also called the corona) up to the layer where critical electron density $n_c = m_e\omega_0^2/4\pi e^2$ is reached at the critical layer (ω_0 is the laser frequency, m_e the electron mass and e the electron charge), when the plasma frequency which increases with density is equal to the laser frequency. The plasma frequency is given by $\omega_{pe} = (4\pi n_e e^2/m_e)^{1/2}$, where n_e is the electron density and is the mode corresponding to electrostatic oscillations of the electrons. At higher plasma frequency the laser light cannot propagate in the plasma. The electron temperature of the corona is typically of the order of hundreds

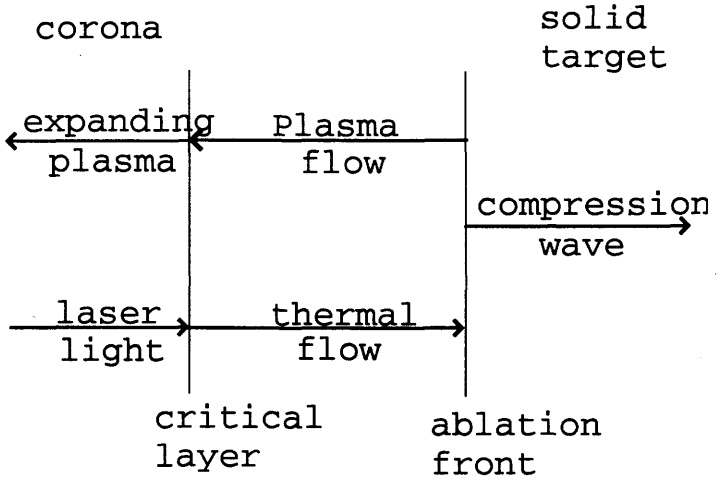

Figure 1.1 Schematic of the three regions that form when a high-power laser irradiates a solid target.

of eV to a few keV.

In the intermediate region between the corona and the solid, energy from the corona is transported conductively or radiatively through a steep temperature gradient (especially close to the ablation front) towards the solid target. Beyond the ablation layer, energy is transported by a compression wave which produces very high densities in the target. The low-density corona can be treated as an ideal gas of fully ionized plasma. In the higher density regions the plasma can become strongly coupled because the interaction energy of the electrons is comparable to thermal energies. In this thesis the results are usually confined to underdense, weakly coupled plasmas such as found in the corona. The physical problems encountered in ICF, discussed in parts in this thesis, can be roughly divided into:

- absorption (laser-plasma interaction)
- transport (i.e. electron energy transport)
- hydrodynamics and stability of laser-plasma interaction

Problems concerning hydrodynamics and stability of the implosion, ignition and burn of the fuel are not considered here. They involve different theoretical techniques and are specific to ICF, whereas the formerly mentioned issues are equally of interest to other branches of plasma physics, e.g. X-ray laser studies.

Most complex physical systems sustain a multitude of phenomena which can evolve on very different time scales. The physics of laser plasma interaction is no exception to this. The propagation of the laser light through the underdense plasma and the various instabilities associated with it occur at very short time scales which are governed by electron dynamics, typically determined by the electron plasma frequency and the laser frequency. Absorption of laser light by electrons is mainly due to slower collisions with ions during the acceleration phase in the laser electric field. Similarly the heat transport is a collisional process. Typically, the collisional time scale is much longer than the electron plasma frequency. Due to the high mass ratio between electrons and ions, ion dynamics evolve on the longest time scale. From these considerations it is obvious that a full description of the system soon becomes untractable, both analytically and also numerically, since simulation runtimes become prohibitively long, e.g. the laser frequency, which is usually the faster time scale, needs to be resolved when the transport

commonly occurs at length and time scales orders of magnitudes longer.

Electrons quiver in the electric field of the laser while the ions remain basically at rest due to their large inertia and the high frequency of the laser. In Chapter 3 we will see that the field oscillations can be averaged and that for moderate fields the heating occurs on the time scale of electron-ion ($e-i$) collisions $\nu_{ei} \propto e^4 Z^2 n_i / m_e^2 v_{te}^3$ where e is the electron charge, Z is the average ionization state, n_i the ion density, m_e the electron mass and v_{te} the electron thermal velocity. Important to note is, that the electron-ion collision frequency has the factor of Z^2 as compared to electron-electron ($e-e$) collisions. In laser plasmas $Z \gg 1$ is typical. This has significant impacts on the velocity distribution of electrons in laser heated plasmas [4, 5]. As will be shown in Chapter 3, the heating occurs faster than the relaxation to Maxwellian velocity distribution due to $e-e$ collisions. The resulting non-Maxwellian distribution functions lead to important changes in the radiation processes, e.g. X-ray lasers which are highly sensitive to the exact form of the velocity distributions. The $e-i$ collision time is also the time scale at which heat transport from the laser hot spots occur. On the transport time scale the plasma remains quasineutral. We exploit this property in these investigations. The energy is mainly transported by fast, energetic electrons. In collisional regimes, collisions with ions determine the limit of the heat flux. However, when collisions are rare the flux is limited by the ambipolar field that is created due to the charge separation (e.g. [6, 7]). To maintain quasineutrality, a return current of colder electrons against the temperature gradient has to occur. We have developed computational and analytic tools to describe the transport and dynamics from collision

dominated to collisionless parameter regimes. Effects of ion motion due to the ambipolar field occur on slower time scales but have to be taken into consideration when long laser pulses are applied [8]. They occur basically during times determined by the ion sound speed $c_s = \sqrt{ZT_e/M_i}$. The instability of ion sound oscillations and the resulting ion turbulence play an important role in the understanding of reduced heat fluxes in experiments or more general aspects of anomalous transport (e.g. [9]).

A powerful tool to complement analytic descriptions of the plasma is computer simulation of the plasma using particles [10, 11]. It is particularly useful for investigating kinetic and nonlinear effects, both of which play important roles in the study of transport and of ion fluctuations in the parameter regimes encountered in laser plasmas. Before being used to interpret new results such simulation codes have to be validated. This is typically done by comparison with theoretical results, e.g. in the parameter regime of classical transport or in the case of small perturbations (density, temperature etc.) where linear theories are a good approximation. Another type of validation is through comparison with other established simulation codes. In this work comparisons are done with codes (Fokker-Planck codes) that numerically solve the kinetic equation for the electrons with collisional terms. These codes are in general more exact, but computationally more complex and less flexible in applications to realistic geometries and the inclusion of other species.

The organization of the thesis is as follows. In Chapter 2 the basic concepts of plasma simulation using particles are presented. The code QNPIC

developed to study laser plasma on transport scales is introduced. Special detail is paid to the implementation of a fast, low noise electric field solver. The problem of absorption of laser light is considered in Chapter 3. A new numerical approach based on a Langevin equation for collisional heating is developed and implemented in QNPIC. QNPIC is then verified in the case of homogeneous (in space) heating against simple theory and previous FP simulation results. Finally, different cases of pulse parameters are investigated for the application in X-ray laser studies [2, 3]. Chapter 4 deals with electron heat transport due to temperature gradients. The classical heat flux model [12, 13] is outlined and limitations due to the assumptions of short collision mean free paths compared to the temperature gradient scale length are highlighted. The heat flux limiter introduced in hydrodynamic simulations is presented and problems with its physical interpretation are discussed. Several commonly cited models in the context of heat flux inhibition [14, 15, 16] are presented that attempt a physical interpretation of the inhibition by introducing the concept of a non-local heat flux. Common features, and physical and numerical problems are compared. The model of Bychenkov [16], which is self-consistent and exact in the case of small temperature perturbations, is used as a validation model for QNPIC simulations of electron transport. Then the case of large temperature perturbations is studied using QNPIC and a nonlocal, nonlinear heat flux based on the Bychenkov model is suggested and successfully tested [17].

Ion dynamics in laser plasmas are studied in the remaining chapters. Beginning in Chapter 5, quasistationary temperature and density profiles in temperature gradients and laser hot spots are found by using QNPIC. Ion

acoustic oscillations are examined next. QNPIC ion dynamics are validated and applicable wavelength regimes are found by calculating the dispersion relation in simple test cases. Applications and further validations by studying two stream instabilities are then performed towards the goal of studying the return current instability in temperature gradients in laser plasmas [18]. Finally, simulation results of the long term evolution of a laser hot spot heated by inverse bremsstrahlung and including ion dynamics are presented. In Chapter 6, the fundamental problem of finding a hydrodynamical representation of ion dynamics that correctly describes kinetic effects due to wave-particle interactions and collisional effects is addressed. The general problems of truncated hydrodynamic representations are discussed and compared with a fully kinetic description. Then a closure (as opposed to a truncation) procedure [19] of the hydrodynamic equations is outlined. Collisional effects, which have been ignored or treated by simple approximations in previous works [20, 19], and were mostly done in the context of magnetic fusion become the focus of this closure. The necessary truncation in the collisional part is motivated and the final closures are compared for a 13-moment truncation [21] and a 21-moment truncation. It is shown that 21 moments are necessary for correct collisional limits, and deviations in the intermediate collisionality regimes are quantified.

A new application of an analytical tool in the study of solitary waves is introduced in Chapter 7. A technique commonly used to investigate the stability of solitary waves to transverse (to the direction of propagation of the solitary wave) oscillations is applied to ion acoustic waves in a plasma sheath which are shown to be stable. The problem is then expanded to

the case of a plasma with two electron distributions with two different temperatures. In this case double layer solutions of potential, density, etc. can occur. Again, the Kadomtsev-Petviashvili formulation is applied to obtain the dispersion relation for transverse ion waves. Results from sheath and double layer configuration are then compared and it is demonstrated that in the double layer case solutions with phase velocities much slower than the ion sound speed occur. Unless otherwise noted, equations in this thesis will be written in cgi units.

2. The PIC Method and Quasineutral Approximation

2.1 Plasma Simulation Methods

For the simulation of complex plasma experiments, fast hydrodynamic simulation codes are used to efficiently describe the long time scale evolution of the plasma system. Such simulations may include complex geometries and sink and source terms like radiation, recombination and ionization that can be described by Monte Carlo type procedures. Electric and magnetic fields are solved from Maxwell's equations where the macroscopic currents and densities act as sources. Hydrodynamic simulation is advantageous since it requires only to evolve averaged quantities like density, flux, temperature etc. in space and time. If, on the other hand, kinetic processes with deviations from a Maxwellian velocity distribution are significant or they are the object of investigation themselves, kinetic simulations have to be employed.

Numerical solution of the kinetic equation with Fokker-Planck (FP) term for collisional processes is the most direct kinetic method and appropriate to investigate basic plasma phenomena in simple geometries. The drawback is the high phase-space dimensionality compared to hydrodynamics and the difficulty to simulate more complex geometries that are neces-

sary to study realistic plasma experiments. In this work results from FP simulation results [22, 17, 23] will be used as a validation for the developed simulation code.

Another technique is the so-called δf-method. This method is much in the spirit of the analytic closure developed in Chapter 6. The one particle velocity distribution is divided into a Maxwellian bulk, which carries the information of density, flow and temperature as functions of time and space, and into a remainder δf, which contains all the kinetic information. δf is represented by marker particles, which are evolved in time in a similar way as in full particle codes described below. Attempts have been made to apply the δf-method to electron transport with the inclusion of collisions [24, 25]. However, due to intrinsic numerical problems in collisional δf methods, this research has not been further pursued. In this thesis, the so-called particle-in-cell (PIC) method [10, 11] is used and extended with an electric field solver for quasineutral plasmas and a Langevin procedure for the process of inverse bremsstrahlung heating of electrons. These significantly accelerate the simulation compared to conventional PIC codes.

2.2 Particle-in-cell Principle

The philosophy of simulating plasma systems using particle models is to follow a large number of charged particles in their self-consistent electric (and magnetic) fields. Although straightforward, this approach soon reaches computational limitations requiring the use of clever approximating numerical techniques. The main limitation arises from the huge number of particles

encountered even in low density laboratory plasmas (appr. 10^{12}cm^{-3}) and even more so in inertial confinement fusion plasmas (up to 10^{27}cm^{-3}). In simulations, a much smaller number of particles is used. Keeping the number of real particles in mind, the particles in simulations can be viewed as "superparticles" representing many particles of the real plasma or one can alternatively view the simulation as a very small representative region of the plasma under investigation. In standard electrostatic PIC (for a review see e.g. Dawson [10] or Langdon, Birdsall [11]), electric fields are computed using Poisson's equation. In turn, the charge density in Poisson's equation is determined from the particle position. The force on particle i is then the sum of the contributions to the electric field from all the other particles

$$F_i = q_i \sum_{j,i \neq j} E_{ij}, \tag{2.1}$$

where q_i is the charge of particle i and E_{ij} is the electric field of particle j acting on particle i. Equation(2.1) implies a computational effort for each time step that scales with N^2 if N is the number of particles. It is obvious that even with the fastest computers this approach is futile when considering simulations with N of the order of 10^6 as will be necessary for warm and inhomogeneous plasmas.

Another problem implicit in this approach is the overemphasis of collisions. Since computer particles represent many electrons or ions, the electrostatic forces between the model particles and the associated collisional effects are much greater. Fortunately, it turns out that a simple procedure, the so-called finite-size particle (FSP) method, reduces collisions substan-

tially and at the same time allows the use of faster force calculations. FSP are realized by interpolating the particle properties (charge, current and kinetic energy) on a grid which is about the size of the particle (see Figure2.1). Usually, the particles are considered pointlike within the simulation and the finite size effects are realized by using a shape function $S(x - x')$. Then, the grid charge density ρ_g would be calculated from the simulation particle density ρ_p by

$$\rho_g(x,t) = \int dx' S(x - x')\rho_p(x',t). \tag{2.2}$$

The simulation particle density is

$$\rho_p(x,t) = \sum_i \delta(x - x_i(t)), \tag{2.3}$$

where $x_i(t)$ is the position of the i-th particle. The electric field can then be conveniently computed as a grid function, e.g. from Poisson's equation. Assuming that we use far less grid points than particles, the field calculation is considerably accelerated. Typically, Fourier transform methods are employed with great success. The electric field is then, in turn, interpolated to the particle position. This procedure averages charges and fields over spatial ranges of the order of the particle size.

In conclusion, we have finite size particles as a natural consequence of using grids for interpolation. Since the grid is typically much larger than the average particle spacing, two-particle interactions on scales shorter than the grid spacing are effectively suppressed. This means that the collision frequency is substantially reduced and the typical particle-in-cell simulation is a collisionless plasma simulation. To include electron-ion and electron-

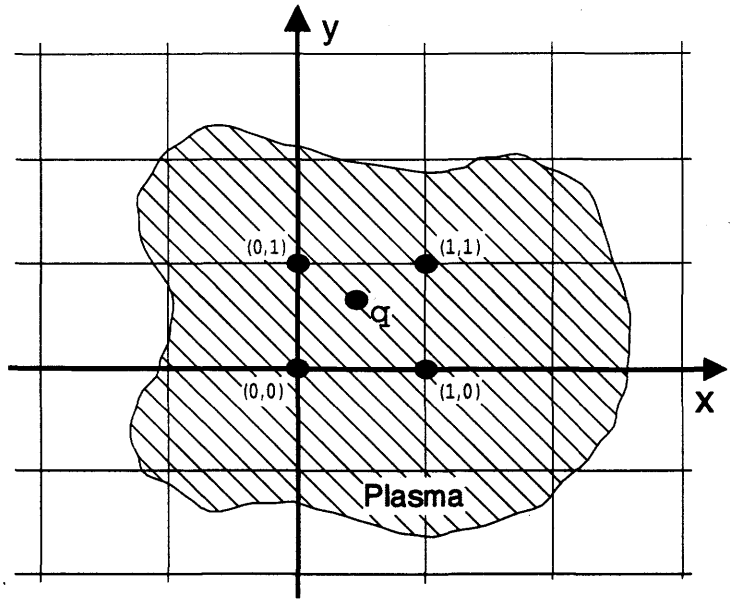

Figure 2.1 A grid is laid over the plasma region. Plasma density, drift, temperature and heat flux are measured on it to obtain the electric field on the grid. Charge and velocity of a charged particle q will typically be distributed to the nearby grid points (0,0), (1,0), (0,1), (1,1). The force on q will be obtained from the same points.

electron collisions we have used a binary collision procedure [26, 27] that has been implemented by Kirkby [28].

2.3 Quasineutral Electric Field Solver

Standard technique for electrostatic field solvers in particle codes is to solve Poisson's equation. The charge source term is determined from the particle positions, with the charge obtained by interpolating onto the grid. This works well if time scales comparable to the electron plasma frequency

are of interest and if there is substantial charge separation. However, for transport studies, time and space scales are much longer, and the plasma maintains quasineutrality throughout, i.e. $|n_e - n_i| \ll n_i$. The encountered problems for stability with respect to electron plasma oscillations are that the time step must be less than $2\omega_o^{-1}$. In transport problems the time scales of interest are usually the electron-ion collision time or the ion sound time scale. These scales may be several orders of magnitude larger, making explicit schemes too time consuming. This can be circumvented by implicit algorithms, but a fundamental difficulty remains due to the quasineutrality of the plasma. In particle codes where electrons and ions are represented by macroparticles a direct calculation of the electric field by Poisson's equation would lead to a large statistical noise. Chen [29] notes on page 66 that, "In a plasma, it is usually possible to assume $n_e = n_i$ and $\nabla \cdot \mathrm{E} \neq 0$ at the same time. This is a fundamental trait of plasmas, one which is difficult for the novice to understand. *Do not use Poisson's equation to obtain E unless it is unavoidable!*". For the simulations presented here we employ an approach by Joyce [30]. The electric field is essentially determined from the electron momentum conservation equation requiring quasineutrality.

2.3.1 Unmagnetized One-Dimensional Plasma

We start out with the electron momentum equation

$$-\grave{e}E = \frac{1}{n_e}\frac{\partial P_e}{\partial x} + \nu_e m_e u_e + \frac{1}{n_e}\frac{\partial}{\partial t}(n_e m_e u_e). \tag{2.4}$$

Here P_e is the xx-component of the total stress tensor, which includes temperature and stresses associated with flows, u_e is the electron mean velocity and ν_e is the mean electron momentum transfer collision frequency. Defined as integrals over the electron distribution they are as follows,

$$P_e(x,t) \equiv \int dv m_e v^2 f_e(x,v,t), \tag{2.5}$$

$$n_e u_e(x,t) \equiv \int dv v f_e(x,v,t), \tag{2.6}$$

$$n_e \nu_e(x,t) \equiv \int dv \nu(x,v,t) f_e(x,v,t) = R_{ei}. \tag{2.7}$$

Since we are interested in slow and long time scale phenomena compared to the motion of the hot electrons, i.e.

$$\omega \ll k v_{te}, \tag{2.8}$$

where v_{te} is the electron thermal velocity, the electron inertia term $\propto \frac{\partial}{\partial t}$ is neglected. By doing this, electron plasma oscillations are no longer resolved. Furthermore, we make use of the quasineutrality condition that $n_e \approx n_i$ and replace the electron density n_e by the ion density n_i. The resulting equation that we use to determine E in the simulation is

$$-eE = \frac{1}{n_i} \frac{\partial}{\partial z} (n_i T_e) + R_{ei}, \tag{2.9}$$

where R_{ei} is the rate of change in momentum due to the random collisions. Using initial density and temperature perturbations, we will validate that quasineutrality is maintained to a noise level of less than 10%.

2.4 Diagnostics

For any physical experiment it is not only important to use the proper physical model and experimental setup for the specific problem, but also to measure the relevant physical parameters in an economical way to facilitate the data analysis. Much the same holds true for computer simulation. In the special case of PIC simulation, the accessible physical quantities are the full phase-space of all particle positions and velocities. For most of the problems discussed in this thesis particle numbers of the order of 10^6 are used. Saving all the information of one spatial and three velocity components in double precision for each particle each time step (typically of the order of 10^4) is clearly not an option. Nor is it particularly easy and insightful to look at the full phase space in transport problems. For most problems the relevant physical variables to describe the evolution of the plasma system are the thermodynamical and hydrodynamical variables, density, flow (or current), temperature, heat flux and electrostatic field and field energy. Also, to study the kinetic effects, it is useful to look at the velocity distribution function of the electrons, both the isotropic part $f_e^0(v)$ and the anisotropic part $f_e^1(v, v_x)$. The separation of isotropic and anisotropic parts of the distribution function is explained below. For this we assume that the velocity distribution is sufficiently well represented with

an expansion in Legendre polynomials P_l,

$$f(v,\mu) = \sum_{l=0}^{\infty} f_l(v) P_l(\mu), \tag{2.10}$$

that is truncated at the first anisotropy $l = 1$ with $P_1(\mu) = \mu$, where $\mu = v_x/v$.

In addition, in the study of ion waves, it is useful to have a reduced representation of the phase space to obtain a qualitative picture of the time evolution and possible onset of particles trapping etc. This is done by following the position and velocity (in x direction) of a few hundred particles which are thought to represent part of the phase space. The purpose of all these diagnostics is not only to analyze the system but also to save file I/O time and disk space in doing so. Since most of these operations scale with the number of particles (they are typically defined as integrals of the distribution function which becomes the sum over all particles), they are only performed as frequently as necessary to resolve the time scale of the phenomena of interest. Global quantities (quantities integrated over the simulation region) are typically calculated approximately every 10 time steps to detect e.g. numerical instabilities while the simulation is running. The distribution function is typically calculated only a few times during the whole simulation since the final state (or the state at a particular time, e.g. when the laser is turned off) is of most interest.

2.4.1 Global Hydrodynamic Variables

Global hydrodynamic variables are plasma parameters that are calculated by taking moments of the distribution function or electric potential over the whole spatial simulation region. For a qualitative picture of the stability, e.g. energy evolution (conservation in closed systems) of the system, it is useful to collect data of the total kinetic energy of all species and total electrostatic energy. These are simply calculated every specified number of time step by

$$T_s \equiv \frac{m_s}{2} \sum_{i=1}^{n_p} v_{si}^2, \tag{2.11}$$

for the temperature of species s and

$$ESE \equiv \sum_{j=1}^{n_g} |E_j^2|, \tag{2.12}$$

for the electrostatic energy where n_g is the number of grid points. These are the discrete forms used in the computations. The original integral forms are,

$$T_s \equiv \frac{m}{2} \int v^2 f(v) d^3v, \tag{2.13}$$

for temperature and

$$ESE \equiv \int_0^L |E|^2 dx. \tag{2.14}$$

2.4.2 Local Hydrodynamic Variables

Local hydrodynamic variables are plasma parameters that are calculated locally, as moments of the distribution function (density etc.) or electric

potential, at each grid point in the simulation region. For transport and wave studies the hydrodynamical moments are needed locally to determine wave structures and especially gradients for transport investigations. They are collected by the same weighting scheme as is used for the particle mover. Since the electric field is determined from fluid moments, additional computational burden is imposed by the collection of density, flow, temperatures and electric field. The density is calculated as follows

$$n_x = m_e \sum_{i=1}^{n_p} S\left(x^i - x\right), \tag{2.15}$$

the flow as,

$$n_x u_x = m_e \sum_{i=1}^{n_p} v_x^i S\left(x^i - x\right) \tag{2.16}$$

where u_x is the local mean velocity and S is the shape function and is determined by the interpolation scheme (2nd order in all simulations here). Temperature and heat flux are calculated analogously.

2.4.3 Electron Distribution Function (EDF)

Detailed knowledge of the EDF is important for the study of collisional heating of plasmas and stability problems in electron temperature gradients. Usually, it is sufficient to assume that the distribution function can be adequately expressed by a two term expansion with a purely isotropic part $f_0(v)$ and the first anisotropic part $\mu f_1(v)$, where $\mu = v_x/v$ is in the direction of the gradients of the inhomogeneities (x in the one dimensional simulations considered here). In the isotropic case $f_0(v)$ is determined by counting

particles within bins on a velocity grid. The two-dimensional distribution $f_e(v, v_x)$ is taken in the same way with a velocity grid in v and v_x. Due to the way the EDF is determined, it is actually $f_e(v)v^2$ that is measured since this corresponds to the actual number of particles in a particular velocity interval for three-dimensional velocity space, and similarly for $f_e(v, v_x)$. As a consequence, the distribution is burdened by lower counts at low velocities and a higher noise level in this regime. The isotropic and anisotropic part are extracted from $f_e(v, v_x)$ by integrating over v_x with the appropriate Legendre polynomial ($P_0 = 1$ and $P_1 = \mu$).

2.4.4 Phase-space Evolution

For the studies of ion sound dynamics with mobile ions it is useful to mark a certain amount of the ions (typically about 200 particles), and write out the array of doublets (x, v_x) in certain time intervals. This does not allow any quantitative analysis, but it is possible to obtain a visualization (if all doublets are plotted on the x, v_x-plane) of the dynamics of certain parts of phase space, and point out possible particle trapping or important regimes (in phase-space) for instabilities.

2.5 Experimental Results

To illustrate the mechanism of the model and verify that the quasineutrality condition is indeed maintained, we have considered some simple test problems.

2.5.1 Plasma Expansion

The first example shows a plasma driven by a density perturbation. Electrons and ions are all distributed with constant temperature. The initial density is

$$n(x) = \begin{cases} n_0 & \text{if } x < L/2 - \Delta \text{ or } x > L/2 + \Delta \\ n_0 + \delta n & \text{if } L/2 - \Delta \leq x \leq L/2 + \Delta \end{cases}, \tag{2.17}$$

where L is the length of the periodic system. Figure (2.2) shows two

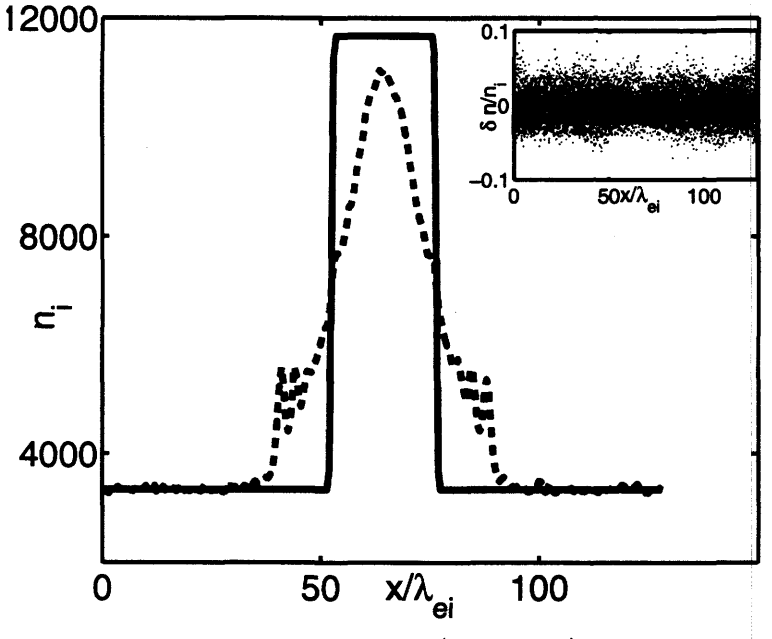

Figure 2.2 Ion density at $t = 0$ (solid line) and at $t = 50\tau_{ei}$ (dashed line). The inlet shows $\frac{(n_i - n_e)}{n_i}$ overlaid over the whole simulation period of $\approx 300\tau_{ei}$.

snapshots of the ion density. The inlet demonstrates that the deviation of quasineutrality is never larger than about 5%. In this simulation, ions

are initially cold. The results show clearly that the algorithm maintains quasineutrality even in the presence of strong density gradients. This configuration will be reused in the section determining the dispersion of ion acoustic waves within this simulation model since it is a convenient method to excite all modes within the system.

2.5.2 Thermal Equilibration/ Thermal Expansion

This example demonstrates a plasma solely driven by a temperature perturbation. Here, only a simple check for quasineutrality is performed. In Chapter 4, this problem will be investigated in detail to understand the physics of nonlocal transport. The initial electron temperature profile is given by

$$T_e(x) = T_0 + \delta T \exp\left(-\frac{x^2}{\lambda^2}\right). \tag{2.18}$$

Ions are initially cold. Figure (2.3) shows two snapshots of the electron temperature. It is a periodic system and relaxes towards a constant temperature throughout. The expulsion of particles from the hot region can be seen in Figure (2.4). It should be pointed out that the large amount of expulsion during this small time is due to the small ion to electron mass ratio ($\frac{m_i}{m_e} = 200$) used in this simulation. A more realistic mass ratio results in less density perturbations and justifies the use of fixed ions ($m_i \to \infty$) for the investigation of heat flux from the hot spot. The inlet in Figure (2.4) demonstrates again that quasineutrality is maintained to about 5% during the simulation.

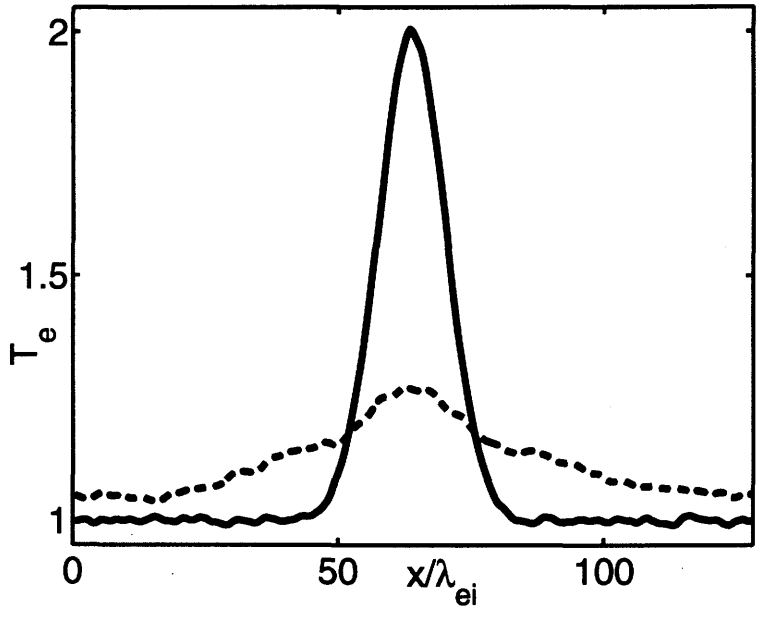

Figure 2.3 Electron temperature at $t = 0$ (solid line) and at $t = 50\tau_{ei}$ (dashed line).

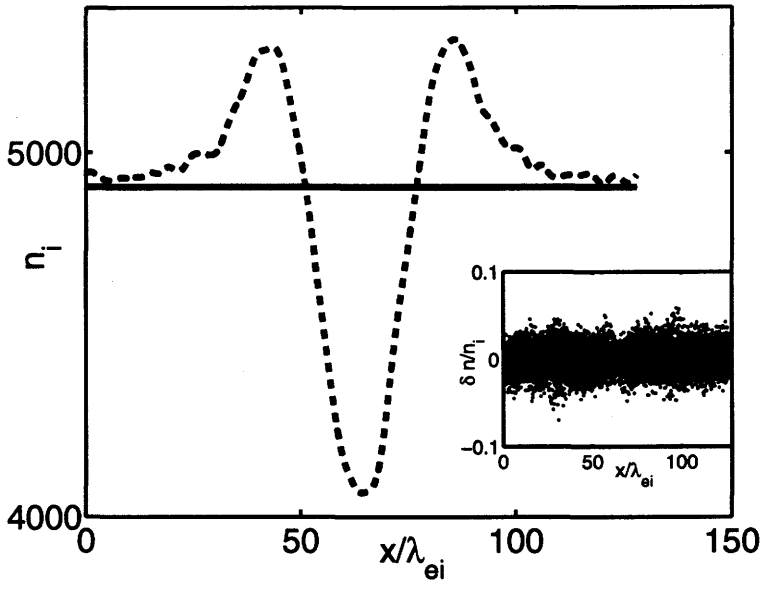

Figure 2.4 Ion density at $t = 0$ (solid line) and at $t = 50\tau_{ei}$ (dashed line). The inlet shows $\frac{(n_i - n_e)}{n_i}$ overlaid over the whole simulation period of $\approx 300\tau_{ei}$.

3. Langevin Representation of Laser Heating in PIC Simulations

3.1 Absorption Processes

Absorption of laser light by the plasma is the main mechanism of energy transfer from beam to plasma, which in turn drives transport and the dynamic evolution of the plasma. Therefore, a detailed knowledge of the absorption process is essential for a correct description of the physics of a laser-plasma system. Absorption leads to the dissipation of energy of the laser electric field into (kinetic) energy of electrons. Ions are considered motionless at the timescale of heating in the laser beam.

In a collisional plasma, the quivering motions of the electrons in the oscillating electric field is converted into energy of random (thermal) motions of the electrons due to collisions of electrons with ions during the oscillations. This classical absorption is also called inverse Bremsstrahlung (IB) because it is the inverse process of an electron-ion collision when the electron looses energy and a photon is emitted. In collisionless plasmas absorption can occur through collective plasma motion because an obliquely propagating laser in an inhomogeneous plasma excites an electron plasma wave near the critical density. This process of resonance absorption is also called linear mode conversion. Closely related are effects of density changes due to the

ponderomotive force and hot electron generation. Parametric instabilities are another absorption mechanism which causes stimulated scattering and generation of high-energy electrons.

3.1.1 Resonant Absorption

At high laser intensities I and long laser wavelengths λ_0, resonance absorption dominates collisional absorption. In particular, its importance increases as $I\lambda_0^2$ increases, and resonant absorption becomes dominant when $k_0^{-1} = \lambda_0/2\pi \approx L$, where L is the density gradient scale length. Obliquely propagating light excites electron plasma waves when it reaches the critical layer, where $\omega_0 = \omega_{pe}$. Here, the electromagnetic mode is converted into a electron plasma mode. Further scattering of electrons on the plasma waves and rare collisions lead to heating of the plasma. Due to the resonant nature of the interaction few electrons (so called hot electrons) gain much higher energies than the background electrons. It should be emphasized, that for resonance absorption to occur, a density gradient needs to be present and it is possible only for p-polarized light, meaning that the electric field of the light lies in the plane of incidence and $\mathbf{E} \cdot \nabla n_e \neq 0$.

3.1.2 Parametric Instabilities

In general, parametric instabilities are three-wave coupling and transfer of energy and momentum from a pump wave (here laser electromagnetic (em) mode) to two other modes. A detailed review of parametric instabilities can be found in [31]. In an unmagnetized plasma three fundamental modes have to be considered: em modes (laser light), plasmons (electron

plasma waves) and phonons (ion sound waves). The former two modes are high frequency modes, whereas the latter is a low frequency mode. The transfer of energy and momentum in the three-mode coupling can follow any of the following six paths:

i. photon $\rightarrow$ photon + plasmon

ii. photon $\rightarrow$ photon + phonon

iii. photon $\rightarrow$ plasmon + plasmon

iv. photon $\rightarrow$ plasmon + phonon

v. plasmon $\rightarrow$ photon + phonon

vi. plasmon $\rightarrow$ plasmon + phonon

The processes (i.,ii.) are called stimulated Raman and stimulated Brillouin scattering respectively. The processes (iii.,iv.) lead effectively to dissipation of energy into the plasma. Process (v.) is related to radiation loss of the plasma. In the case of resonance absorption, the em mode couples to a plasma mode, due to the density gradient created by the expanding plasma. Three-wave coupling is closely related to this, and the coupling occurs due to a density gradient caused by ion density fluctuation (ion sound wave) or an existing electron density fluctuation. Unlike parametric instabilities and resonance absorption, collisional absorption does not require density gradients and is always present in laser plasma interactions.

3.1.3 Inverse Bremsstrahlung

In laser-plasma interaction at low laser intensities, the main heating mechanism is through collisional absorption of the laser radiation or inverse bremsstrahlung (IB). Heating occurs through randomization of the energy acquired by the laser electric field in electron-ion collisions. Typically, the laser frequency is much larger than the electron-ion collision frequency. This allows an averaging of the electron kinetic equation over the laser period and leads to a kinetic equation, that describes the development of the distribution function on the collisional time scale. First investigations of the evolution of the electron velocity distribution function towards a self-similar state appeared in the papers of Langdon [4] and Jones [32]. Using different methods, they concluded that the electrons in a homogeneous plasma, evolving under the influence of an external HF electromagnetic field and undergoing electron-ion collisions, evolve towards a self-similar distribution. In this state, the temperature (i.e. the average kinetic energy of the electrons) increases in time, but the shape of the distribution function remains unchanged. Self-similar states have attracted attention by many plasma physicists especially in the study of transport as an alternative to a Maxwellian equilibrium distribution, in situations where the latter cannot be reached. Balescu [33] extended the work to show that the ions are also represented by a self-similar distribution, which is exactly Maxwellian.

3.2 IB Heating Equation

Collisional absorption of laser irradiation or inverse Bremsstrahlung (IB) is the main mechanism of laser-plasma interaction at short wavelengths and moderate intensities. It leads to heating of the plasma and non-Maxwellian velocity distribution functions. The starting point is the kinetic equation:

$$\frac{\partial f}{\partial t} - \frac{e}{m_e}\mathbf{E}\cdot\frac{\partial f}{\partial \mathbf{v}} = A\frac{\partial}{\partial \mathbf{v}}\cdot\left[\frac{v^2\mathbf{I}-\mathbf{vv}}{v^3}\cdot\frac{\partial f}{\partial \mathbf{v}}\right] + C_{ee}(f), \tag{3.1}$$

where $A = \nu_{ei}v^3$. The presence of a HF external electric field is represented by

$$\mathbf{E}(t) = \mathbf{E}_0\cos(\omega_0 t), \tag{3.2}$$

with amplitude and frequency strictly constant, where $\nu_{ei} = 4\pi Ze^4 n\ln\Lambda/m_e^2v^3$ is the electron-ion collision frequency. $\ln\Gamma$ is the standard Coulomb logarithm, where $\Gamma = \lambda_D/r_0$ represents the maximum impact parameter in units of the closest approach r_0 averaged over a Maxwellian distribution. For later use the quiver velocity of electrons in the external field is defined as

$$\mathbf{v}_E(t) = \frac{e}{m_e\omega}\mathbf{E}_0\exp(-i\omega t). \tag{3.3}$$

A full derivation of the kinetic equation in the weak coupling (Landau) approximation of a fully ionized plasma in a high-frequency electric field can be found in chapter 8 of Ref.[34] for example, and the subsequent derivation of a self-similar solution in [33].

Here, we follow a simple expansion (see e.g. Shkarovsky[35]) in Legendre polynomials making use of the fact that they are eigenfunctions of $e-i$

collision operator. The first two equations are

$$\frac{\partial f_0}{\partial t} - \frac{eE}{m_e}\frac{1}{3v^2}\frac{\partial}{\partial v}\left(v^2 f_1\right) = C_0, \tag{3.4}$$

$$\frac{\partial f_1}{\partial t} - \frac{eE}{m_e}\left(\frac{\partial f_0}{\partial v} + \frac{2}{5v^3}\frac{\partial}{\partial v}\left(v^3 f_2\right)\right) = -\frac{2A}{v^3} f_1 + C_1. \tag{3.5}$$

Langdon [4] truncates the expansion at f_1. This is valid in the limit $v_{E0}/v_t \ll 1$. Also, the contribution of $e-e$ collisions to the anisotropic part of the distribution function C_1 is neglected. We assume that the time dependence of f_1 is dominated by oscillations at the laser frequency ω to obtain

$$f_1(v) = \frac{eE}{m_e}\frac{\partial f_0}{\partial v}\left(\nu_{ei} - i\omega\right)^{-1}. \tag{3.6}$$

Substituting into the equation for f_0 and taking the real part results in the IB kinetic equation:

$$\frac{\partial f_0}{\partial t} = A\frac{v_E^2}{6v^2}\frac{\partial}{\partial v}\left(\frac{g}{v}\frac{\partial f_0}{\partial v}\right), \tag{3.7}$$

where $v_E = eE_0/m\omega$ is the quiver velocity of the electrons in the laser electric field and g is defined as

$$g(v) = \left[1 + \frac{\nu_{ei}(v)^2}{\omega^2}\right]^{-1}. \tag{3.8}$$

The power absorption is calculated from

$$\langle J_1 E\rangle = \frac{\Re}{2}\left[-eE_0\frac{2}{3}\int_0^\infty dv v^3 f_1(v)\right], \tag{3.9}$$

which becomes

$$\langle J_1 E \rangle = -\frac{4\pi}{3} A n_e m_e v_E^2 \int_0^\infty dv \frac{\partial f_0}{\partial v} g(v). \tag{3.10}$$

Usually, one assumes $\omega \tau_{ei} \gg 1$ for all electrons, such that collisions are a perturbation on the entire distribution function. In this case $g = 1$, which we assume for the rest of this work, since the laser frequency is not retained as a parameter in the simulation. It is this equation that we solve using a stochastic formulation. The IB heating equation above has a non-stationary self-similar solution,

$$f_0(v,t) = N(t) \exp\left(-\frac{v^5}{v_t(t)^5}\right) \tag{3.11}$$

where $N(t)$ is a normalization constant and $v_t(t) = \left(v_{t0}^5 + \frac{25}{6} A v_E^2 t\right)^{\frac{1}{5}}$. In Equations (3.7)-(3.11) the total velocity, v, is in the range $v \in [0, \infty)$.

In addition to validating the self-similar solution, another important test of the algorithm is to achieve the correct heating rate. Calculating $< v^2 >= \int_0^\infty dv v^4 f(v)$ from Equation (3.7), we obtain the heating rate $\partial < v^2 > / \partial t$. It turns out that it only depends on the distribution function at $v = 0$ and is given as

$$\frac{\partial < v^2 >}{\partial t} = \frac{A v_E^2}{6} f(v = 0, t) \tag{3.12}$$

Langdon [4] also shows distribution functions in the case where C_0, $e-e$ collision term, is accounted for in numerical calculations. He makes no at-

tempt, however, to prescribe a fit for the description of the distribution function with the parameter $\alpha = Zv_E^2/v_{th}^2$, which is known as the Langdon parameter. Qualitatively, it is clear, that in the case of small α, $e-e$ collisions dominate and will force the distribution to remain equilibrium Maxwellian and in the case of large α the distribution is supermaxwellian self-similar solution as discussed above. An analytic theory of the general case has not been developed. Matte and Co-workers [5] have studied the mixed case extensively with numerical Fokker-Planck simulations. The results suggest that the general solution is fitted best with self-similar distribution of the form

$$f_m(v,t) = C_m \exp\left[-(v/v_m)^m\right], \tag{3.13}$$

with the normalizations

$$v_m^2 = \frac{3T}{M_e}\frac{\Gamma(3/m)}{\Gamma(5/m)},$$

and

$$C_m = \frac{n}{4\pi}\frac{m}{\Gamma(3/m)v_m^3}.$$

Γ is the usual generalization of the factorial. Without IB heating, the solution is Maxwellian ($m = 2$) and with only IB heating the solution is $m = 5$. Matte [5] derives the following interpolation formula from comparison with FP simulations:

$$m(\alpha) = 2 + \frac{3}{1 + 1.66/\alpha^{0.724}}. \tag{3.14}$$

The heating procedure for PIC simulations developed in this chapter will be checked against these predictions.

The departure from a Maxwellian distribution function can lead to dramatic changes in the transport properties of the plasma. Therefore, for detailed numerical studies, heating has to be properly included in any transport simulation code. In particle-in-cell (PIC) codes, this can be achieved by explicit inclusion of the oscillating laser electric field and collisions [36]. The main disadvantage of this approach is the introduction of the laser time scale, which is commonly much smaller than collisional time scales. To study transport phenomena, a different approach is needed, which makes it feasible to run the simulation over many collisional times.

3.3 Langevin Equation

In this section, the required connection between the Langevin and Fokker-Planck equations are presented. The Fokker-Planck equation gives the time evolution of the probability density function in the velocity space. Every Fokker-Planck equation is equivalent to a corresponding Markov process, which can be formulated as a stochastic differential equation, from here on called Langevin equation [37, 38]. This process can then be directly translated into an algorithm for a particle simulation. The following description of the IB heating is included in QNPIC.

The Langevin equation is a stochastic differential equation of the form:

$$\frac{d\boldsymbol{v}}{dt} = \boldsymbol{A}(\boldsymbol{v},t) + \underline{\widetilde{\boldsymbol{B}}}(\boldsymbol{v},t)\cdot\xi(t), \tag{3.15}$$

where $\boldsymbol{\xi}(t)$ is a rapidly fluctuating random term, describing the stochastic heating or diffusion. Generally, one requires $\boldsymbol{\xi}(t)$ to be a white noise signal with

$$< \xi_i(t) >= 0, \tag{3.16}$$

$$< \xi_i(t)\xi_j(t') >= \delta(t-t')\delta_{ij}, \tag{3.17}$$

and <> denotes the ensemble average. In this work, we use Ito's definition of the stochastic integral [37]. With this definition it can be shown that Equation (3.15) is equivalent to a Fokker-Planck equation of the form

$$\frac{\partial f(\boldsymbol{v},t)}{\partial t} = -\frac{\partial}{\partial v_i}\left[A_i(\boldsymbol{v},t)f(\boldsymbol{v},t)\right] + \frac{1}{2}\frac{\partial^2}{\partial v_i \partial v_j}\left[B_{ij}(\boldsymbol{v},t)f(\boldsymbol{v},t)\right], \tag{3.18}$$

where i,j are summed over and $B_{ij} = \widetilde{B_{il}}\widetilde{B_{lj}}^{\mathsf{T}}$.

3.4 Heating Operator

The kinetic equation describing the IB heating resembles an isotropic electron-electron collisional term and can formally be written as a Fokker-Planck equation. Next, we outline the procedure for converting Equation (3.7) into the Fokker-Planck form, and then show how the corresponding Langevin equation can be used for particle simulation. The Langevin equation has long been used to model diffusion phenomena and has previously been successfully implemented to model electron-electron collisions in their linearized form [39]. Equation(3.7) is formally a diffusion equation in velocity and has a form, which is very similar to isotropic electron-electron collisions. When spherical coordinates with total velocity v are used, there

is no angular dependence. Normalizing time to the $e-i$ collision time (for $T = T_0$ background temperature) it is:

$$\frac{\partial f}{\partial t} = v^3 \frac{v_E^2}{6v^2} \frac{\partial}{\partial v} \left(\frac{1}{v} \frac{\partial f}{\partial v} \right). \tag{3.19}$$

To make the transition to the Langevin equation suitable for the particle code, we have to determine "good" choices for vector A and matrix B in Equation (3.15) that do not contain angular dependence and lead to a simple form in cartesian coordinates that will be used in the code. The main step is to rewrite the above equation as

$$\frac{\partial f}{\partial t} = \frac{1}{v^2} \frac{\partial}{\partial v} \left(\frac{Cv^2}{v^3} \frac{\partial f}{\partial v} \right), \tag{3.20}$$

with $C = v_E^2/6$ and compare with the FP equation

$$\frac{\partial f}{\partial t} = \nabla \cdot \left(-\boldsymbol{A} f + \frac{1}{2} \nabla \cdot \boldsymbol{B} f \right). \tag{3.21}$$

We require the angular contributions of the outer divergence to vanish and in this case the FP equation is of the form

$$\frac{\partial f}{\partial t} = \frac{1}{v^2} \frac{\partial}{\partial v} \left(v^2 \left\{ -\boldsymbol{A} f + \frac{1}{2} \nabla \cdot \boldsymbol{B} f \right\} \right). \tag{3.22}$$

Comparing Equation(3.20) and Equation(3.22), we obtain the following equation for the radial component of the functions A and B

$$\frac{C}{v^3} \frac{\partial f}{\partial v} = \left(-\boldsymbol{A} f + \frac{1}{2} \nabla \cdot \boldsymbol{B} f \right)_v. \tag{3.23}$$

From now on, we require $A_\theta = A_\phi = 0$. In the following steps, a general spherical form of B $= b(v)b_{ij}$ will be used to determine $b(v)$ and $A_v(v)$. Then we transform A_i and B_{ij} into cartesian coordinates for use in the Langevin equation. The goal is to find a choice that results in simple forms in cartesian coordinates. The singularity at $v = 0$ is inherent in the model heating equation due to the choice $g = 1$ and cannot be avoided by special choices of b_{ij}. In the implementation, special care has to be taken to avoid numerical instability due to this.

3.5 Ansatz and Langevin Equation

The goal is to make a particular choice for B that results in vanishing angular components after taking the divergence. This will lead to a form of A that depends only on the total velocity. The Ansatz is

$$B_{ij}(v) = B(v) \begin{pmatrix} 1 & 0 & 0 \\ 0 & 1 & 0 \\ 0 & 0 & 1 \end{pmatrix}. \tag{3.24}$$

Then, Equation (3.23) becomes

$$\frac{C}{v^3}\frac{\partial f}{\partial v} = -Af + \frac{1}{2v^2}\frac{\partial}{\partial v}\left(v^2 B f\right) - \frac{1}{v}Bf, \tag{3.25}$$

for the v-component. It turns out that the θ and ϕ components of the divergence of B_{ij} are zero. We find:

$$\frac{C}{v^3}\frac{\partial f}{\partial v} = f\left(-A + \frac{1}{2}\frac{\partial B}{\partial v}\right) + \frac{1}{2}B\frac{\partial f}{\partial v}. \tag{3.26}$$

Comparing coefficients for f and $\partial f/\partial v$, we find

$$B = \frac{2C}{v^3}, \tag{3.27}$$

and

$$A = -\frac{3C}{v^4}. \tag{3.28}$$

Converting from spherical to cartesian coordinates leads to:

$$\boldsymbol{A_{sp}} = -\frac{3C}{v^4}\begin{pmatrix} 1 \\ 0 \\ 0 \end{pmatrix} \Longleftrightarrow \boldsymbol{A_{ca}} = -\frac{3C}{v^5}\begin{pmatrix} v_x \\ v_y \\ v_z \end{pmatrix}, \tag{3.29}$$

and

$$\boldsymbol{B_{sp}} = \frac{2C}{v^3}\begin{pmatrix} 1 & 0 & 0 \\ 0 & 1 & 0 \\ 0 & 0 & 1 \end{pmatrix} \Longleftrightarrow \boldsymbol{B_{ca}} = \frac{2C}{v^3}\begin{pmatrix} 1 & 0 & 0 \\ 0 & 1 & 0 \\ 0 & 0 & 1 \end{pmatrix}. \tag{3.30}$$

The diffusion matrix is decomposed into

$$\widetilde{\boldsymbol{B_{ca}}} = \sqrt{\frac{2C}{v^3}}\begin{pmatrix} 1 & 0 & 0 \\ 0 & 1 & 0 \\ 0 & 0 & 1 \end{pmatrix}, \tag{3.31}$$

so that the Langevin equation reads

$$dv_i = -\frac{3C}{v^5}v_i dt + \sqrt{\frac{2C dt}{v^3}}\xi_i. \tag{3.32}$$

where ξ_i are Gaussian random variables. This is a desirable choice, since the random term only depends on the total velocity. For practical purposes, we have to modify Equation(3.32) slightly to avoid numerical problems at $v = 0$. In the simulation we use

$$dv_i = -\frac{3C}{(v+\epsilon)^4}\frac{v_i}{v}dt + \sqrt{\frac{2Cdt}{(v+\epsilon)^3}}\xi_i, \tag{3.33}$$

effectively introducing a cutoff at small velocities. This is still consistent with a similarly modified FP equation. For small but finite ϵ, it can be shown that the stochastic differential equation for v fulfills a Lipschitz condition and a growth criterion and has a unique solution [37].

3.6 Description of the Algorithm

Before implementing the algorithm, we have to address the singularity at $v = 0$. Integrating the IB heating Equation (3.7), we see that with $g = 1$, particle number conservation is not guaranteed for an arbitrary initial velocity distribution, but only for the self-similar solution. It turns out that after splitting the operator into drift and diffusion terms, the drift part alone does not even conserve particles in its self-similar solution. We demonstrate this property in the following section. In the implementation, the resulting numerical instability is suppressed by introducing a cutoff at slow velocities and resulting large velocity changes. This is done in two steps. First, we add a small constant ϵ to the velocity in the denominator to avoid the singularity when the velocity is close to zero. Second, we disallow large velocity changes, i.e. larger than the current velocity. This

reflects the fact that the IB heating equation is similar to $e - e$ collisions and the heating is due to many small velocity changes.

3.6.1 Algorithm

The following steps are necessary for each particle each time step the particles are heated:

Step 1 Set $\Delta v_{Drift} = -\frac{3C}{(v+\epsilon)^4}\frac{1}{v}dt$

Step 2 Set $\Delta v_{Diff} = \sqrt{\frac{2Cdt}{(v+\epsilon)^3}}$

Step 3 If $|\Delta v_{Drift}| > 1$ then set $\Delta v_{Drift} = 0$

Step 4 For all three components:

(a) Generate Gaussian random variable X with width 1.

(b) If $|X\Delta v_{Diff}| > 1$ generate new X.

Step 5 Push particle with $\Delta v_i = \Delta v_{Drift} v_i + X\Delta v_{Diff}$

3.7 Particle Conservation

The plasma automatically conserves particles, unless a mechanism for creation and destruction, such as ionization and recombination, is explicitly taken into account. The same is naturally true for the particle code. The simplified kinetic equation for heating does not guarantee particle conservation by itself, as can be easily seen by integration

$$\frac{\partial f}{\partial t} = \frac{1}{v^2}\frac{\partial}{\partial v}\left(\frac{Cv^2}{v^3}\frac{\partial f}{\partial v}\right), \tag{3.34}$$

which yields the density evolution

$$\frac{\partial n}{\partial t} = \frac{\partial}{\partial t}\int_0^\infty v^2 f dv = C\frac{1}{v}\frac{\partial f}{\partial v}\bigg|_{v\to 0}^{\infty} \stackrel{?}{=} 0. \tag{3.35}$$

The last equality is not true in the general case but for the self-similar solution particle number is conserved and finite. To see in detail how the Langevin approach models the Fokker-Planck equation in this particular problem, we have investigated the drift and diffusion parts separately.

3.7.1 Fokker-Planck with Diffusion Only

With diffusion only, the drag term A is set to be zero. The kinetic equation then reads

$$\frac{\partial f}{\partial t} = \frac{1}{v^2}\frac{\partial}{\partial v}\left(v^2 f\frac{\partial B}{\partial v} + v^2 B\frac{\partial f}{\partial v}\right). \tag{3.36}$$

We search for a self-similar solution of the form $F(v/v_0)$, where v_0 contains the time dependence. This can be found as

$$f(v) = \frac{v^3}{v_0^6}\exp\left(-\frac{k}{5}\frac{v^5}{v_0^5}\right), \tag{3.37}$$

where k is a free parameter determined by the initial conditions and

$$v_0 = \left(v_0^5|_{t=0} - 5kCt\right)^{1/5}. \tag{3.38}$$

As long as v_0 is real, this solution does conserve particles as can be found by integration. Figures (3.1) and (3.2) show the distribution function after

a long time and the temperature evolution of such a system.

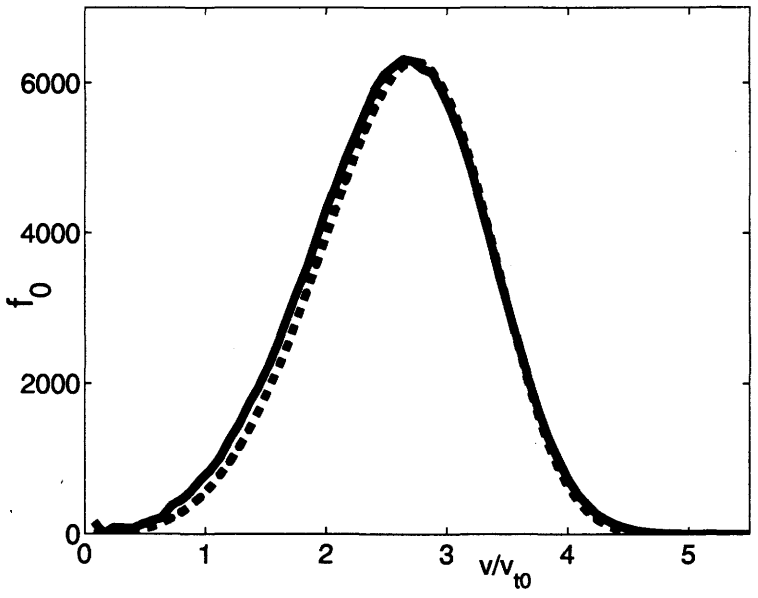

Figure 3.1 Isotropic distribution function at $t = 100\tau_{ei0}$ with diffusion term in heating algorithm only. Dashed line is a fit of the form Equation (3.37). The solid line is the distribution measured in the simulation.

3.7.2 Fokker-Planck with Friction Only

Defining diffusion $B = 0$, the Fokker-Planck equation is

$$\frac{\partial f}{\partial t} = \frac{3C}{v^2}\frac{\partial}{\partial v}\left(\frac{f}{v^2}\right). \tag{3.39}$$

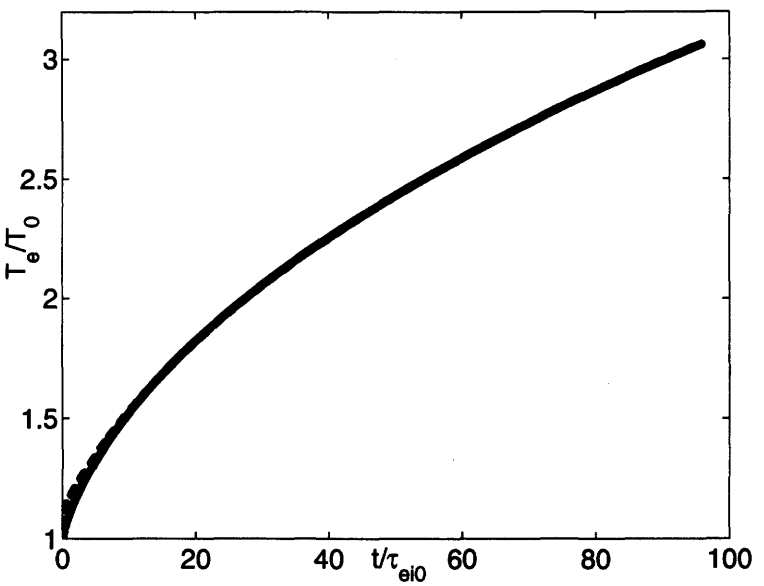

Figure 3.2 Temperature evolution with diffusion term in algorithm only.

Again, defining the variable $x = v/v_0$, where $v_0 = v_0(t)$ contains the time dependence, we find the solution

$$f(v) = \frac{x^2}{v_0^3} \frac{C}{kx^5 + 3}. \tag{3.40}$$

Therefore, particles are not conserved in the friction only case. In the simulation, particle number is forced to be conserved, so we see that this self-similar solution is only approximately achieved, with faster decrease in f at large velocities.

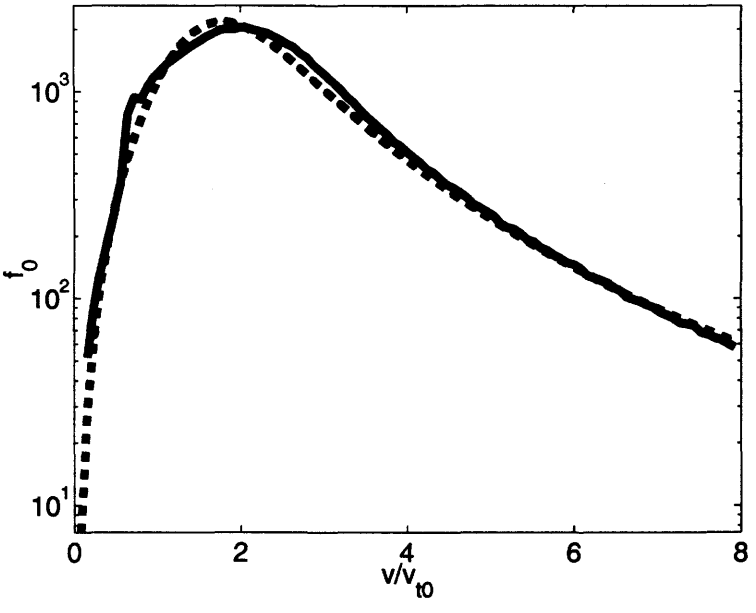

Figure 3.3 Isotropic distribution function at $t = 100\tau_{ei0}$ with friction term in heating algorithm only. Dashed line is fit of the form Equation (3.40). Solid line is distribution measured in simulation.

Figure 3.3 shows simulation results and a best fit in the form of the

self-similar solution to the Fokker-Planck equation. For large velocities, the distribution falls below the fit due to the particle conservation of the code. From these considerations, it is obvious that only the exact balance of friction and diffusion in the Fokker-Planck equation results in the desired solution of the IB heating equation.

3.8 Simulation Results

3.8.1 IB Heating Only

The first test problem we consider is a homogeneous plasma with an initial waterbag velocity distribution. A waterbag distribution is defined as

$$f(v_i) = \begin{cases} \frac{\sqrt{3}}{2} & \text{if } -\sqrt{3} < v_i < \sqrt{3}, \\ 0 & \text{otherwise,} \end{cases} \tag{3.41}$$

such that the mean velocity is zero and the mean square velocity is 1. The time step is $0.2\tau_{ei}$ and heating is included every time step. The simulation is run with 10^6 electrons to enable resolution of the distribution over several orders of magnitude. After a few heating steps, the self-similar state is reached. Figure (3.4) shows the distribution function after 200 e-i collision times. For comparison, a Maxwellian distribution at the same temperature is included in the plot. After such a long time, and higher temperature plasma ($T = 3.2T_0$), even at high velocities of up to 4-5v_{t0}, the simulated distribution follows the analytical prediction. We find slight inaccuracies at small velocities. These are partly due to the small number of particles in each velocity space volume element at small velocities. We recall that

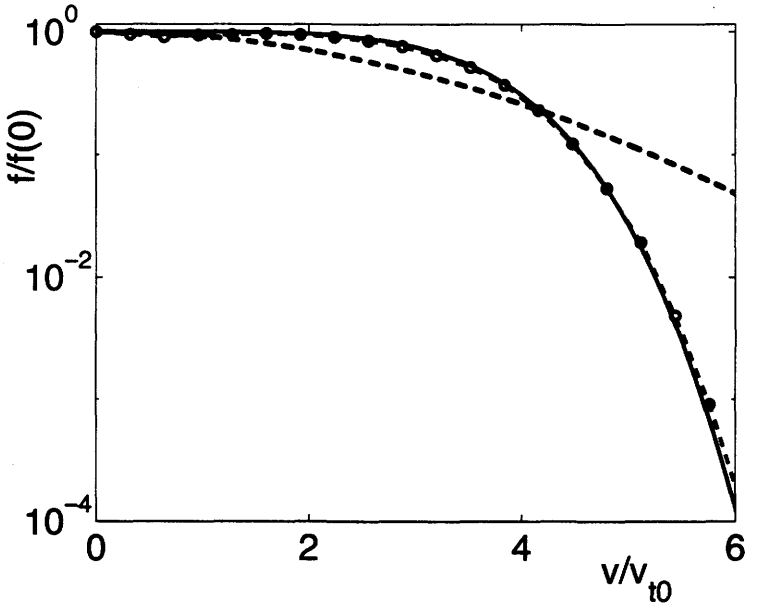

Figure 3.4 Isotropic electron distribution $f/f(0)$ on logarithmic plot for a simulation without e-e collisions and only IB heating. Solid line is the self similar solution from Equation (3.11) and the dashed line with circles are PIC results at $t = 200\tau_{e-i0}$. The dashed line is a Maxwellian distribution at the same temperature for comparison.

the particle code essentially measures $v^2 f(v)$, from which $f(v)$ is extracted. Another reason is the higher sensitivity of the algorithm at small velocities due to the v^{-4} proportionality of the drift and the v^{-3} proportionality of the diffusion term. Inclusion of $e - e$ collisions, as described in the next section, generally works to attenuate these inaccuracies.

Figure (3.5) shows the heating rate, $< v^2 > /f(v = 0, t)$, and the linear dependence as predicted is clearly observed. The slope corresponds to the

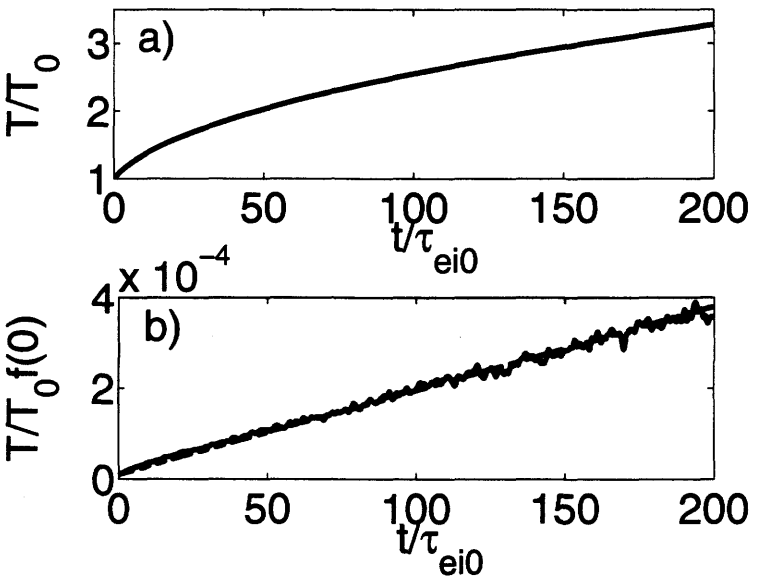

Figure 3.5 Temperature and heating evolution. a) shows the temperature evolution. b) shows evolution of $T/T_0 f(0)$ as solid line. The dashed line is predicted value of $2C/f(v=0,t=0)t$.

right heating rate of $8\pi C$, which also quantitatively verifies the heating procedure. The algorithm is quite robust to changes in the laser intensity (or equivalently to changes in time step). This suggests that it is possible to do the heating operation on a larger time step than the electric field calculation in a complete self-consistent PIC simulation.

3.8.2 $e-e$ Collisions

A further test and proof of the algorithm as an investigative tool for the distribution function is the inclusion of electron-electron collisions in the simulation. These are simulated using a binary pair Monte Carlo type

algorithms as described in [26, 27] and have been used successfully on the problem of nonlocal electron heat transport in a preformed hot spot [17] and electron distribution functions [36]. Matte *et al* [5] suggest that for the combined operator, a distribution function should be of the form described by Equations (3.13) and (3.14).

The simulation parameters are the same as before with ion charge $Z = 10$. We start the simulation with an initial $\alpha = 10$, and since the plasma is heated, a wide range of values from $\alpha = 10$ to $\alpha = 0.8$ is covered in a single simulation. We find that a function of the form of Equation (3.13) fits well

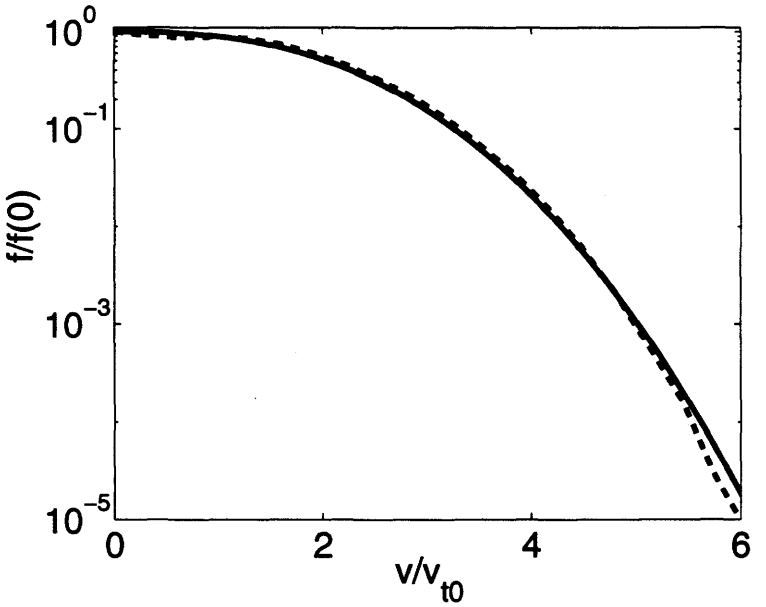

Figure 3.6 Isotropic electron distribution $f/f(0)$ on logarithmic plot for simulation with $e - e$ collisions ($Z = 10$) and IB heating. Solid line is a fit of a supermaxwellian with $f(v) = \exp\left[-(v/v_0)^{2.56}\right]$ and $v_0 = 2.36$. Dashed line is the simulation result.

the distribution function. Figure (3.6) shows the distribution function after 200 e-i collision times. At this time, $m = 2.56$, and m is within 10% of the Matte predictions. In Figure (3.6) the distribution falls only slightly below the fit at small velocities which demonstrates the attenuating effect of $e - e$ collisions on the fluctuations of f at small velocities as compared to the case without collisions.

4. Nonlocal Electron Heat Flux at Arbitrary Temperature Gradients

4.1 Introduction

In the previous chapter, the basic process of heating of the plasma through irradiation with laser light has been discussed. We used and justified the assumption that primarily electrons are heated. The physical process of heat transport in plasma is a rich and complex process in itself, and will be discussed in this chapter. The heat transport by electrons to the colder plasma regions determines the efficiency of the implosion in an ICF target and, in general, determines the plasma conditions in the whole experimental region.

One of the experimental situations, that motivate the study of heat flux from laser heated plasmas is the problem of uniform illumination of the target in ICF [1]. In an ideal situation, a uniform intensity on the spherical target can be achieved with at least six laser beams which have uniform intensity profiles and only negligible small phase distortions. This situation is quite realistic for modern table top lasers. However, the high-power lasers required to achieve the high intensity needed for ICF typically can not provide such high quality beams. The many optical surfaces such as lenses, mirrors and apertures cumulatively introduce distortions that are usually

10 times, or more, larger than diffraction limited distortions. The resulting intensity profile on the target is therefore usually highly nonuniform.

Designs from Kato and Mima[40] and by Lehmberg and Obenschain [41] are based on the observation that the target size (typically $\sim mm$) is much larger than the focus size of the laser (usually $\sim \mu m$). The basic idea is to improve the beam quality at the cost of losing some of the focus of the beam. In both techniques, the beam is divided into a large number of smaller beamlets, where each of the smaller beams has a much smaller distortion than the original beam. The resulting beam has a larger spot size in the far field but, as discussed above, this size can match the diameter of the target. At a given time, the beamlets produce a complicated pattern that changes with the laser coherence time. If this time is small compared to hydrodynamic responses of the target, the plasma will see only the smooth, time-averaged intensity profile. Induced spatial incoherence (ISI) [41] and random phase plates (RPP) [40] are the most common designs to achieve this goal. In the usual embodiment of ISI, a pair of reflecting, echelon-like mirrors is used to divide a broad bandwidth laser beam into many independent beamlets. The echelons introduce time delays between the beamlets which are longer than the laser coherence time. In RPP the beam is propagated through a phase plate that randomly divides the beam into a large number of beamlets, half of which are delayed by a phase separation of π. In ISI and RPP the beamlets are then overlapped onto a target. Both methods usually result in interference pattern of localized hot spots in the laser focus.

Spatial inhomogeneities of laser intensity produce localized plasma heating and modify the electron distribution function (EDF) [42]. Because of small hot spot sizes, which can be comparable to the electron mean free path, hydrodynamic equations are incorrect and kinetic models should be applied in the investigation of energy transport in such a plasma [43, 7, 6]. In order to better understand the physics of thermal conduction and localized inverse Bremsstrahlung (IB) heating, studies of a single hot spot relaxation and energy exchange between neighboring hot spots have been conducted. Steep temperature gradients, due to localized heating by nonuniform laser beams, give rise to nonlocal heat transport [44, 45, 16, 25]. In the hot plasma, the mean free path becomes comparable to the gradient scale length. On average, the electrons travel a scale length or more between collisions, thereby rendering the assumption of a local transport invalid. We have generalized the expression for the nonlocal heat flux derived from small perturbation theory [16] to the case of finite amplitude initial perturbation of electron temperature. An approximate, practical formula has been proposed and tested for the nonlocal heat flux in the nonlinear regime. Different laser-plasma interaction processes can be significantly altered due to non-Maxwellian EDF. Supermaxwellian distributions ($\propto \exp(-v^m)$, with $m > 2$), which result from collisional heating, can cause a reduction in heat flux, due to the less densely populated tails in the distribution functions. In this chapter, we investigate heat transport and EDF in plasmas heated by single and multiple laser hot spots. QNPIC is used for the numerical results. We have compared our results with Fokker-Planck codes from Batyshchev [17] for some of the results on the tails in the EDF. In the case of a hot

spot heated by IB, we find a flattened EDF for the bulk of electrons and well-pronounced high-energy tails due to spatial transport.

The organization of this chapter is as follows. First, we outline the classical electron heat flux calculations, which go back to the classical works by Spitzer and Härm[12] (SH). The heat flux is written in form of Fick's Law, as a function of the local gradient. We note that in a laser-plasma, this classical theory becomes invalid, and often much smaller heat fluxes, than expected from classical theory, are observed because density gradient scale lengths are comparable to the electron mean free path. Next, heat flux limiting schemes employed in magnetohydrodynamic codes to reflect the inhibition are described. A more physical interpretation of the inhibition leads to the concept of nonlocal heat flux. Before performing simulations of hot spot relaxation, different nonlocal heat flux models are described, and the simulation results experiments are used to extend the self-consistent model of Bychenkov [16] to regimes of finite temperature perturbations. Localized IB heating will be investigated. Stationary temperature and heat flux profiles are presented. A reduced heat flux is found that exhibits a similar functional dependance on the temperature profile as that of SH.

4.2 Classical Heat Transport

Before introducing nonlocal models, we will outline the SH [12] calculation of heat transport. In local heat transport theory, the heat flux can be

written in a form analogous to Fick's law for density gradients:

$$q(x) = -\kappa(x)\frac{\partial T}{\partial x}, \tag{4.1}$$

where κ is computed by solving a simplified kinetic equation. The kinetic equation to solve is

$$\frac{\partial f}{\partial t} + \mathbf{v}\cdot\frac{\partial f}{\partial \mathbf{x}} - \frac{e\mathbf{E}}{m}\cdot\frac{\partial f}{\partial \mathbf{v}} = A\frac{\partial}{\partial \mathbf{v}}\cdot\left[\frac{v^2\mathbf{I} - \mathbf{vv}}{v^3}\cdot\frac{\partial f}{\partial \mathbf{v}}\right] + C_{ee}(f). \tag{4.2}$$

C_{ee} denotes the electron electron collision operator and $A = (2\pi Ze^4/m^2)\ln\Lambda$. A two term expansion is used which reflects strong collisions, thereby implying that higher order anisotropies can be neglected.

$$f = f_0(v) + \mu f_1(v), \tag{4.3}$$

where $\mu = v_x/v$. Then a kinetic equation for f_1 can be derived. For simplicity, we neglect $e-e$ collisions assuming a high Z plasma (making $e-i$ collisions dominate the collisional processes). For f_0, we assume a Maxwellian with temperature T and the electric field is determined by a zero current condition (assuming quasineutrality and a vanishing initial current). f_1 is

$$f_1 = f_0\frac{v^4}{4mA}\left[\frac{8}{v_{te}^2(x)} - \frac{v^2}{v_{te}^4(x)}\right]\frac{\partial T_e}{\partial x}. \tag{4.4}$$

The heat flow is determined by calculating the third moment of f_1 giving

$$q_{SH}(x) = -\kappa_0(x)\frac{\partial T_e}{\partial x} \tag{4.5}$$

where

$$\kappa_0 = \frac{128}{3\pi}\gamma_\kappa n_e v_{Te}\lambda_{ei}. \tag{4.6}$$

The effect of $e-e$ collisions is computed numerically by Spitzer and approximated by

$$\gamma_\kappa = 0.24 + Z/4.2 + Z. \tag{4.7}$$

The SH assumption of $f_1 \ll f_0$ (and so on for f_2 etc.) fails for large temperature gradients. Heat fluxes larger than the free streaming limit $nT_e v_{te}$ are predicted for large gradients. Bychenkov and Krasheninnikov [16, 46] have shown that a full kinetic treatment is necessary for regimes of $1/20\sqrt{Z} \leq \lambda_{ei}L$, where λ_{ei} is the mean free path and L is the gradient scale length. Physically, this reflects that the locality assumption implied in $f_0 \gg f_1$ no longer holds, and increasingly more terms in the expansion of f are necessary.

4.3 Flux Limiting in Hydrodynamic Simulations

A heuristic attempt to match the heat flux into the collisionless regime has been to simply limit the heat flux to a maximum value. A typical maximum value would be the free streaming limit when all electrons move with thermal velocity $q_{max} = nT_e v_{te}$. This concept is widely used in hydrodynamic simulations for laser plasma experiments. The heat flux here is

$$q = \min\left[\kappa\frac{\partial T}{\partial x}, fnT_e v_{te}\right], \tag{4.8}$$

where f is the so-called flux limiter. Typically, f is chosen to a value around 0.1. However, this model clearly lacks physical interpretation as it treats the transport locally pointwise and for a better understanding analytic and numerical calculations of the full kinetic equation are necessary. Early numerical works (e.g. [44]) show that a limiter as small as 0.1 is necessary but also indicate that a single flux limit is in general not sufficient. Clearly, a more sophisticated model is needed to improve transport routines, that are still sufficiently economical for use in hydrodynamic codes.

4.4 Nonlocal Transport

Since the early 80s several efforts to develop a theory for nonlocal transport regimes have been made [15, 14, 47, 45, 46]. Albritton et al [14] used a reduced Fokker-Planck equation and divided the distribution into a Maxwell-Boltzmann part plus a perturbation δf which contains the information about the heat flux, i.e. of the fast electrons. The reduced Fokker-Planck equation is solved for δf in the limit of fast velocities. Such a closing scheme, the velocity distribution can be expressed as a convolution of the Maxwellian with a Gaussian in space with an additional velocity dependence. For the heat flux, it results in a kernel with complicated integral propagators. Luciani, Mora and Pellat [15] suggest a simpler kernel, that is based on numerical solution of the Fokker-Planck equation and simple physical arguments.

These kernels contain parameters or numeric factors which are not self-consistently defined and require comparison with simulations. Some expres-

sions may lead to nonphysical results as was demonstrated in Ref. [48, 49]. The expression for the nonlocal electron heat flux found in Ref. [16] is self-consistent. However, it was derived in a small perturbation approximation and the question naturally arises if it is valid beyond this formal restriction. We have compared our PIC simulations with this nonlocal theory [16], extending its results to the large perturbation case. Such a comparison shows, that the expression for the nonlocal heat conductivity works well for $n_e = const$, even for the time dependent problem, if the temperature inhomogeneity is modest, i.e. $\lambda_{ei}/L < 1$. This correlates well with the findings of Ref. [25] from δf-model for small perturbation case. All schemes have in common that the heat flux is expressed as a convolution integral of the temperature (gradient) rather than just the local gradient. The electron heat flux can be presented in the form

$$q(x) = \int_{-\infty}^{\infty} q_{SH}(x')G(x,x')dx' , \tag{4.9}$$

where q_{SH} is given by Equation (4.5) and $G(x,x')$ is a nonlocal kernel. For instance, the Refs. [15] (LMV) and [45] (E) provide, correspondingly, with the following kernels

$$G_{LMV}(x,x') = \frac{1}{2a\lambda_e(x')} e^{-\eta} , \tag{4.10}$$

$$G_E(x,x') = \frac{1}{\pi a\lambda_e(x')} \left[\frac{\pi}{2} \sin\eta - \mathrm{Si}(\eta)\sin\eta - \mathrm{Ci}(\eta)\cos\eta \right] , \tag{4.11}$$

where $\lambda_e = Z\lambda_{ei}^{FP}/\sqrt{Z+1}$, $\eta = \mid x - x' \mid /a\lambda_e(x')$, $Si(\eta)$ and $Ci(\eta)$ are the sine and cosine integrals, and a is the parameter to be adjusted through the

comparison with numeric simulation ($a = 32$ [15] and $a = 50$ [45]).

Here, we suggest a new kernel as generalization of the analytical result for nonlocal heat conductivity, κ, which was derived for small perturbations [16]. The transport theory is self-consistent in the limit of linear perturbations. In the following, we outline the main aspects of the theory. A perturbation δf of the equilibrium Maxwellian distribution function is given in terms of hydrodynamical forces n_e and T_e (and E and u_i if necessary). In the kinetic equation $e - i$ collisions are included by a pitch-angle scattering operator with a velocity dependent collision frequency $\nu_{ei}(v)$.

Electron-electron collisions are linearized

$$C_{ee}[f_e, f_e] \approx C_{ee}[\delta f, F_0] + C_{ee}[F_0, \delta f]. \tag{4.12}$$

δf is expanded in Legendre polynomials

$$f = \sum_l f_l(v) P_l(\mu), \tag{4.13}$$

and a hierarchy of coupled kinetic equations of the angular harmonics f_l is obtained. Restricting the analysis to slow (quasistationary) processes in the plasma, the time derivatives are dropped. Each angular harmonic f_l is then expanded in basis functions ϕ as

$$f_l = \frac{e\Phi}{T_e} F_0 \delta_{l,0} + \frac{\delta n_0}{n_e} F_0 \phi_l^N + \frac{3}{2} \frac{\delta T_0}{T_e} F_0 \phi_l^T - iku_i F_0 \phi_l^R. \tag{4.14}$$

The result is an infinite system of linear equations which the authors trun-

cate and solve with the software package Mathematica. Taking the heat flux moment of f_1, the heat flow in terms of the hydrodynamic forces is obtained and numerical results are tabulated [16]. We find an approximate fit in a simple analytic form:

$$\kappa(k) = \frac{\kappa_0}{1 + (ak\lambda_e)^{0.9}}, \quad \lambda_e = \sqrt{Z}\lambda_{ei}, \; k\lambda_{ei} < 1, \tag{4.15}$$

where a is the function of Z, which fits the results [16] with the accuracy at least 15% and reads

$$a = 10\frac{Z+5}{Z+12}. \tag{4.16}$$

In the linear model it is implied that the mean free path λ_e, and κ_0 are constant in Equation (4.15). This however restricts the model to very small temperature perturbations, as $\lambda_e \propto T_e^2$ changes rapidly with temperature. Similarly $\kappa_0 \propto T_e^{5/2}$ the classical heat flux is a function of T_e. For an application of the model to realistic, nonlinear temperature perturbations, we suggest to treat λ_e and κ_0 locally within the kernel. Equation (4.15) leads to the kernel

$$G(x,x') = \frac{\xi(\eta(x'))}{\pi a \lambda_e(x')}, \quad \xi(\eta) = \int_0^\infty \frac{dp\, \cos \eta p}{1 + p^{0.9}}. \tag{4.17}$$

The function $\xi(\eta)$ is shown in Figure 4.1. In the limit $\eta \to 0$ it grows as $\xi(\eta) \approx \Gamma(0.1)\cos(\pi/20)\eta^{-0.1} \approx 9.4/\eta^{0.1}$ and for $\eta \to \infty$ it vanishes as $\xi(\eta) \approx 0.9\Gamma(0.9)\cos(\pi/20)\eta^{-1.9} \approx 0.95/\eta^{1.9}$, where Γ is the usual Γ-function. Equation (4.17) is the newly suggested kernel which takes into account nonlocality in the heat flux as well as nonlinearity in the classical

heat conductivity and the mean free path.

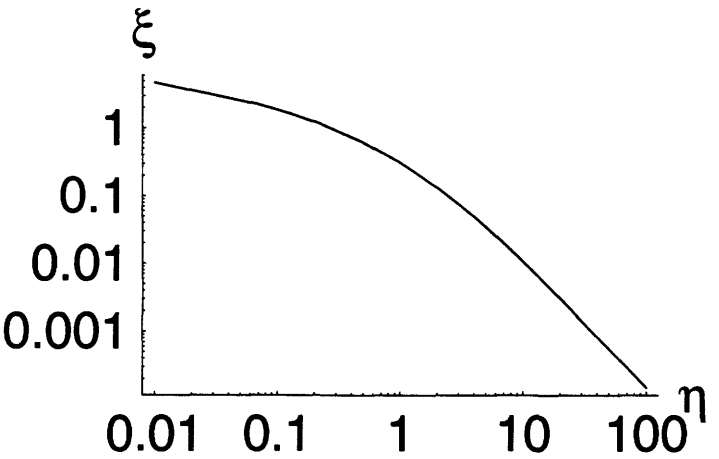

Figure 4.1 The nonlocal kernel $\xi(\eta)$ (4.17) for the electron heat flux in nonlinear transport model.

In Section 4.5 we simulate a single hot spot relaxation as an initial value problem using QNPIC. Based on these simulation results, we have proposed the aforementioned practical formula for nonlocal heat flux. Section 4.6 describes FP and collisional PIC simulations of localized plasma heating in a single hot spot.

4.5 Hot Spot Relaxation

In order to verify the nonlocal transport theory [16], and extend the thermal conduction model to nonlinear regime of perturbations, we consider relaxation of the initial localized temperature perturbation. The simulations are carried out in a 1D planar geometry hot spot that corresponds to the instantaneous release of laser energy at the time $t = 0$ in the given

x-plane. The performance of QNPIC is further verified by comparison with results from the FP code FPFIAN [23].

The 1D PIC simulations were performed for a plasma with ion charge, Z, varying from $Z = 1$ to $Z = 8$. We used periodic boundary conditions that allow to model a single hot spot relaxation until hot electrons reach the boundary. Initially, electrons had a Maxwellian distribution with a Gaussian temperature profile

$$T_e(x, t = 0) = T_0 + T_1 \exp\left(-\frac{x^2}{L^2}\right). \tag{4.18}$$

The spatial scale length, L was varied over a range from $L = 300\lambda_{ei}^{FP}(T_0)$ down to $L = 11\lambda_{ei}^{FP}(T_0)$, where λ_{ei}^{FP} is $\sqrt{9\pi/2}$ times smaller than the usual electron ion mean free path $\lambda_{ei}(T_e) = 3T_e^2/4\sqrt{2\pi}Ze^4 \ln\Lambda$. For $L = 300\lambda_{ei}^{FP}$ and $T_1 < T_0$ the relaxation of the temperature was close to the classical behavior with Spitzer-Härm (SH) heat conductivity.

Figures 4.2 and 4.3 show the temperature and heat flux spatial distributions computed at the time $t = 4\tau_{ei}^{FP}(T_0)$. The noise level for this simulation with only a small temperature perturbation is quite large with about 10%. This is for rather small and wide initial temperature perturbation, $T_1 = 0.4T_0$, and $L = 18\lambda_{ei}^{FP}$, where $\tau_{ei,ee}^{FP}$ is $e - i$ $(e - e)$ collision time $\tau_{ei}^{FP} = \sqrt{m_e}T_e^{3/2}/4\pi Ze^4 n_e\Lambda = \tau_{ee}^{FP}/Z$. The classical result from the solution to the diffusion equation for the electron temperature, with SH heat conductivity, is presented for comparison (dashed curve in Figure 4.2). Due to the nonlocal nature of energy transport, the relaxation occurs more slowly than with the classical conductivity. Heat flow, q, shown in Figure

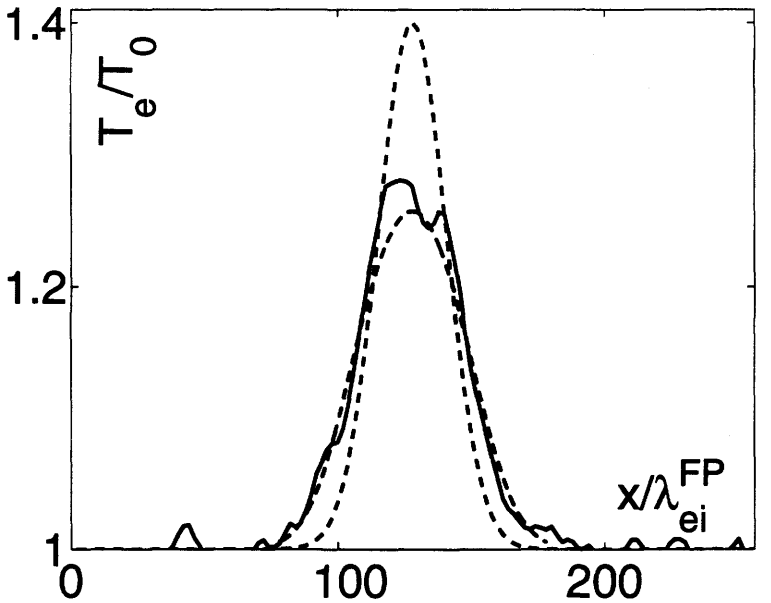

Figure 4.2 Temperature profiles of the hot spot relaxation. Solid line is $T_e(x)$ at time $t = 4\tau_{ei}^{FP}(T_0)$. The two dashed lines are the initial temperature profile and the solution to the classical diffusion equation for the relaxation after $4\tau_{ei}^{FP}(T_0)$.

4.3 is also inhibited compared to SH heat flux ($v_{Te} = \sqrt{T_e/m_e}$) calculated from the temperature profile of Figure 4.2. Clearly, the deviation from SH case increases with the initial spatial temperature gradient. We have compared the results of PIC simulations with those from the FP code FPFIAN. A comparison of the temperature and heat flux profiles is given in Figure 4.4. Good agreement between the PIC and the FP results demonstrates that our PIC model is an effective tool to study transport problems at the large spatial scales, significantly longer than the Debye length. Moreover, even the kinetic features of particle transport can be reproduced well us-

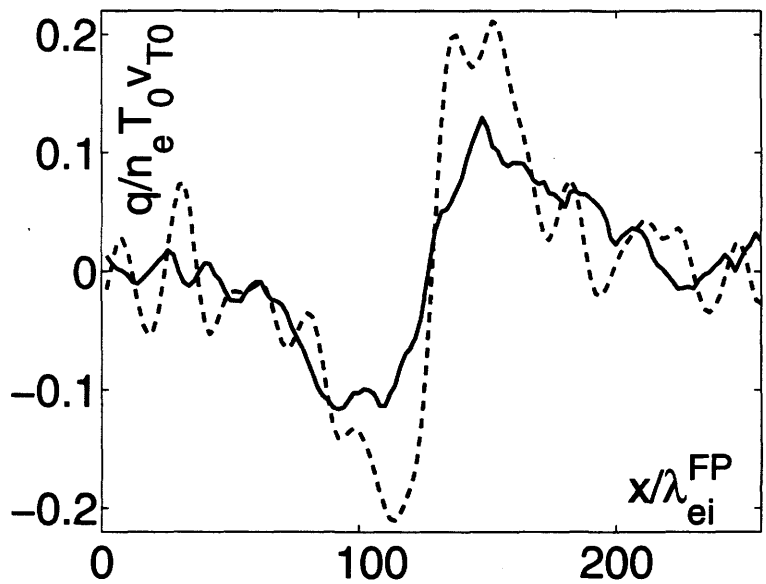

Figure 4.3 Heat flux $q(x)$ after $4\tau_{ei}^{FP}(T_0)$. Solid line flux measure in PIC simulation. Dashed line classical heat flux as calculated from $T_e(x)$ in Figure 4.2.

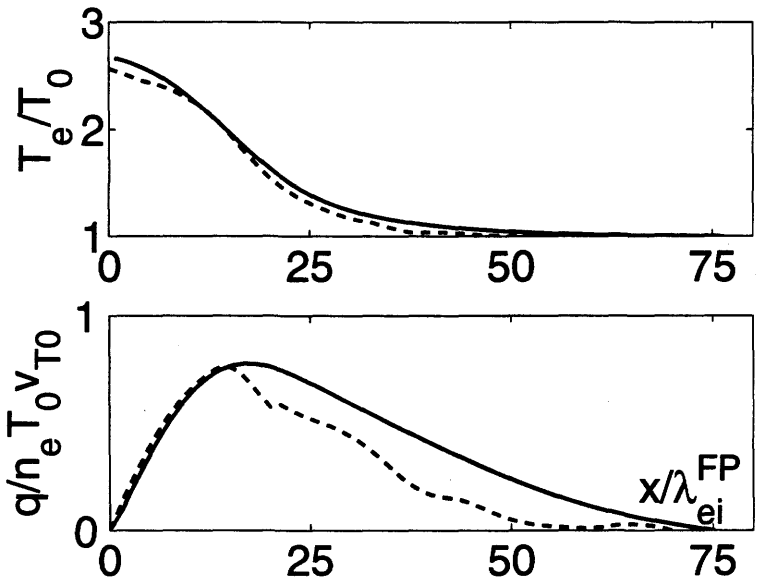

Figure 4.4 Comparison of the temperature and heat flux profiles from QNPIC (dashed) and Fokker-Planck code FPFIAN (solid).

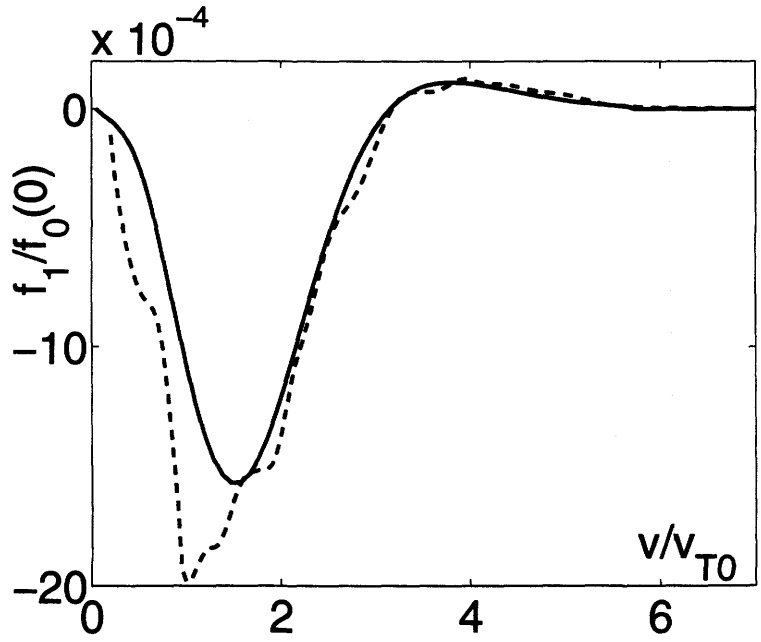

Figure 4.5 Comparison of anisotropic part of distribution function f_1 from QNPIC (dashed) and FPFIAN (solid).

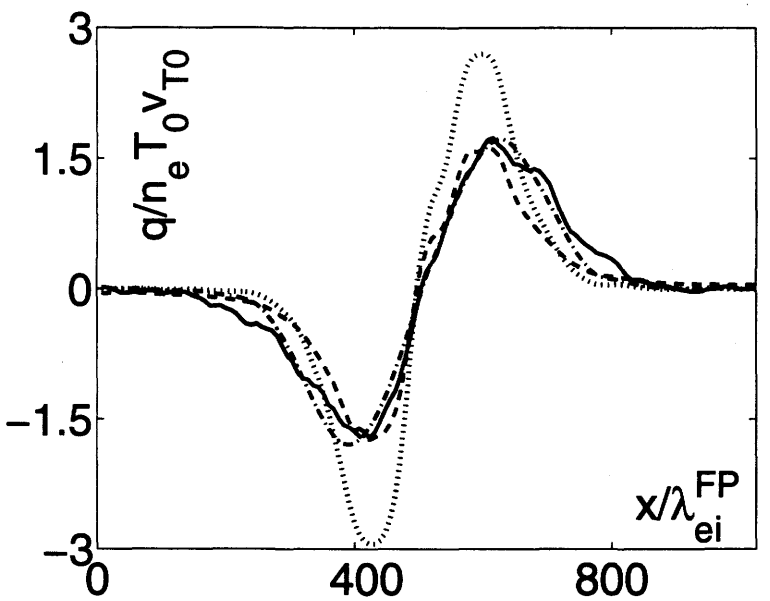

Figure 4.6 Heat flux profiles $q(x)$. The solid line is the heat flux measured in QNPIC. The dotted line shows the SH heat flux. The dashed line shows the LMV nonlocal heatflux and the dash-dotted line shows the nonlinear, nonlocal heatflux using the kernel from Equation (4.17).

ing the PIC model. This is demonstrated in Figure 4.5, where we plot the first anisotropic component, f_1 of EDF versus v/v_{T0}. Here, μ is again the cosine of the angle between electron velocity and temperature inhomogeneity direction, P_n are the Legendre polynomials and $v_{T0} \equiv v_{Te}(T_0)$. In Figure 4.6 the spatial distribution of the heat flux is shown in comparison with the expression [16] (BRTB) followed from Equations (4.9) and (4.17). Accordingly to Figure 4.6, this expression is valid for the nonlinear case. Compared with previous approaches, our method has the advantage that no parameter a needs to be adjusted to give the best fit for different Z. Our kernel, being exact in the linear case, is self-consistent in the sense that it does not contain adjustable parameters.

4.6 IB Heating of a Single Hot Spot

We now consider the stationary heat spot, that is due to the localized IB heating, so that the balance between heating and electron energy transport away from the hot spot will provide the quasistationary state of a plasma. This modeling has been done by using QNPIC and also the FP code ALLA [17], both with the IB heating term as given in [4]. We do not use a more complicated expression for the IB heating term as for example in [36]. The presentation given in [36] would account for the anisotropic part of EDF due to the $e-e$ collisions. The latter is important for the correct description of the EDF at super thermal velocities in a weakly homogeneous plasma. For the inhomogeneously heated plasma considered here, high heat fluxes from the hot spots are dominating the EDF tail formation.

We performed PIC simulations of the dynamics of a single hot spot in a plasma with $Z = 1$ and $Z = 8$. The l aser intensity distribution was chosen of a square form with an intensity I_0 corresponding to $v_E^2/v_{T0}^2 = 0.25$ and a width of $d = 5\lambda_{ei}^{FP}(T_0)$. The position of the laser is indicated in Figure 4.7. The FP equation is solved with free boundary conditions, which allow fast electrons to leave the simulation box and cold Maxwellian electrons to enter with with $T_e = T_0$ to preserve quasineutrality. In the PIC simulations, constant temperature boundary conditions are used. Particles reaching the boundary are re-initialized with the initial temperature $T_e = T_0$. In Figure 4.7 the temperature profile is shown for the quasistationary

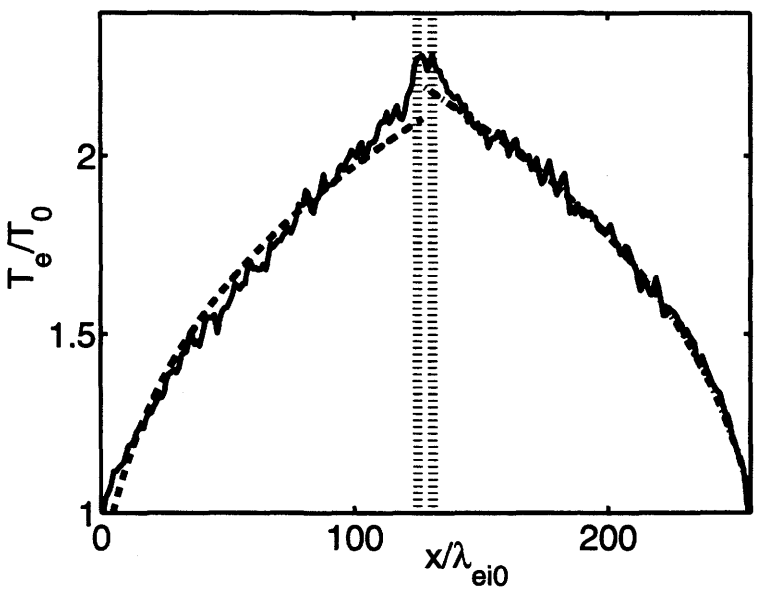

Figure 4.7 Quasistationary temperature profile (solid line) of IB heated hot spot. The heated region is marked by vertical dotted lines. Dashed lines are $\propto x^{2/7}$ fits the profile.

state. The vertical dotted lines show the region of IB heating. The classical

temperature profile from the SH theory can be determined from solving the temperature balance equation with the IB heating term

$$\frac{\partial T_e}{\partial t} - \frac{2}{3n_e}\frac{\partial}{\partial x}\kappa_{SH}\frac{\partial T_e}{\partial x} = \frac{m_e v_E^2}{3}. \tag{4.19}$$

As the profile approaches the quasistationary state the temperature gradient drops and the shape of the temperature profile outside the hot spot becomes similar to that prescribed by the SH theory, following the dependence $x^{2/7}$, as shown by the two dashed lines in Figure (4.7). This is not the case within the hot spot and near it, where the temperature is higher than that calculated from Equation (4.19), because of heat flux inhibition. Figure 4.8

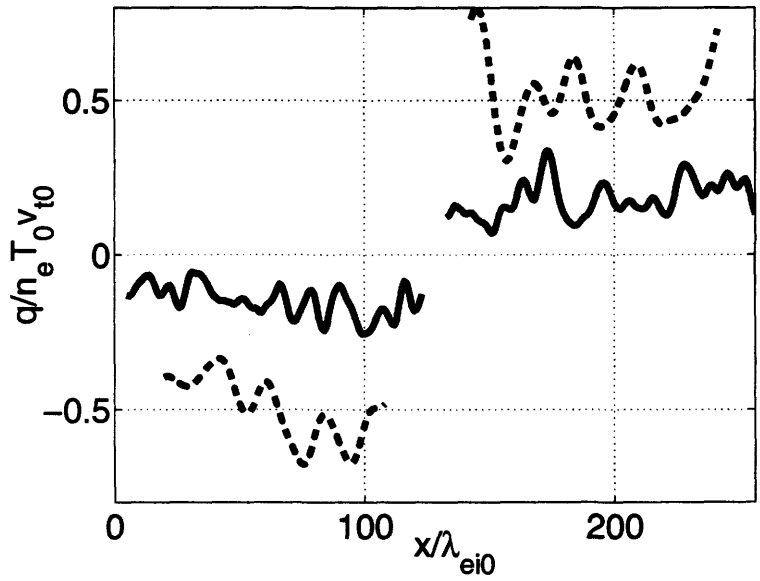

Figure 4.8 Quasistationary heat flux profile (solid line). One can see an approximately constant heat flux outside the hot spot in the centre. The dashed line shows the SH heat flux calculated from $T_e(x)$.

shows the quasistationary heat flux profile. It is very interesting to note that outside the hot spot, both q and q_{SH} are approximately constant, which demonstrates the same functional dependence of the heat flux as in the SH case. The magnitude of the heat flux, however, is significantly (approx. a factor of three) less than q_{SH}, i.e. the effect of heat flux inhibition is displayed primarily as a reduction of the heat conductivity coefficient. To qualitatively discuss the electron distribution function, it is easier to refer to the results from the FP results which are better suited for EDF studies. The FP simulation [22] was performed in a plasma with $Z = 5$. The laser intensity distribution was chosen to be Gaussian

$$I(x) = I_0 \exp\left(-\frac{x^2}{d^2}\right), \tag{4.20}$$

with I_0 corresponding to $v_E^2/v_{T0}^2 = 0.5$ and $d = 5\lambda_{ei}^{FP}(T_0)$. In Figure 4.9a the temperature is shown for transient (curves 1 and 2) and quasistationary regimes (curve 3) in comparison with SH transport model where the temperature profile is found as a solution to the diffusion equation with IB heating. We look at the EDF, both the symmetric part $f_0(v)$, and the anisotropic part $f_a(v,\mu) = f_e - f_0$. These distributions are shown in Figure 4.10 for two spatial locations, within and outside the hot spot, correspondingly. The symmetric part of the EDF out of hot spot has significant superthermal tail which we attribute to the spatial transport effect. In contrast, it has flat-top shape with inhibited tail within hot spot in accordance with particle redistribution caused by IB heating [4]. At the same time, this superthermal domain of the EDF in heating region should be a subject of more detail consideration in the future because of the simplified model of IB heating implemented in the codes. The effect of heat flux inhibition is

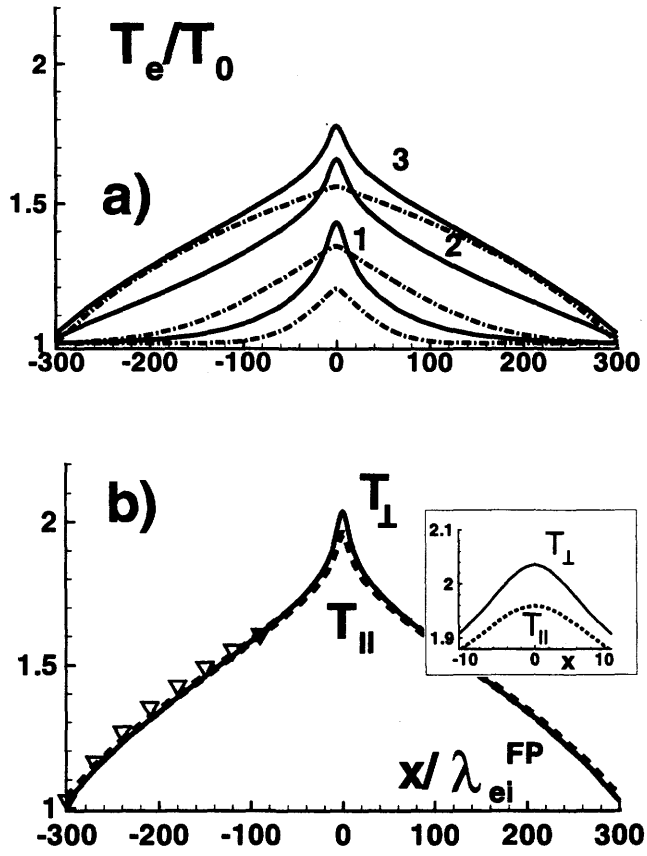

Figure 4.9 Temperature profiles of the IB heated hot spot calculated with the Fokker-Planck code ALLA. For $Z = 5$ at $t = 50\tau_{ei}^{FP}(1)$, $t = 250\tau_{ei}^{FP}(2)$ and $t = 2500\tau_{ei}^{FP}(3)$. (a) Dot-dashed profiles demonstrate the SH temperature obtained from the solution to the diffusion equation for T_e. Panel (b) corresponds to the quasistationary profile. The triangles show a $x^{2/7}$ fit to T near the left boundary.

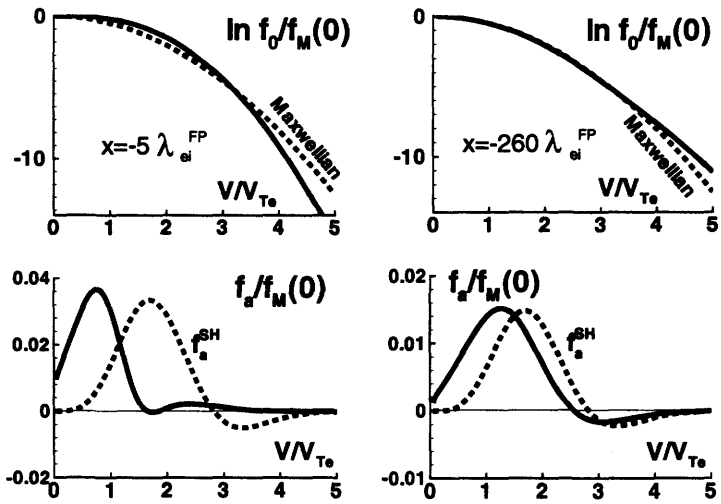

Figure 4.10 Symmetric (upper panels) and anisotropic (bottom panels) parts of EDF from Fokker-Planck simulations in the quasistationary state with $Z = 5$ at $x = -5\lambda_{ei}^{FP}$ (left) and $x = -260\lambda_{ei}^{FP}$ (right) from the centre of the hot spot. The dashed curves show the Maxwellian distribution and anisotropic part for the SH model, respectively.

displayed also through the anisotropic part of the EDF, presented in Figure 4.10 for $\mu = -1$ that corresponds to the electron velocity in the direction of temperature gradient. The anisotropic part of the EDF is more enriched by low velocity electrons, which inhibits heat flux and return current. Out of hot spot, the shape of f_a is similar to SH case, however, within hot spot it is quite different because of IB heating.

4.7 Conclusions

We have proposed a new nonlocal kernel that describes heat conduction in large temperature gradients with constant density and initial EDF near Maxwellian. Numerical simulations performed are in good agreement with the kernel which is a generalization of the linear theory results [16] that does not depend on any fitting parameter.

IB heating of a single hot spot which leads to a stationary profile has been performed in QNPIC and we found that the heat flux outside the heated region displays temperature dependence similar to the SH theory. However, the magnitude of the flux is strongly inhibited as expected from the earlier relaxation results. The EDF is observed and we found enhanced tails of heat carrying electrons away from the hot spot and the typical super Gaussian form in the heated region.

5. Ion Dynamics in Laser Plasmas

5.1 Introduction

Until now, ions have been assumed infinitely heavy. However, the existence of various ion fluctuations can significantly change the electron transport. The electron heat flux, described in the previous chapter, can be modified by ion turbulence in the plasma. The possible mechanism believed to produce the turbulence is the ion-acoustic drift instability, which is driven by the heat flux.

Ion instabilities lead to a turbulent ion spectrum, that may provide a means of energy dissipation in ion motion. The electrons, besides scattering on the ions, now also scatter on electrostatic ion waves. This mechanism increases the effective collision frequency and consequently decreases the electric conductivity and heat conductivity. The modified "anomalous" transport theory has been developed since the 80's[50, 51]. Applications to magnetically confined plasmas and a survey of experimental and numerical studies can be found in the report by Kluiver, Perepelkin and Hirose [9] and references therein. The interplay of both, kinetic effects (nonlocality) and turbulence, and its influence on transport is an intriguing problem to study numerically. Typically, FP codes treat kinetic effects most properly, but until now, neglect the effects of ion dynamics completely. On the other

hand, hydrodynamic codes can only handle kinetic effects phenomenologically, by artificially introducing heat flux limiters for example, as discussed in the previous chapter.

Large scale ion motion is important for modeling long pulse interaction, which lead not only to hot spots in the electron temperature profile, but also to inhomogeneities in the ion densities due to the pressure forces present in the hot spot. Knowledge of the stationary ion density and electron temperature profiles is necessary to properly study ion instabilities in these plasmas. In itself, a kinetic simulation code, that includes ion motion and density gradients and electron temperature gradients, opens the field for further studies of nonlocal transport in plasmas with ∇n and ∇T_e that are commonly encountered in laser plasma experiments. With a weak temperature gradient the electron distribution function can be approximated by an expansion in Legendre polynomials to first order $f = f_0(v) + \mu f_1(v)$. The vector moments current and heat flux are determined by f_1. Simulations show that the heat flux $\int dv v^5 f_1(v)$ is carried mostly by electrons with velocities of $v \approx 3 - 5v_{te}$, as seen in Figure 5.2. A larger number of slower electrons with $v \leq 2v_{te}$, carrying the so called "return current", cause a zero net electric current. This return current is produced by the self-consistent electric field to compensate for the flow of the hot electrons which carry the heat flow. Analog to the two stream instability, the return current causes a drift instability, if the mean drift of the return current exceeds a threshold.

We start the discussion of ion dynamics by deriving the dispersion relation of ion sound within the model of the quasistatic electric field cal-

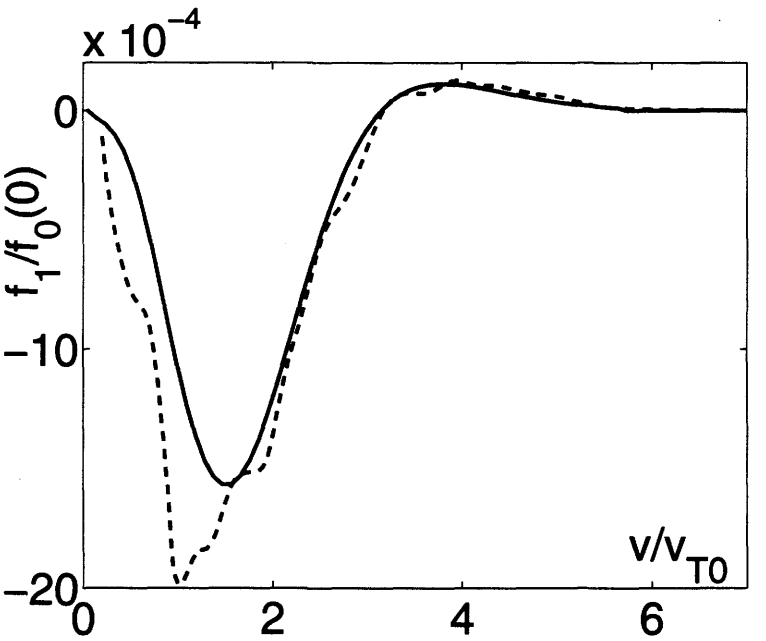

Figure 5.1 Anisotropic part of the distribution function f_1 as found in Chapter 4

culation used in QNPIC, following the derivation of Joyce [30]. We find that ion sound waves are correctly reproduced, with the exception of effects of the order $k^2\lambda_{De}^2$, which are neglected because essentially $\lambda_{De} = 0$ in the quasineutral field calculation. Ion Landau damping is correctly represented. Simulation results from QNPIC are presented that validate the ion dynamics of the simulations.

As a simple test of the interplay between collisions and electric field calculation, we then consider the damping of ion sound waves due to $e - i$ collisions. These cause the electron energies to be not quite Boltzmann distributed, which causes a damping of the order of the $e - i$ collision frequency ν_{ei}. In realistic experiments this effect is not necessarily dominant

since $i - i$ collisions are expected to play a more important role but in this thesis we restrict ourselves to collisionless ions. Before examining the return current instability, we take a closer look at the simpler two stream instability, which is excited by a mechanism similar to the return current instability. The procedure to calculate the growth rate from the numerical results is introduced and used to calculate growth rates from simulations of different streaming velocities. Our results confirm that QNPIC correctly reproduces theoretical results for the regime of the Buneman instability, which is hydrodynamic when the flow is much larger than the electron thermal velocity. For slower velocities, just above the threshold of the ion sound velocity, a different scaling corresponding to the kinetic ion-acoustic instability is verified.

The heating of the streaming electrons, induced by the $e - i$ collisions in the stable regime, and enhanced by turbulent heating in the unstable regime, is calculated and found to confirm analytic results from the theory of anomalous transport and heating [50, 51]. Following the streaming instabilities, we derive a simple dispersion relation for inhomogeneous electron temperature profiles, where the EDF is composed of an isotropic and an anisotropic part. It is shown that it is the slow electrons carrying the return current, that will lead to an instability analogous to the two stream instability. Before showing simulations of ion dynamics in laser heated plasmas, we determine the stationary density and temperature profiles for different inhomogeneous situations. By artificially introducing a large ion temperature, all ion modes are strongly Landau damped and all instabilities are suppressed. These profiles will then be compared to cold ion simulations,

which demonstrate the onset and saturation of the instability.

5.2 Ion Sound Dispersion Relation

The derivation of the 1-dimensional dispersion relation follows standard procedure by linearizing Vlasov equation (neglecting collisions for simplicity)

$$-i\omega f_{\alpha k}(v) + ikvf_{\alpha k}(v) + \frac{neZE}{m_\alpha}F'_{0\alpha}(v) = 0, \tag{5.1}$$

around the Maxwellian $F_{0\alpha}(v)$. This gives for the perturbed part of the distribution function

$$f_{\alpha k}(v) = -\frac{in_0eE}{m_\alpha}F'_{0\alpha}(v)\frac{1}{\omega - kv}, \tag{5.2}$$

for species α.

In the quasineutral procedure, developed by Joyce [30], the electric field is not determined from Poisson equation but from

$$-eE = \frac{1}{n_i}\frac{\partial}{\partial z}(n_iT_e) = \frac{1}{n_i}\frac{\partial}{\partial z}\left(\frac{n_iP_e}{n_e}\right), \tag{5.3}$$

where

$$P_e = \int dv f_e m_e v^2. \tag{5.4}$$

We linearize around the background temperature and density to get

$$-eE_k = \frac{1}{n_0^2}ikn_{ik}P_{0e} + \frac{1}{n_0}ikP_{ek} - \frac{1}{n_0^2}ikP_{0e}n_{ek} = \frac{ik}{n_0}P_{ek} + ik\frac{T_{0e}}{4\pi en_0}\rho_k, \tag{5.5}$$

where we use the definition

$$P_{0e} = T_{0e} n_0. \tag{5.6}$$

Substituting the appropriate moments of $f_{\alpha k}$ for n_{ik} and T_{ek} into Equation (5.5), we arrive at the dispersion relation of the quasineutral simulation model

$$0 = -\frac{\omega_{pe}^2}{k^2} \int \frac{dw F'_{0e}}{w} - \frac{\omega_{pi}^2}{\omega^2} + \frac{k^2 \omega_{pi}^2}{\omega^2} \int dw w^3 F'_{0i} - \frac{i\pi}{k^2} \left[\omega_{pe}^2 F'_{0e} \left(\frac{\omega}{k} \right) + \omega_{pi}^2 F'_{0i} \left(\frac{\omega}{k} \right) \right]. \tag{5.7}$$

To derive the simplified dispersion relation given in Equation (5.18), an expansion is done, with the assumptions $v_{te} \gg c_s \gg v_{ti}$ and $T_e \gg T_i$. The resulting expression is similar to the standard expression, derived from Poisson's equation. The only difference is the assumption of $k\lambda_{De} = 0$, due to the way of calculating the electric field from Equation (5.3).

The basic dispersion relation is verified by carrying out simulations in homogeneous (in temperature) plasmas. The results allow us to examine within which range of wavelengths ion sound waves are properly described. Waves of all wavelength are excited by initially rectangular shaped density perturbations, similar to the ones used in Chapter 2 to verify conservation of quasineutrality. This configuration is used to confirm the dispersion in lowest order, when there is no driving term (flow) and we neglect all damping. Figure (5.2) shows the dispersion relation obtained from a simulation with $M_i/m_e = 200$ and $Z = 1$. In this case, to lowest order the dispersion follows $\omega = kc_s$, where $c_s = 1/\sqrt{200}$ in this configuration. The dashed line

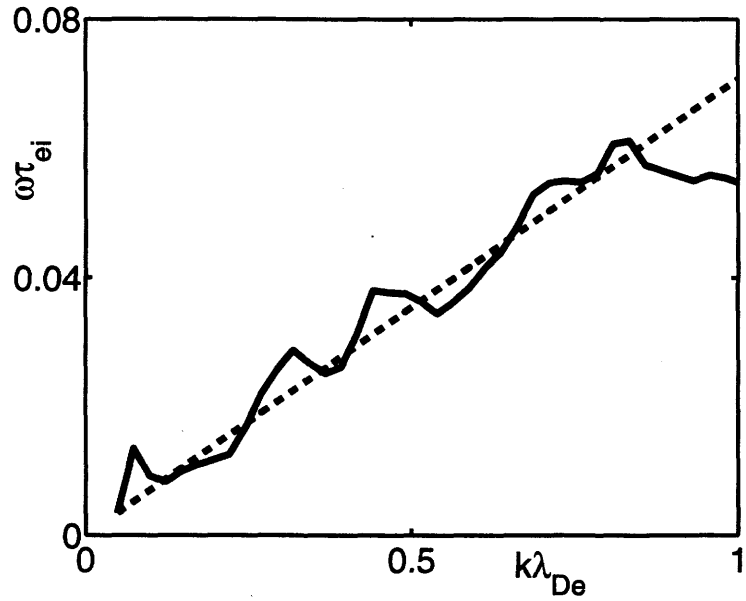

Figure 5.2 Dispersion of initial density perturbation. $\omega(k)$ (solid) as determined from the simulation. Dashed line $\omega = kc_s$ theoretical, linear dispersion in lowest order.

shows the linear dispersion for comparison. The dispersion is well represented up to $k \approx 0.8$, which corresponds to a wavelength of approximately $\lambda \approx 8\lambda_{De}$, where λ_{De} is also the grid spacing in this simulation. At this wavelength, the smoothing due to the employed weighting scheme (3rd order) is becoming effective, which suppresses wavelengths below this regime. As noted in the derivation above, the assumption of quasineutrality breaks down, as $k\lambda_{De}$ effects become important at these wavelength in real plasmas. The procedure of the calculation of the dispersion relation from the simulation is sketched below.

5.2.1 Calculation of Dispersion

The core program used for the wave analysis (Fourier transform, autocorrelation) of the data produced by the simulation is provided by R. Sydora [52]. All analysis is performed on the electric field data on the grid. First, the electric field data is fourier transformed in space

$$E(x,t) \rightarrow E_k(t), \tag{5.8}$$

into the different k-modes. This form is useful for measuring growth rates of instabilities in dependence of k. For each k-mode the autocorrelation is calculated

$$c(\tau) =< E_k(t)E_k(t-\tau) >\equiv \int_0^T dt E_k(t)E_k^*(t-\tau). \tag{5.9}$$

From this form it is usually more convenient to measure damping rates and frequencies of the waves as functions of k-mode. Finally, by fourier transforming the autocorrelation function, we obtain the powerspectrum for each k-mode. For the calculation of the linear dispersion relation above with a large number of k-modes, the maxima of these power spectra are automatically determined and tabulated to give $\omega(k)$ directly.

5.3 Collisional Damping of Ion Sound Waves

Joyce [30] has demonstrated that ion Landau damping is correctly represented within the same simulation model as in QNPIC. However, collisional damping has not been considered so far. To demonstrate and validate the

correct interplay of ion sound waves and collisions, we consider the damping of ion sound waves due to $e-i$ collisions. The standard derivation from ion fluid equations and Poisson's equation, where electrons are assumed to be Boltzmann distributed, is no longer valid in this case, since the $e-i$ collisions appear as friction in the electron momentum equation and cause a delay in the electron response.

To emphasize the effect of damping due to $e-i$ collisions, we derive a simple dispersion from linearized cold ion fluid equations:

$$\omega\tilde{n}_i = n_0 k\tilde{u}_i, \tag{5.10}$$

and

$$\omega M_i n_0 \tilde{u}_i = eZn_0 k\phi, \tag{5.11}$$

where n_0 is the background density. For the electrons we use warm fluid equations with friction due to $e-i$ collisions,

$$\omega\tilde{n}_e = n_0 k\tilde{u}_e, \tag{5.12}$$

and

$$-\omega m_e n_0 \tilde{u}_e = en_0 k\phi - T_e k\tilde{n}_e - i\nu_{ei} n_0 m_e \tilde{u}_e. \tag{5.13}$$

The system is closed by quasineutrality,

$$Z\tilde{n}_i- = \tilde{n}_e \tag{5.14}$$

Terms of the order $k^2\lambda_{De}^2$ are neglected in this approach and we can solve the

system to lowest order in k. The real part is the usual $\omega = kc_s$ (with $c_s = \sqrt{ZT_e/M_i}$) and the imaginary damping part is $\gamma \approx \nu_{ei} Z^2 m_e/2M_i$. Since $i-i$ collisions are absent within QNPIC, and for cold ions Landau damping is absent, this is the only damping term and can be clearly observed as demonstrated in Figure (5.3).

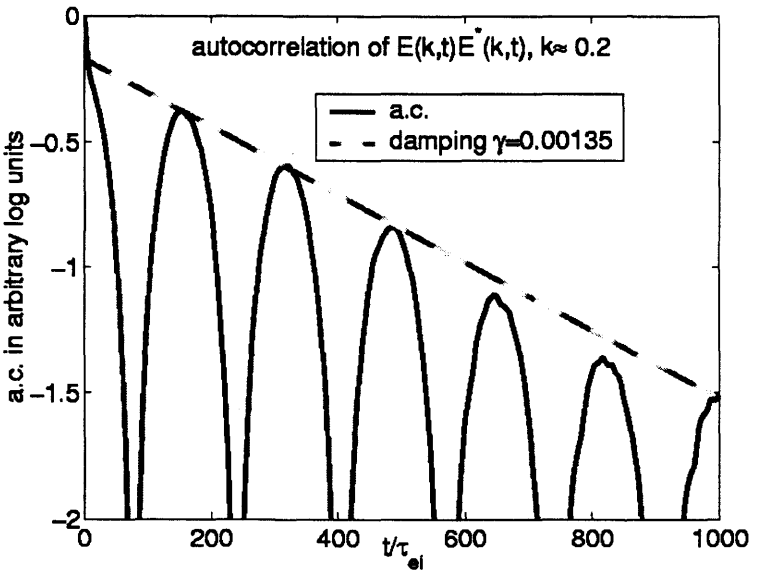

Figure 5.3 Autocorrelation of $k = 0.2 k_\lambda De$ mode (solid line). The damping rate agrees well with predicted value (dashed line).

5.4 Two Stream Instabilities

Before introducing the return current instability, we study the closely related phenomenon of a streaming instability. The ions are Maxwellian with zero flow and the electrons are described by a shifted Maxwellian

distribution (in the x-direction)

$$f_e(v_x) = n\sqrt{\frac{m}{2\pi T}} \exp\left(-\frac{m(v_x - u)^2}{2T}\right). \tag{5.15}$$

If u is larger then the ion sound velocity $c_s = (ZT_e/M)^{1/2}$ the plasma becomes unstable if $T_i \approx 0$ and ion Landau damping can be neglected. A detailed analytic analysis of the general two stream instabilities was done e.g. by Ahedo and Lapuerta [53, 54]. A simple derivation can be found for example in chapter 24 in the standard textbook by Goldston and Rutherford [55]. If the difference between electron drift and ion sound velocity is large, one deals with a hydrodynamical instability, which was first described by Buneman [56]. Ahedo [53] points out that the character of the instability goes from reactive to resistive as $(v_d - c_s)/v_{te}$ becomes smaller. In this case, kinetic effects determine the nature of the instability. It is analogous to Landau damping with the difference that the slope of the distribution function is positive in the resonance region as shown schematically in Figure (5.4) . The resonant ions gain energy from the streaming electrons. The transition from hydrodynamic to kinetic instability is marked by a change of the scaling with respect to ion mass (or sound velocity) of the growth rate. In the Buneman case it scales as $(m_e/M_i)^{1/3}$ and in the kinetic regime like $(m_e/M_i)^{1/2}$.

5.4.1 Buneman Instability

The nonlinear evolution and saturation mechanisms of the Buneman instability in collisionless plasmas has been studied extensively by Ishihara,

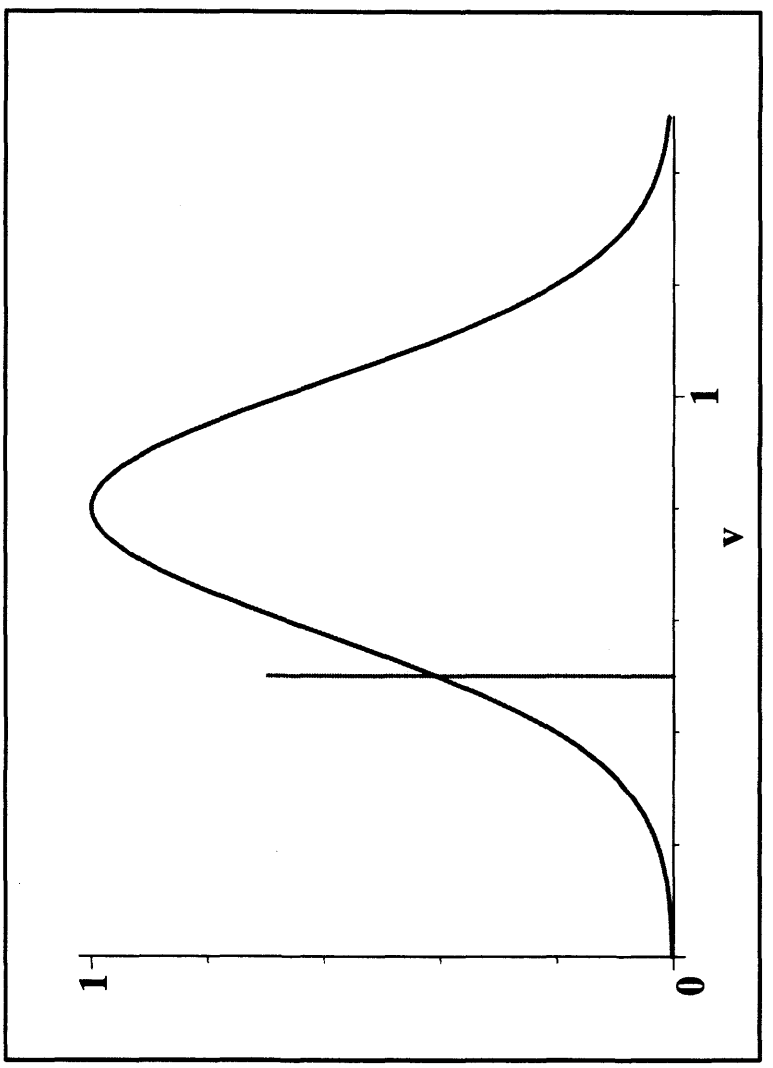

Figure 5.4 Sketch of electron distribution function (solid line). The derivative at $v = c_s$ (dashed vertical line) is positive, thus causing instability.

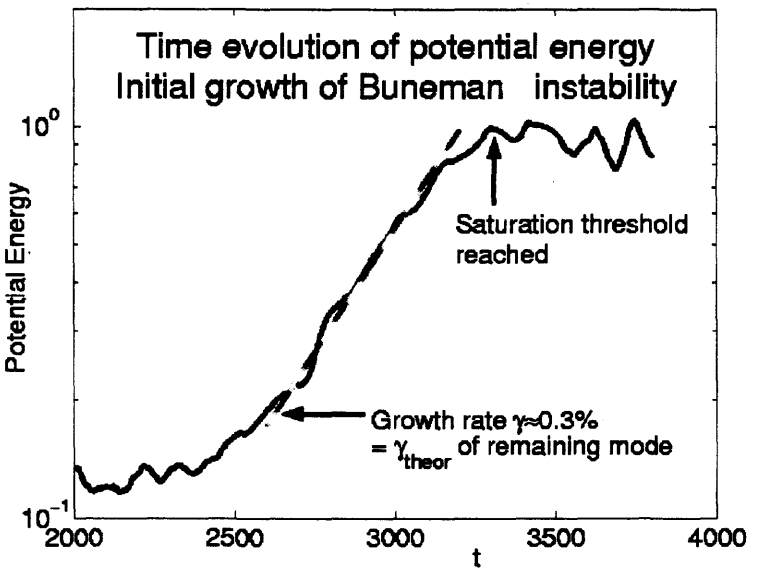

Figure 5.5 Total electric field energy evolution of the Buneman instability normalized to the initial value at $t = 0$ (solid line). The theoretical prediction is shown by the dashed line.

Hirose and Langdon [57, 58, 59]. In the simultion the electron drift velocity is chosen as $v_d = 2v_{te}$. Figure (5.5) shows the time evolution of the electrostatic energy during the instability. The growth is soon saturated due to the slowing down of the beam and electron heating. The drift velocity falls below the threshold for the instability. The growth rate of the instability in the initial growth phase is given by [60]

$$\gamma = \omega_{pe} \frac{\sqrt{3}}{2^{4/3}} \left(\frac{m_e}{m_i} \right)^{1/3} \tag{5.16}$$

5.4.2 Kinetic Ion Acoustic Beam Instability

The solution for the growth rate of the dispersion relation (5.7) for long wavelength is

$$\begin{aligned} \gamma &= \sqrt{\frac{\pi}{8}} \left[\frac{\omega(ku - \omega)}{kv_{te}} - \frac{T_e}{T_i} \frac{\omega^2}{kv_{ti}} \exp\left[-\frac{\omega^2}{2k^2 v_{ti}^2} \right] \right] \\ &= \sqrt{\frac{\pi}{8}} kc_s \left[\sqrt{\frac{m}{M}} \left(\frac{u}{c_s} - 1 \right) - \left(\frac{T_e}{T_i} \right)^{3/2} \exp\left(-\frac{T_e}{2T_i} \right) \right]. \end{aligned} \tag{5.17}$$

The first term leads to destabilization if $u > c_s$. It depends on the ratio of the unstable electron term to the stabilizing ion term if the wave becomes unstable. The ion term reflects ion Landau damping and is negligible if $T_i \ll T_e$.

In Figure (5.6) the onset of the instability after about $1200\tau_{ei}$ is shown in a plot of the total electrostatic energy. The initial drift velocity of the electrons of $0.2v_{te} \approx 2.8c_s$ had reduced by about 5% at this time. The fastest growing mode in this simulation was for $\omega \approx 0.15$. The expected growth

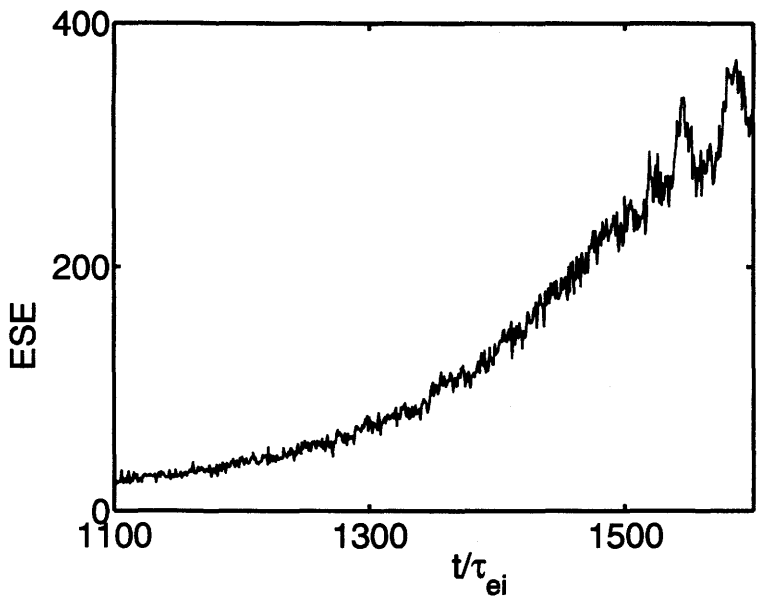

Figure 5.6 Total electric field energy normalized to initial value at $t = 0$.

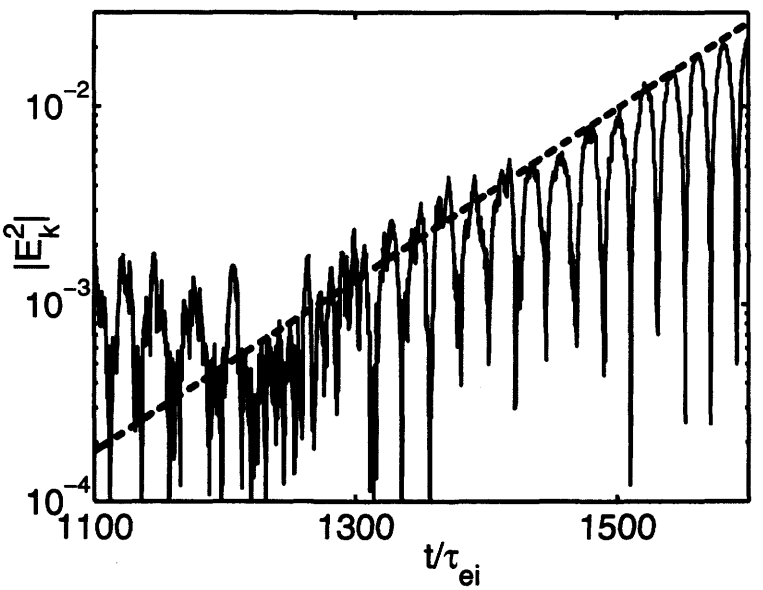

Figure 5.7 Electrostatic energy of the k-mode corresponding to $\omega = 0.15$ (solid line). The dashed line corresponds to an exponential fit $\exp(\gamma t)$ with $\gamma = 0.01$.

rate is then $\gamma \approx 0.011$, if Landau damping is neglected. Figure (5.7) shows the time evolution of the electrostatic energy of this mode on a log scale and an exponential fit for a growth rate of $\gamma = 0.01$. Clearly, a reasonably good agreement between theory and experiment is visible. The slightly lower growth rate is probably due to ion Landau damping effects, since at $1100\tau_{ei}$ the initially cold ion distribution has heated. Energy reduction in the electron beam prohibits further growth.

To demonstrate the reliability of the quantitative growth, results for a slower electron drift ($0.1v_{te} \approx 1.4c_s$) are presented as well. Figure (5.8) shows the time evolution of the total electrostatic energy. The instability begins at roughly $1800\tau_{ei}$. The growth of a specific mode (as before $\omega \approx 0.15$ is shown in Figure (5.9) together with the theoretical growth rate of $\gamma \approx 0.0028$ as dashed line. Good agreement with the theoretical prediction is found even at the low growth rate found in this example.

5.4.3 Anomalous Heating and Resistivity

In the drifting electrons, $e - i$ collisions will cause slowing down of the beam due to resistivity and randomization of electron velocities, causing the electrons to heat up while slowing down. In the presence of density fluctuations, electrons will not only undergo $e - i$ collisions, but also scatter on ion sound waves. This causes the effective resistivity and heating rates to increase in the so called anomalous regime.

In a nonturbulent plasma, which we can enforce by using hot ions, such that all instabilities are Landau damped, the electron heating is classical

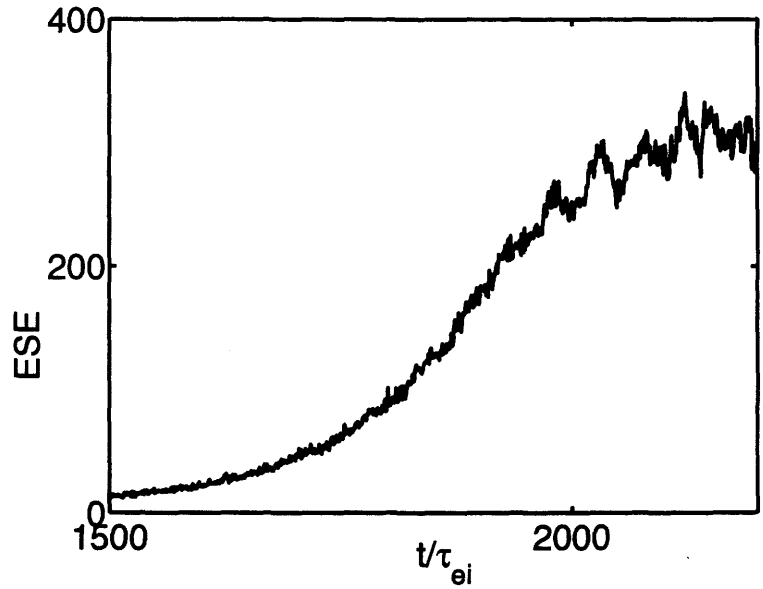

Figure 5.8 Total electric field energy normalized to initial value at $t = 0$.

and described by

$$\frac{dT}{dt} = \frac{0.34}{\tau_{ei}} u^2, \tag{5.18}$$

where u is the drift velocity and τ_{ei} is the $e - i$ collision time [13].

Figure 5.10 demonstrates that the classical heating rate is very well reproduced. If ions are initially cold, the streaming instability can develop fully until it saturates due to trapping and electrons slowing down below the threshold. In Figure (5.11) enhanced heating compared is clearly observed once the instability develops. In the turbulent regime, we have compared with the approximate turbulent heating prediction by Galeev [51]

$$\frac{dT}{dt} = \nu_{eff} m_e u^2, \tag{5.19}$$

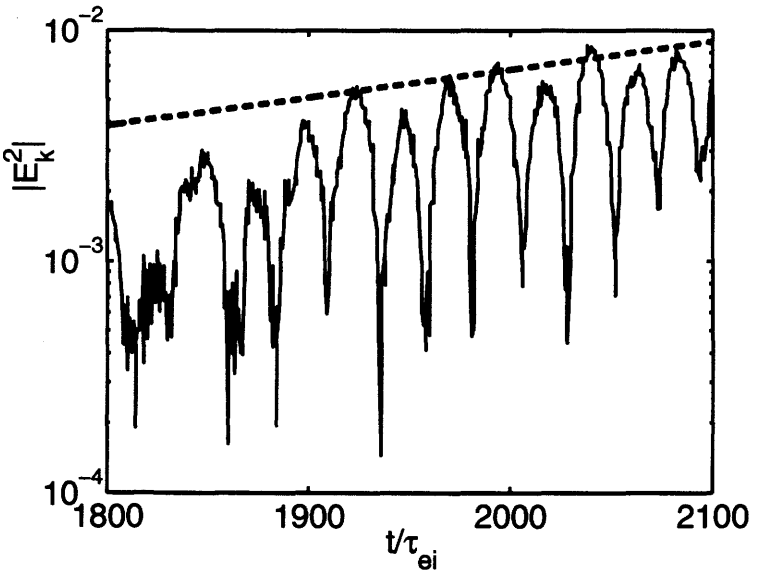

Figure 5.9 Electrostatic energy of the k-mode corresponding to $\omega = 0.15$ (solid line). The dashed line corresponds to an exponential fit $\exp(\gamma t)$ with $\gamma = 0.0028$.

with the approximate effective collision frequency given by

$$\nu_{eff} \approx 10^{-2}\omega_{pi}\frac{u}{c_s}\frac{T_e}{T_i}. \tag{5.20}$$

5.5 Return Current Instability

The return current instability, which occurs in plasmas with temperature gradients and strong heat fluxes, is closely related to the formerly described two stream instabilities. In this case there is no net current of electrons, but an electron heat flux created by an electron temperature

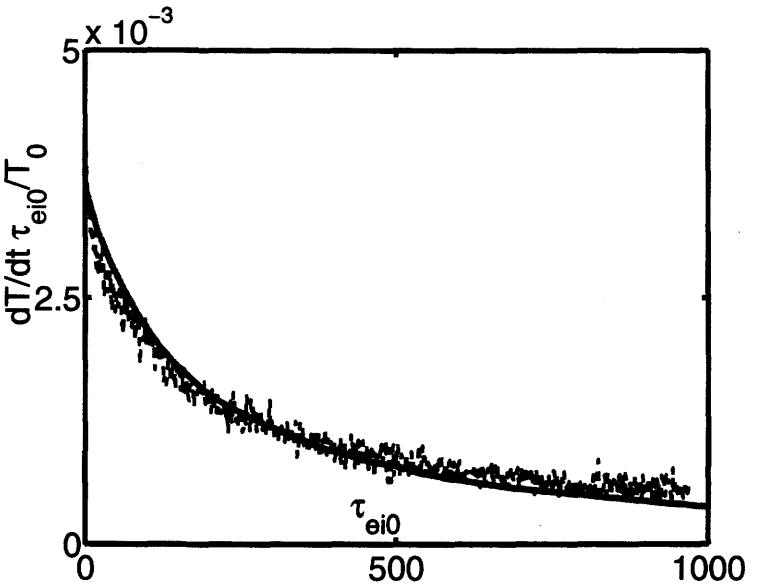

Figure 5.10 Dashed ragged line shows heating rate, solid line heating rate calculated from r.h.s. of Braginskii heating rate. Ions are warm to suppress instabilities.

gradient. Hot electrons with velocities above approximately $3v_{te}$ carry the energy down the temperature gradient. A larger number of slower electrons flows in the opposite direction such that overall the electric current is zero. If the mean velocity of the slower "return current" electrons is greater than the ion sound velocity approximately, they drive ion sound waves unstable (analogous to the two stream case). The derivation of the return current instability starts with the standard plasma dispersion relation derived from the dielectric tensor. For simplicity, we assume adiabatic ions and $T_e \gg T_i$, so that ion Landau damping is completely neglected. Then, the dispersion relation is

$$1 - \frac{\omega_{pe}^2}{k^2} \int d^3v \frac{1}{\xi - v_{||}} \frac{\partial f_e}{\partial v_{||}} - \frac{\omega_{pi}^2}{k^2} = 0, \tag{5.21}$$

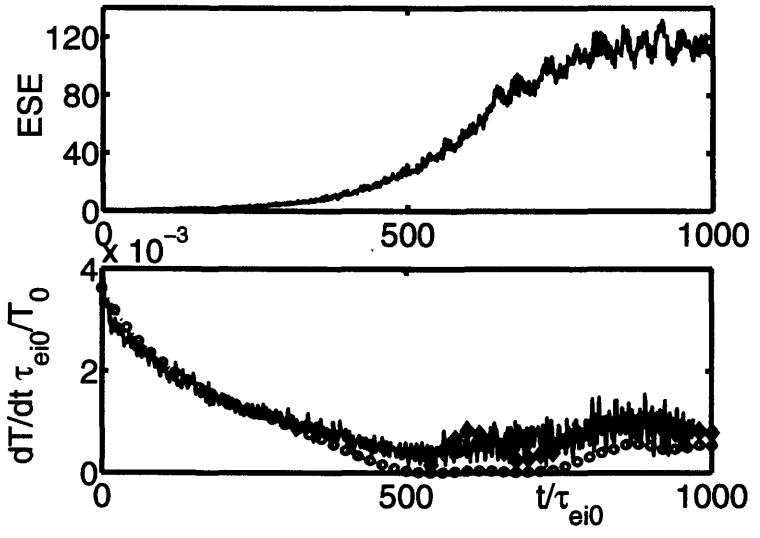

Figure 5.11 The upper figure shows the total electrostatic energy evolution and onset of the instability at $t \approx 400/\omega_{pe}$. Below the corresponding electron heating rate (solid) and the Braginskii prediction (circles) and turbulent heating prediction (diamonds) are shown.

where $\xi = \omega/k$ for shorter notation. We allow for an anisotropy of the unperturbed electron distribution function and expand it in Legendre polynomials

$$f_e = F_0 + \frac{v_{||}}{v} F_1. \tag{5.22}$$

Then, the gradient in parallel direction is

$$\frac{\partial f_e}{\partial v_{||}} = \frac{v_{||}}{v} F_0' + \frac{F_1}{v} - \frac{v_{||}^2}{v^3} F_1 + \frac{v_{||}^2}{v^2} F_1'. \tag{5.23}$$

The integration over the singularity is expanded for $\xi \ll v_{||}$, which is true for ion acoustic waves

$$\frac{1}{\xi - v_{||}} \approx -\frac{1}{v_{||}}\left(1 + \frac{\xi}{v_{||}}\right) - i\pi\delta\left(\xi - v_{||}\right). \tag{5.24}$$

The second term in the real part is of higher order and will be neglected. The velocity integrals can be done by partial integration and variable substitution as outlined for the first term leads to

$$\begin{aligned}
\int d^3v \frac{1}{\xi - v_{||}} \frac{v_{||}}{v} &= -\int d^3v \frac{F_0'}{v} - i\pi \int d^3v F_0' \frac{v_{||}}{v} \delta\xi - v_{||} \\
&\quad -4\pi \int_0^\infty dv v F_0' - i\pi 2\pi\xi \int_0^\infty dv_\perp v_\perp \frac{F_0'\left(\sqrt{\xi^2 + v_\perp^2}\right)}{\sqrt{\xi^2 + v_\perp^2}} \\
&\quad 4\pi \int_0^\infty F_0(v) dv - i2\pi^2\xi \int_\xi^\infty dx F_0'(x) \\
&\approx 4\pi \int_0^\infty F_0(v) dv - i2\pi^2 \xi F_0(0).
\end{aligned}$$

It is assumed that $\xi \approx 0$ in the integration boundary, which is a good approximation for near Maxwellian distributions. For the F_1 integrations the real parts vanish in first order and the imaginary parts of the last two terms cancel each other so we are left with

$$\int d^3v \frac{1}{\xi - v_{||}} \frac{F_1}{v} \approx -i2\pi^2 \int_0^\infty F_1(v) dv. \tag{5.25}$$

Collecting all the terms we obtain the final dispersion relation

$$1 - \frac{\omega_{pe}^2}{k^2} 4\pi \int_0^\infty F_0(v)dv + i2\pi^2 \frac{\omega_{pe}^2}{k^2} F_0(0)\frac{\omega}{k} + i2\pi^2 \frac{\omega_{pe}^2}{k^2} \int_0^\infty F_1(v)dv - \frac{\omega_{pi}^2}{\omega^2} = 0. \tag{5.26}$$

Inserting a complex omega, with small damping $\omega = \omega - i\gamma$,the linear damping rate is

$$\frac{\gamma}{\omega} = \frac{\pi}{4\int_0^\infty F_0(v)dv} \left[F_0(0)\frac{\omega}{k} + \int_0^\infty F_1(v)dv \right]. \tag{5.27}$$

The criterion for instability then becomes

$$P = \frac{k}{\omega F_0(0)} \int_0^\infty F_1(v)dv > 1. \tag{5.28}$$

This shows that the return current of "slow" electrons is driving the instability, because P is calculated by the zero moment of f_1. In contrast, the heat flux corresponds to the fifth ($\int v^5 f_1 dv$) moment of f_1, where the relatively small number of fast electrons determine the heat flux.

5.6 Stationary Profiles

To clearly distinguish the return current instability from large scale ion motion due to inhomogeneous heating, and to provide reference profiles, we first find stationary density and temperature profiles without ion turbulence. Ion oscillations are suppressed by initializing the ion temperature to a sufficiently high value. All oscillations are suppressed by ion Landau damping. We study two configurations, that were used previously in the study of electron heat flux, and will operate in the same parameter regimes

as before with the only exception of allowing ion motion in this chapter.

5.6.1 Heated Boundary

The boundaries are kept at different constant electron temperatures $T_1 > T_0$ at the left and right boundary respectively. Electrons reaching a boundary are reinitialized to the boundary temperature. For ions the same holds, but it is noted that differences in ion temperature effects on the pressure and dynamics are negligible and are important only for Landau damping. We find the heat flux reduced compared to Spitzer-Härm (SH), but the functional form in the quasistationary state is similar as in SH, i.e. $q \propto x^{2/7}$. This is remarkable as density gradients are included in this system. The quasistationary state is defined by non-changing temperature and density profiles. Figure 5.12 shows the system after it has reached the quasistationary state which is demonstrated by an almost constant heat flux.

5.6.2 IB Heating of Single Hot Spot

In this configuration the temperature is initially homogeneously T_0 throughout the simulated region. The boundaries are kept at T_0 during the interaction with the laser. The laser causes IB heating of electrons as implemented in Chapter 3 in a region of about λ_{ei} in the centre of the simulation. Ion motion, due to the higher pressure in the interaction region, causes a drop in the density profile in the heated zone. Again, in the stationary state we find a temperature profile following $T \propto x^{2/7}$ as in SH, but measure a reduced heat flux compared to SH.

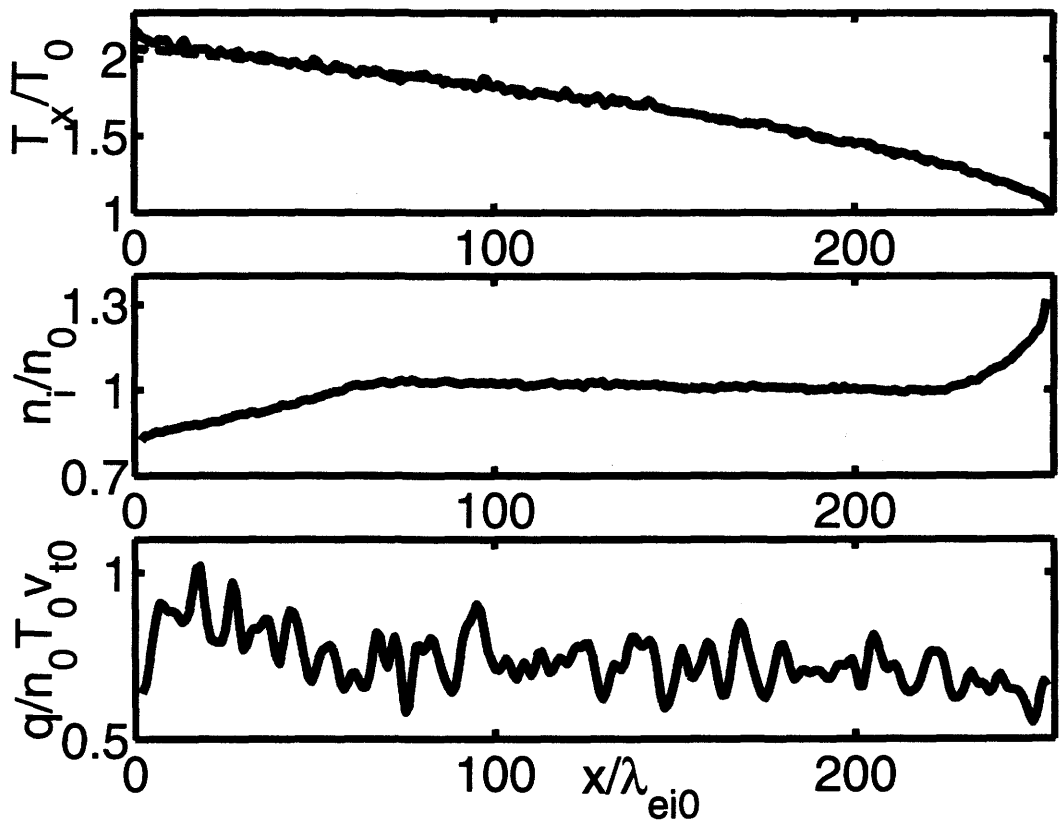

Figure 5.12 Quasistationary (const. heat flux) electron temperature (top) and ion density (centre) profile are shown. T_x is well presented by SH ($T \propto x^{2/7}$ dashed line in top figure) even though heat flux is reduced compared to SH and ion density is not constant. The bottom plot shows the quasistationary electron heat flux.

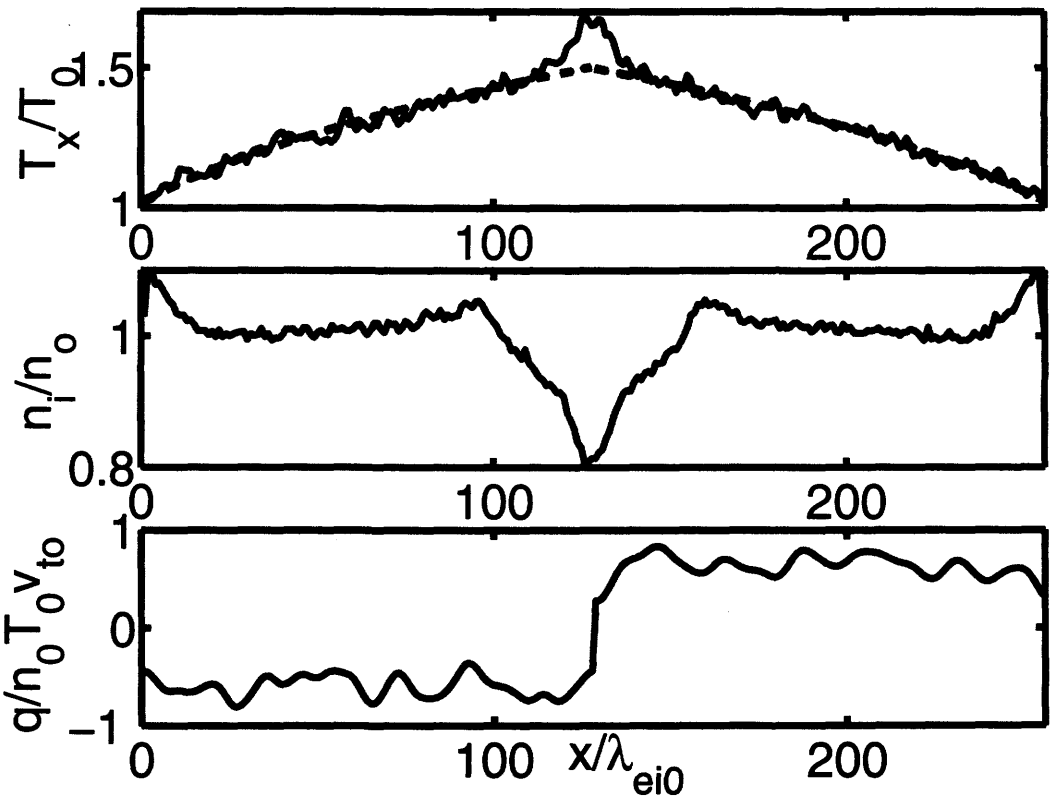

Figure 5.13 Quasistationary (const. heat flux) electron temperature (top) and ion density profile (centre) for centered IB heating of electrons are shown. T_x is well presented by SH ($T \propto x^{2/7}$ dashed line in top figure) even though the heat flux is reduced compared to SH and the ion density is not constant. The bottom plot shows the quasistationary electron heat flux.

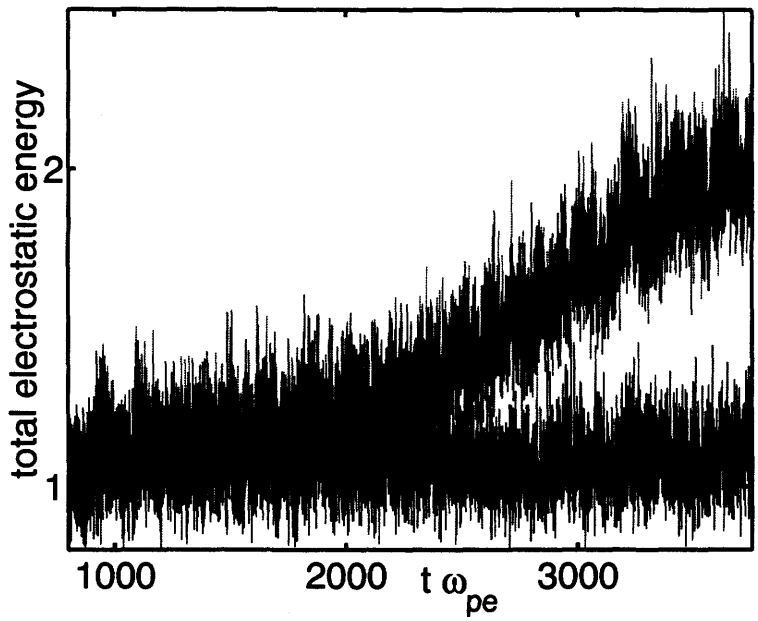

Figure 5.14 The evolution of the total electrostatic energy after a quasistationary state has been reached. For comparison the evolution of the energy without reinitialization of the ion temperature is shown (constant energy).

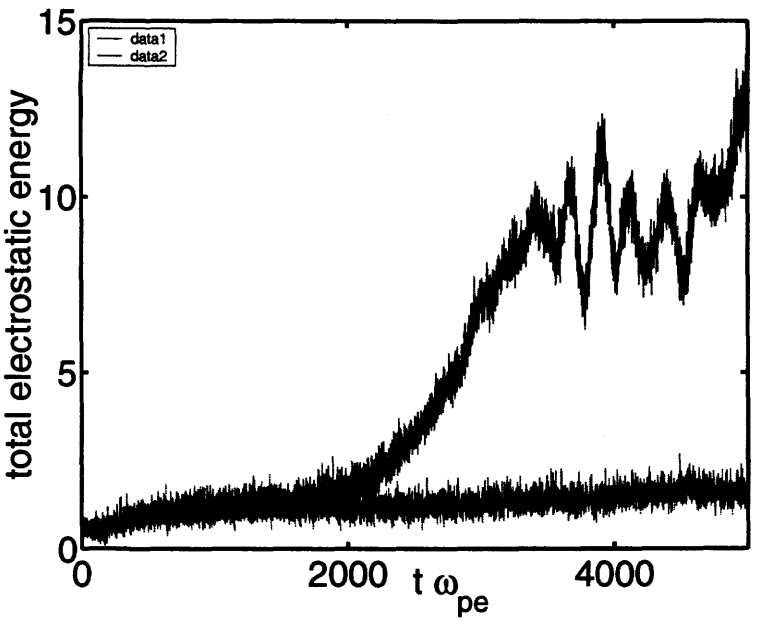

Figure 5.15 The evolution of the total electrostatic energy. For comparison the evolution of the energy with a hot ion temperature is shown (almost constant energy).

5.7 Preliminary RCI Simulations

Preliminary simulations of the return current instability are performed in two different ways. First, we wait for the plasma to reach the quasistationary state by suppressing instabilities. At this time the ion temperature is reinitialized to a low value to allow instabilities to develop. Figure 5.14 demonstrates the different evolution of the electrostatic energy compared to a run where instabilities are continued to be suppressed. Clearly, we can see the onset of a return current instability. The more realistic case is investigated by starting with a homogeneous temperature and density profile and IB heating in the centre with cold ions. In this case, the return current instability is more obvious as seen in Figure 5.15.

5.8 Conclusions

In this chapter, we verified the applicability of QNPIC for simulating ion acoustic dynamics in collisionless ion dynamics. The dispersion of the model has been derived and it is demonstrated to be similar with the complete electrostatic dispersion relation as it is usually derived. The difference is due to effects of the order of $k\lambda_{De}$, which are neglected in QNPIC. This limits the instability studies somewhat as the growth rate is biggest for large k.

The collisionless dispersion has been verified by simulations and experimental limits on the available wavelength have been established, which are due to smoothing effects of the weighting scheme and the quasineutral approximation. The effect of $e - i$ collisions on the damping has been esti-

mated and verified before studying instabilities. Two stream instabilities, with electrons streaming relative to the ions initially, have been studied in detail. The subsequent turbulence and enhanced heating, due to the turbulence, have been demonstrated. After deriving the return current instability, which is thought to be relevant in laser plasma experiments, inhomogeneous temperature profiles have been studied with respect to large scale ion motion and possible instabilities in configurations relevant to laser plasma experiments. Preliminary results suggest the existence of return current instability in the simulations for sufficiently large gradients and IB heating.

6. Kinetic Closure of Ion Hydrodynamic Equations

6.1 Introduction

When describing the state of a plasma system, we mostly use local thermodynamic quantities such as density, temperature etc. In the fluid description of plasmas these parameters, typically density, temperature and flow velocity, are advanced in time by a set of hydrodynamic equations analog to the fluid equations from neutral hydrodynamics with the addition of electromagnetic fields through Maxwell's equations. One of the key issues in the fluid description is the closure problem. Closure means having as many equations as unknowns, which, together with boundary and initial conditions, will determine the plasma evolution. Without taking special note of it, we have presented one such closure in Chapter 4, when discussing the heat flux as a function of the temperature.

In this chapter we will systematically review the closure problem as it occurs in the fluid hierarchy, and compute exact closures in the linear approximation for the ion dynamical evolution. The results are a set of fluid equations for ion dynamics with exact closures for the heat flux and the viscosity. The derived description is exact for all collisionality regimes of the linearized plasma system. An approach first used by Chang and Callen

[19] is further developed to include collisional effects. We will write ion evolution equations with kinetic closures for the ion heat flux and viscosity. These ensure the validity of the expressions for arbitrary collisionality, from the collisionless case, where wave-particle effects dominate, to strongly collisional plasmas. The closure presented here is obtained through a Chapman-Enskog like (CEL) approach by taking the appropriate moments of the full kinetic equation. The closure is exact in the sense that it is equivalent to solving the kinetic equation directly. The approximation is necessary to truncate the collision operator. In the collisionless limit the closure is exact, including kinetic effects such as Landau damping self-consistently into the fluid equations. The accuracy of the collisional limit is determined by the level at which the distribution, used in the collisional operator, is truncated. Braginskii [13] has calculated the collisional limit of the closures kinetically and noted that the accuracy increases significantly, if two moments higher than heat flux $\mathbf{q}$ and stress tensor $\boldsymbol{\pi}$ are included.

Kinetic closures (e.g. [19, 20]) have previously been developed with a simplified collision operator in the case of [19]. In the work by Zheng [61] the closure relations are expressed in terms of a fluctuating electric fields, whereas the CEL approach, employed in this work and in the work of Chang [19], describes them in terms of the lower fluid moments, just as is the case in Braginskii's closure relations. This appears to be a more appropriate approach. In certain analyses, it is desirable to neglect some fluctuations (e.g. flow fluctuation) and in the CEL approach the appropriate closure is immediately obtained, since they are already expressed in terms of fluid quantities. In Zheng's paper the corresponding change in the closure is not

immediately obvious, since it is expressed in terms of the electromagnetic potentials. This work uses the full ion-ion collision operator and will therefore also be useful for electron closures, where the same collision operator can be used.

The organization of this chapter is as follows. We begin by deriving the fluid equation hierarchy from the kinetic equation, and highlight the closure problem. Different simple closures are discussed, most of which assume a plasma with high collisionality, such that the mean free path between collisions is much smaller than any gradient scale length $\lambda_{mfp} \ll L$. Next, the systematic Chapman-Enskog approximate solution to the kinetic equation is outlined and results from Braginskii are summarized. These will form the reference case for collisional limits of the closures. The general method of an exact closure is discussed next. After writing down the fluid equation system in their exact form, the Chapman-Enskog kinetic equation is calculated, and the closures are expressed in terms of integrals of known functions and the collisional integrals. Ion heat flux and viscosity are written as functions of temperature gradient and flow.

The collisional operator is presented and a truncated version is computed that ensures accuracy in the collisional limit. After verifying that the collisionless closures agree with previously known results, the simplifying assumption of $ZT_e \gg T_i$, which is commonly encountered in laser plasmas, is used to find approximate solutions of the collisional integrals. We show that Braginskii's results for the collisional limits are reproduced correctly.

6.2 The Closure Problem

When using a fluid description of the plasma, local macroscopic parameters such as density, flow velocity and temperature are evolved in time by means of fluid equations. These are analogous to the equations in ordinary fluid dynamics. For a complete description of the plasma the set of fluid equations has to be closed together with appropriate boundary and initial conditions as well as with Maxwell's equations for the electromagnetic fields, such that the plasma evolution is completely described.

Fluid equations are systematically derived from a kinetic equation describing the evolution of the distribution function of the particle species $f(\mathbf{x}, \mathbf{v}, t)$. The moments of the distribution function determine the fluid quantities. We give the lowest three moments which have simple interpretations. First, we have the density,

$$n(\mathbf{x}, t) = \int d^3v f(\mathbf{x}, \mathbf{v}, t), \tag{6.1}$$

and the flux density,

$$n\mathbf{u}(\mathbf{x}, t) = \int d^3v f(\mathbf{x}, \mathbf{v}, t)\mathbf{v}. \tag{6.2}$$

The relative velocity $\mathbf{w} = \mathbf{v} - \mathbf{u}$ is used to define the pressure tensor as,

$$\mathbf{p} = \int d^3v f(\mathbf{x}, \mathbf{v}, t)m\mathbf{w}\mathbf{w}, \tag{6.3}$$

and the heat flux,

$$\mathbf{q}(\mathbf{x},t) = \int d^3v f(\mathbf{x},\mathbf{v},t)\frac{1}{2}mw^2\mathbf{w}. \tag{6.4}$$

The scalar pressure is found by taking the trace of the pressure tensor,

$$p = \frac{1}{3}Tr(\mathbf{p}), \tag{6.5}$$

and the kinetic temperature is then defined as,

$$T = \frac{p}{n}. \tag{6.6}$$

The viscosity tensor is defined as

$$\pi = \mathbf{p} - \frac{p}{3}\underline{\underline{\mathbf{I}}}. \tag{6.7}$$

The kinetic equation itself is,

$$\frac{\partial f}{\partial t} + \nabla \cdot (\mathbf{v}f) + \frac{\partial}{\partial \mathbf{v}} \cdot (\mathbf{a}f) = C(f), \tag{6.8}$$

where $\mathbf{a}$ is the acceleration due to the macroscopic electromagnetic field, which is caused by the averaged densities and currents, and C is a collision operator that accounts for microscopic correlations between single particles. The k-th moment equation is simply computed by multiplying the kinetic equation by $\mathbf{v}^k$ and integrating.

The infinite hierarchy of fluid equations is equivalent to the underlying

kinetic equation. To use a finite set of fluid equations, additional information is required. This can involve a small parameter, a limiting assumption or some additional physical input. The electric field is not discussed since it is always available through Maxwell's equations. The continuity equation is obtained by simply integrating over velocity space:

$$\frac{\partial n}{\partial t} + \nabla \cdot n\mathbf{u} = 0. \tag{6.9}$$

The momentum equation is obtained by multiplying by $\boldsymbol{v}$ and integrating:

$$mn\left(\frac{\partial \mathbf{u}}{\partial t} + \mathbf{u} \cdot \nabla \mathbf{u}\right) = en\mathbf{E} - \nabla p - \boldsymbol{\nabla} : \boldsymbol{\pi} + \mathbf{R}. \tag{6.10}$$

Here $p = nT$ and for $\boldsymbol{\pi}$ the viscous stress tensor a closure is required. $\mathbf{R}$ is the change in ion current due to collisions with other species. Finally, multiplying by v^2 and integrating results in the energy equation:

$$\frac{3}{2}n\left(\frac{\partial T}{\partial t} + \mathbf{u} \cdot \boldsymbol{\nabla} T\right) = -p\boldsymbol{\nabla} \cdot \mathbf{u} - \boldsymbol{\pi} : \boldsymbol{\nabla}\mathbf{u} - \boldsymbol{\nabla} \cdot \mathbf{q} + Q. \tag{6.11}$$

Q is the heating or cooling due to collisions with other species. The coupling to the next higher moment in each evolution equation constitutes the closure problem. If, for example, only the first equation is considered, we have one equation for four unknowns (density and three flow velocity components) and so on, if we include ever higher order evolution equations. For the set of Equations (6.9)-(6.11) closures are needed for $\boldsymbol{\pi}$ and $\mathbf{q}$.

6.2.1 Cold Plasma Approximation

A simple closure can be obtained from truncation by the assumption that some higher moments vanish. A typical example is the case of a cold plasma. In this case pressure and stress vanish, and the continuity equation and the momentum equation alone provide a closed set of fluid equations. We will use the cold ion assumption in the following chapter, when considering sheath stability.

6.2.2 Local Thermodynamic Equilibrium

Sometimes also a local thermal equilibrium (LTE) approximation is used. This is defined by

$$f = f_M = \frac{n}{(\sqrt{2\pi}v_t)^3} \exp\left(\frac{-(\mathbf{v}-\mathbf{u})^2}{2v_t^2}\right). \tag{6.12}$$

The Maxwellian f_M is determined by $n, T, \mathbf{u}$ hence viscosity and heat flow vanish and continuity, momentum and energy equation completely determine the plasma evolution. The LTE approximation puts strong restrictions on the usefullness of results. Assuming local Maxwellian requires frequent collisions. On the other hand, collision dominated transport and relaxation processes are neglected in LTE. Therefore, LTE can only be expected to provide reasonable results when the system is maintained extremely close to equilibrium.

6.2.3 Chapman-Enskog Theory

An asymptotic closure is a scheme which exploits a small parameter. By this, in principle, an estimate of the error is possible. A classic asymptotic closure using the ratio of mean-free-path to scale size is the Chapman-Enskog (CE) theory [62], which solves simplified kinetic equations for each order in the distribution function. First order solutions allow higher order moments, such as heat flux and viscosity, to be expressed in terms of density, flow velocity and temperature. The main ideas of CE theory will be reviewed in the following section.

The distribution function is assumed to be approximately Maxwellian $f^0 = f_M$, which is determined by the parameters $n, \mathbf{u}, T$, which are slowly varying functions of coordinates and time. These are the only parameters on which the solution f depends on throughout the plasma. The solution f itself is expanded in a series,

$$f = f^0 + f^1 + f^2 + ... \tag{6.13}$$

with increasing order in the ratio of mean-free-path to scale length. In the kinetic equation (electrostatic for simplicity) the dominant part is assumed to be the collisional term. All other terms with time and space derivatives and electric field are assumed small. In zeroth order, therefore, only the collision operator is considered. Since the Maxwellian distribution is the solution of the collision operator

$$C(f_M) = 0, \tag{6.14}$$

it follows that f_M is a valid solution of f^0. The collision term to first order considers $C(f^0, f^1) + C(f^1, f^0)$ linearized contributions. This can be solved for f^1. In the next order it is $C(f^0, f^2) + C(f^1, f^1) + C(f^2, f^0)$ which can be solved for f^2. In principle, any order of accuracy can be obtained by this procedure. However, higher orders become successively more difficult to solve.

Braginskii [13] uses CE theory in plasmas employing the Landau collision operator to first order to find $f^1(\mathbf{v})$ as function of the hydrodynamic forces $\nabla T, \nabla \mathbf{u}$ etc. From $f^1(\mathbf{v})$ heat flux and viscosity are computed which gives the desired closures. Braginskii avoids solving $C(f^0, f^1) + C(f^1, f^0)$ numerically by expanding f^1 in Laguerre polynomials as is done in the original work by Chapman and Enskog [62]. His conclusion is that the accuracy of the results increases sharply as that expansion in Laguerre polynomials is taken up to second order.

In this context, the moment approach is worth mentioning. It was first developed in the work of Grad [63] and in similar forms considered by Mikhailovski [64] and Balescu [65]. In this approach a hierarchy of evolution equation of hydrodynamic moments is derived from the kinetic equation. Within the collision operator the distribution function is expanded in the same hydrodynamic moments that are used in the evolution equation. A high collisionality assumption is made, that allows to drop certain time derivatives and spatial derivatives, to obtain a closed set of fluid equations, from which transport coefficients can be calculated. The 13-moment approximation moments are density, temperature and velocity vector (i.e., 5

quantities), as well as the heat flux vector $\mathbf{q}$ (3 quantities) and the viscosity tensor π (5 quantities since the viscosity tensor is symmetric and has zero trace). In the 21-moment approximation the 8 new moments are a second rank tensor π^*, similar to the viscosity tensor, and a vector $\mathbf{q}^*$, similar to the heat flux. Mikhailovski [64] and Balescu [65] note that in order to reproduce Braginskii's results one should take into account those two moments. This leads us to the assumption that also in collisional parts in the kinetic closure described below second order terms (π^* and $\mathbf{q}^*$) need to be included. Zheng [21] only included the first order terms and found large deviations from Braginskii in the collisional limit in the heat conductivity.

6.3 Outline of the Kinetic Closure Procedure

The starting points are the fluid equations for the density n, the flow velocity $\mathbf{u}$ and the plasma temperature T. These are standard MHD equations but with the current Chapman-Enskog Ansatz for the distribution function the fluid moments are given only by their definitions and do not necessarily retain their thermodynamical meaning. The kinetic information is contained within the moments and explicitly expressed in the closures for the viscosity $\boldsymbol{\pi}$ and the heat flux $\mathbf{q}$. The deviation $\tilde{F}$ of the total distribution from Maxwellian is used to calculate the closures. In the Chapman-Enskog Ansatz the lower order moments serve as driving forces in the kinetic equation. Linearizing the Chapman-Enskog kinetic equation allows to solve for $\tilde{F}$ exactly, and the closures are recovered by direct calculation of the higher moments $\mathbf{q}$ and $\boldsymbol{\pi}$.

6.4 Chapman-Enskog Kinetic Equation

The kinetic equation is

$$\frac{\partial f}{\partial t} + \mathbf{v} \cdot \boldsymbol{\nabla} f + \frac{e}{m} \mathbf{E} \cdot \boldsymbol{\nabla}_v f = C(f), \tag{6.15}$$

where C is short for all collisional contributions (two or more particle correlations). We consider a fully ionized plasma in which collisions with neutrals can be neglected. For ion dynamics it is also valid to neglect effects of collisions with electrons because of the large mass ratio. We will therefore limit the collisional effects to ion-ion $(i - i)$ collisions.

The ion distribution is separated into a drifting Maxwellian and a remainder $f = f_M + F$ where

$$f_M = n(\mathbf{x}, t) \left(\frac{m}{2\pi T(\mathbf{x}, t)} \right)^{3/2} \exp \left(- \frac{(m(\mathbf{v} - \mathbf{u}(\mathbf{x}, t))^2}{2T(\mathbf{x}, t)} \right). \tag{6.16}$$

The drifting Maxwellian contains the three lowest moments $n, \mathbf{u}, T$ which are conserved in $i - i$ collisions. The remainder F contains all kinetic effects and contributions from higher moments. From here on, the procedure is to substitute f into the kinetic Equation (6.15) and solve for F. The contributions of the Maxwellian in Equation (6.15) are shown below

$$\frac{\partial f_M}{\partial t} = \frac{1}{n} \frac{\partial n}{\partial t} f_M + \frac{\partial T}{\partial t} \frac{1}{T} \left(\frac{m v'^2}{2T} - \frac{3}{2} \right) f_M + \frac{m}{T} \mathbf{v}' \cdot \frac{\partial \mathbf{u}}{\partial t} f_M, \tag{6.17}$$

where $\mathbf{v}' = \mathbf{v} - \mathbf{u}$.

$$\nabla f_M = \frac{\nabla n}{n} f_M - \frac{3}{2}\frac{\nabla T}{T} f_M + \frac{m v'^2}{2T}\frac{\nabla T}{T} f_M + \frac{m}{T}\mathbf{v}' \cdot \nabla \mathbf{u} f_M, \tag{6.18}$$

$$\nabla_v f_M = -\frac{m v'^2}{T} f_M. \tag{6.19}$$

The time derivatives of the moments n, T and $\mathbf{u}$ are replaced by the linearized fluid equations. The contribution to the kinetic equation due to the Maxwellian part is

$$\begin{aligned} \frac{df_M}{dt} + \frac{e}{m}\mathbf{E} \cdot \nabla_v f_M \;=\; & \frac{m}{T}\left(\mathbf{v}'\mathbf{v}' - \frac{v'^2}{3}\underline{\mathbf{I}}\right) : \nabla \mathbf{u} f_M \\ & -\mathbf{v}' \cdot (\nabla \cdot \boldsymbol{\pi} - \mathbf{R})\frac{f_M}{p} \\ & -\left(\frac{m v'^2}{3T} - 1\right)(\boldsymbol{\pi} : \nabla \mathbf{u} + \nabla \cdot \mathbf{q} - Q)\frac{f_M}{p} \\ & +\left(\frac{m v'^2}{2T} - \frac{5}{2}\right)\mathbf{v}' \cdot \nabla T \frac{f_M}{T}, \end{aligned} \tag{6.20}$$

which is the kinetic equation for the Maxwellian in term of fluid moments. $\boldsymbol{\pi}$ is separated into a parallel and a perpendicular component. Perpendicular components are assumed second order and neglected from here on. Similarly, it is assumed that the heat flux is predominantly parallel, and perpendicular components are neglected. The same assumptions is applied to all other gradients and vectors.

The equation determining F is obtained by taking the Fourier transform and substituting Equation (6.20) for the parts involving the Maxwellian

contribution into (6.15)

$$\begin{aligned}(\omega - k_{\|}v_{\|})\,F - iC(f) \;=\; & k_{\|}u_{\|}\frac{f_M}{v_t^2}\frac{2}{3}\left(v_{\|} - \frac{v_{\perp}^2}{2}\right) \\ & -\frac{2}{3}k_{\|}\pi v_{\|}\frac{f_M}{p} - iv_{\|}R\frac{f_M}{p} \\ & -k_{\|}q\frac{f_M}{p}\frac{2}{3}\left(\frac{v^2}{2v_t^2} - \frac{3}{2}\right) \\ & -iQ\frac{f_M}{p}\frac{2}{3}\left(\frac{v^2}{2v_t^2} - \frac{3}{2}\right) \\ & -iv_{\|}\frac{\nabla_{\|}T}{T}f_M\left(\frac{v^2}{2v_t^2} - \frac{5}{2}\right) \qquad (6.21)\end{aligned}$$

where $v_t^2 = \frac{T}{m}$.

The collision operator still remains in its general form and will be considered in detail later. For now it suffices to know that through a truncation scheme it is known in principle and can be expressed by fluid moments.

6.5 Closing the MHD Equations

We solve Equation (6.21) for F. Taking moments of F will then yield equations linear in the fluid moments. These will be solved for the desired closure coefficients. The moments are defined in terms of Laguerre and Legendre polynomials. We give definitions of q^* and π^* which will occur in the discussion of the collisional operator.

$$\pi = m\int P_2(\mu)v^2L_0^{5/2}F dv, \qquad (6.22)$$

$$\pi^* = m\int P_2(\mu)v^2L_1^{5/2}F dv, \qquad (6.23)$$

$$q = T \int P_1(\mu) v L_1^{3/2} F dv, \tag{6.24}$$

$$q^* = T \int P_1(\mu) v L_2^{3/2} F dv. \tag{6.25}$$

The Laguerre polynomials are

$$L_0^{5/2} = 1, \tag{6.26}$$

$$L_1^{5/2} = \left(\frac{v^2}{2v_t^2} - \frac{7}{2} \right), \tag{6.27}$$

$$L_1^{3/2} = \left(\frac{v^2}{2v_t^2} - \frac{5}{2} \right), \tag{6.28}$$

$$L_2^{3/2} = \left(\frac{v^4}{4v_t^4} - \frac{7v^2}{2v_t^2} + \frac{35}{4} \right), \tag{6.29}$$

and will be used like this in the expansion of the collisional operator. Denoting the collisional contributions of moment x by C_x we summarize for F with $\xi = \frac{\omega}{k_{||} v_t}$, where all velocities in units of v_t

$$\begin{aligned}
(\xi - v_{||})F \;=\; & u_{||} f_M \frac{2}{3} v^2 P_2(\mu) \\
& -i \frac{\nabla_{||} T}{T} \frac{f_M}{k_{||}} v_{||} \left(\frac{v^2}{2} - \frac{5}{2} \right) \\
& -\pi \left(\frac{2}{3} \frac{f_M}{p} v P_1(\mu) - \frac{iC_\pi}{k_{||}} \right) \\
& -q \left(\frac{f_M}{p v_t} \frac{2}{3} \left(\frac{v^2}{2} - \frac{3}{2} \right) - \frac{iC_q}{k_{||}} \right) \\
& +\pi^* \frac{iC_{\pi^*}}{k_{||}} + q^* \frac{iC_{q^*}}{k_{||}},
\end{aligned} \tag{6.30}$$

(6.31)

The exact forms of the C_x are given in the following section.

6.6 Collisional Operator

The collisional effects on the left hand side of the kinetic Equation (6.13) are due to the fundamental graininess of the medium. They manifest themselves through Coulomb scattering of each of the discrete charges of each other. A rigorous derivation of the correlations can be found, for example, in the work of Klimontovich [34].

For most applications in plasma theory, it is assumed that the effect of charged-particle interactions is adequately described by a Fokker-Planck equation. A general feature of the collision operator is conservation of particles, momentum and energy locally. If $C_{ss'}$ denotes the collision effects on species s due to species s', then the conservation laws have the form

$$\int d^3v C_{ss'} = 0, \tag{6.32}$$

$$\int d^3v m_s \mathbf{v} C_{ss'} = -\int d^3v m_{s'} \mathbf{v} C_{s's}, \tag{6.33}$$

$$\int d^3v \frac{1}{2} m_s v^2 C_{ss'} = -\int d^3v \frac{1}{2} m_{s'} v^2 C_{s's}. \tag{6.34}$$

If we demand these requirements of the collision operator and only consider $i - i$ collisions in the ion dynamics, the friction term $\mathbf{R}$ in the momentum equation and the heating term Q in the energy equation vanish.

6.6.1 Ion-ion Collision Operator

The form of the collision operator in a plasma is explained in detail in [66]. It is referred to as the Landau collision operator and is formally written as a Fokker-Planck equation:

$$C(f,f) = -\Gamma_{ii}\nabla_v \cdot \left(f\nabla_v H - \frac{1}{2}\nabla_v \cdot f\nabla_v\nabla_v G \right), \tag{6.35}$$

where H and G are the Rosenbluth potentials of f, and Γ_{ii} is the collision strength parameter.

$$H(\mathbf{v}) = 2\int \frac{f(\mathbf{v}')}{|\mathbf{v}-\mathbf{v}'|}d\mathbf{v}', \tag{6.36}$$

$$G(\mathbf{v}) = \int f(\mathbf{v}')|\mathbf{v}-\mathbf{v}'|d\mathbf{v}', \tag{6.37}$$

$$\Gamma_{ii} = \frac{4\pi Z^4 e^4 \ln\Lambda}{m_i^2}. \tag{6.38}$$

In the linear approximation the distribution is assumed to be Maxwellian plus a small perturbation similar as before,

$$f = f_M + \tilde{f}. \tag{6.39}$$

The Maxwellian contains perturbations in $n, \mathbf{u}$ and T since these plasma parameters are conserved by $i-i$ collisions. Working in spherical coordinates $\zeta = v/v_t$ and $\mu = v_\parallel/v$ the linearized collision term can then be simplified (see e.g. [67]),

$$C\left(f_M,\tilde{f}\right) = \Gamma_{ii}\left(4\pi\tilde{f} - \frac{1}{2v_t^2}H_{01} + \frac{\zeta^2}{2v_t^4}\frac{\partial^2 G_{01}}{\partial\zeta^2}\right) f_M, \tag{6.40}$$

$$C\left(\tilde{f}, f_M\right) = -\frac{\Gamma_{ii}}{\zeta^2 v_t^2}\frac{\partial}{\partial\zeta}\left[\frac{\zeta}{2}\frac{\partial H_{10}}{\partial\zeta}\exp -\frac{\zeta^2}{2}\frac{\partial}{\partial\zeta}\left(\exp\frac{\zeta^2}{2}\tilde{f}\right)\right] + \frac{\Gamma_{ii}}{2\zeta^3 v_t^4}\frac{\partial G_{10}}{\partial\zeta}\left[\frac{\partial}{\partial\mu}(1-\mu^2)\frac{\partial\tilde{f}}{\partial\mu}\right], \tag{6.41}$$

where (H_{01}, G_{01}) and (H_{10}, G_{10}) refer to the Rosenbluth potentials of the perturbed $\tilde{f}$ and the background Maxwellian f_M ion distribution functions, respectively. The Maxwellian Rosenbluth potentials can be calculated as

$$\frac{\partial H_{10}}{\partial\zeta} = \frac{2n_i}{\zeta^2 v_t}\left[\sqrt{2/\pi}\zeta e^{-\zeta^2/2} - \Phi\left(\zeta/\sqrt{2}\right)\right], \tag{6.42}$$

$$\frac{\partial G_{10}}{\partial\zeta} = n_i v_t \Theta\left(\zeta/2\right), \tag{6.43}$$

where $\Phi(x)$ is the error function and $\Theta(x)$ is the Chandrasekhar function [65]. Legendre polynomials are eigensolutions of the angular operator in Equation (6.41). It is therefore standard to expand $\tilde{f}$ in a series of Legendre polynomials P_l,

$$\tilde{f}(v,\nu) = \sum_{l=0}^{\infty} a_l(v) P_l(\nu). \tag{6.44}$$

For each Legendre polynomial term the Rosenbluth potential terms can be calculated ([67])

$$H_l = \frac{8\pi v_t^2}{(2l+1)\zeta}\left[\frac{1}{\zeta^l}\int_0^{\zeta} a_l(t)t^{2+l}dt + \zeta^{l+1}\int_{\zeta}^{\infty} a_l(t)t^{1-l}dt\right], \tag{6.45}$$

$$\frac{\partial^2 G_l(\zeta)}{\partial \zeta^2} = -\frac{4\pi v_t^4}{(4l^2-1)}\left[\int_0^{\zeta} a_l(t)t^{2+l}\left(\frac{l(l-1)}{\zeta^{l+1}} - \frac{(l+1)(l+2)(l-1/2)t^2}{(l+3/2)\zeta^{l+3}}\right)dt \right.$$
$$\left. + \int_{\zeta}^{\infty} \frac{a_l(t)}{t^{l-3}}\left(l(l-1)\zeta^{l-2} - \frac{(l+1)(l+2)(l-1/2)\zeta^l}{(l+3/2)t^2}\right)dt\right] \tag{6.46}$$

6.6.2 Truncated Collision Operator

To obtain an analytic result of the collision operator, we expand the distribution function in a series of Legendre and Laguerre polynomials in μ and ζ (or v) similar as above. The series in μ in Legendre polynomials is truncated after second order. The Laguerre series is truncated at third order, leaving four contributing moments q, q^* and π, π^*. The moments $\mathbf{u}$ and T vanish in the collisional integral because of momentum and energy conservation in ion-ion collisions. The expansion looks as follows

$$f = f_M(1+\Phi), \tag{6.47}$$

$$f_M = \frac{n}{(2\pi v_t^2)^{3/2}} \exp\left(-\frac{v^2}{2v_t^2}\right). \tag{6.48}$$

The expansion is

$$\Phi = \frac{1}{3}\mathrm{P}_2(\mu)v^2\pi + \frac{1}{42}\mathrm{P}_2(\mu)\pi^* + \frac{1}{10}\mathrm{P}_1(\mu)v(v^2-5)q + \frac{1}{70}\mathrm{P}_1(\mu)v\left(\frac{v^4}{2} - 7v^2 + \frac{35}{2}\right)q^*. \tag{6.49}$$

Note that the Maxwellian above Equation (6.48) is local, that is, $v_t(x)$ and $n(x)$ are function of coordinate, and the velocity is the random velocity $|\mathbf{v} - \mathbf{u}(x)|$, which is separated from the local flow.

The collisional operator is calculated utilizing the computer algebra package Maple. The resulting expressions are,

$$C\left(f_M P_1(\mu) v\left(v^2-5\right)\right)/P_1(\mu) = 20\frac{\Phi\left(\frac{v}{\sqrt{2}}\right)}{v^2} - 4\Phi\left(\frac{v}{\sqrt{2}}\right) - 20\sqrt{\frac{2}{\pi}}\frac{1}{v}\exp\left(-\frac{v^2}{2}\right), \tag{6.50}$$

$$\begin{aligned} C\left(f_M P_1(\mu) v\left(\frac{v^4}{2} - 7v^2 + \frac{35}{2}\right)\right)/P_1(\mu) \;&=\\ -63\frac{\Phi\left(\frac{v}{\sqrt{2}}\right)}{v^2} - 3v^2\Phi\left(\frac{v}{\sqrt{2}}\right) + 36\Phi\left(\frac{v}{\sqrt{2}}\right)&\\ -35\sqrt{\frac{2}{\pi}}v\exp\left(-\frac{v^2}{2}\right) + 63\sqrt{\frac{2}{\pi}}\frac{1}{v}\exp\left(-\frac{v^2}{2}\right),& \end{aligned} \tag{6.51}$$

$$C\left(f_M P_2(\mu) v^2\right)/P_2(\mu) = -4\frac{\Phi\left(\frac{v}{\sqrt{2}}\right)}{v} - +16\frac{\Phi\left(\frac{v}{\sqrt{2}}\right)}{v^3} - 16\sqrt{\frac{2}{\pi}}\frac{1}{v^2}\exp\left(-\frac{v^2}{2}\right), \tag{6.52}$$

$$C\left(f_M P_2(\mu) v^2\left(v^2-7\right)\right)/P_2(\mu) \;=\; 30\frac{\Phi\left(\frac{v}{\sqrt{2}}\right)}{v} - 5v\Phi\left(\frac{v}{\sqrt{2}}\right) + 29\frac{\Phi\left(\frac{v}{\sqrt{2}}\right)}{v^3} - 49\sqrt{\frac{2}{\pi}}\exp\left(-\frac{v^2}{2}\right) - 29\sqrt{\frac{2}{\pi}}\frac{1}{v^2}\exp\left(-\frac{v^2}{2}\right), \tag{6.53}$$

where v is normalized to units of v_t.

So the moments to be included in F are

$$C_q \;=\; -\Gamma_{ii}\frac{f_M}{nTv_t}\frac{2}{5}v_{||}\left[\frac{5}{v^2}\sqrt{\frac{2}{\pi}}\exp\left(-\frac{v^2}{2}\right) + \frac{1}{v}\Phi\left(\frac{v}{\sqrt{2}}\right) - \frac{5}{v^3}\Phi\left(\frac{v}{\sqrt{2}}\right)\right], \tag{6.54}$$

$$C_{q^*} \;=\; -\Gamma_{ii}\frac{f_M}{nTv_t}\frac{1}{70}v_{||}\left[35\sqrt{\frac{2}{\pi}}\exp\left(-\frac{v^2}{2}\right) - \frac{63}{v^2}\sqrt{\frac{2}{\pi}}\exp\left(-\frac{v^2}{2}\right) + 3v\Phi\left(\frac{v}{\sqrt{2}}\right) - \frac{36}{v}\Phi\left(\frac{v}{\sqrt{2}}\right) + \frac{63}{v^3}\Phi\left(\frac{v}{\sqrt{2}}\right)\right], \tag{6.55}$$

$$C_\pi \;=\; -\Gamma_{ii}\frac{f_M}{nT}\frac{4}{3}\mathrm{P}_2(\mu)\left[\frac{4}{v^2}\sqrt{\frac{2}{\pi}}\exp\left(-\frac{v^2}{2}\right) + \frac{1}{v}\Phi\left(\frac{v}{\sqrt{2}}\right) - \frac{4}{v^3}\Phi\left(\frac{v}{\sqrt{2}}\right)\right], \tag{6.56}$$

$$C_{\pi^*} = \tag{6.57}$$
$$-\Gamma_{ii}\frac{f_M}{nT}\frac{1}{42}\mathrm{P}_2(\mu)\left[49\sqrt{\frac{2}{\pi}}\exp\left(-\frac{v^2}{2}\right)+\frac{29}{v^2}\sqrt{\frac{2}{\pi}}\exp\left(-\frac{v^2}{2}\right)\right.$$
$$\left.+\frac{5}{v}\Phi\left(\frac{v}{\sqrt{2}}\right)-\frac{30}{v^3}\Phi\left(\frac{v}{\sqrt{2}}\right)-\frac{29}{v^5}\Phi\left(\frac{v}{\sqrt{2}}\right)\right].$$

6.7 Closed Set of Linear Equations in Fluid Moments

Taking the following moments we obtain a closed set of linear equations. This allows $\boldsymbol{\pi}$ and $\mathbf{q}$ to be expressed in terms of $\mathbf{u}$ and ∇T.

$$\begin{pmatrix} 1-M_{\pi\pi} & -M_{\pi q} & -M_{\pi\pi^*} & -M_{\pi q^*} \\ -M_{q\pi} & 1-M_{qq} & -M_{q\pi^*} & -M_{qq^*} \\ -M_{\pi^*\pi} & -M_{\pi^* q} & 1-M_{\pi^*\pi^*} & -M_{\pi^* q^*} \\ -M_{q^*\pi} & -M_{q^* q} & -M_{q^*\pi^*} & 1-M_{q^* q^*} \end{pmatrix} \begin{pmatrix} \pi \\ q \\ \pi^* \\ q^* \end{pmatrix} = \begin{pmatrix} M_{\pi u} & M_{\pi T} \\ M_{qu} & M_{qT} \\ M_{\pi^* u} & M_{\pi^* T} \\ M_{q^* u} & M_{q^* T} \end{pmatrix} \begin{pmatrix} u_{\|} \\ \frac{\nabla_{\|} T}{T} \end{pmatrix}, \tag{6.58}$$

which is then transformed into

$$\begin{pmatrix} 1 & 0 & 0 & 0 \\ 0 & 1 & 0 & 0 \\ 0 & 0 & 1 & 0 \\ 0 & 0 & 0 & 1 \end{pmatrix} \begin{pmatrix} \pi \\ q \\ \pi^* \\ q^* \end{pmatrix} = \begin{pmatrix} A_V & A_T \\ B_V & B_T \\ C_V & C_T \\ D_V & D_T \end{pmatrix} \begin{pmatrix} u_{\|} \\ \frac{\nabla_{\|} T}{T} \end{pmatrix}. \tag{6.59}$$

In a 13-moment approximation the system reduces to a 2×2 matrix. To discuss the physical meanings we rewrite the closed equations for π and q as

$$\pi_{||} = -n_0 m_i \nu_{||} i k_{||} u_{||} - l n_0 \nabla_{||} T, \tag{6.60}$$

$$q_{||} = -hpu_{||} - n_0 \kappa_{||} \nabla_{||} T. \tag{6.61}$$

This way we obtained expressions for viscosity and heat conductivity and the two less used coefficients l and h as functions of ω and k. The relations are

$$\nu_{||} = i\frac{v_t}{3k_{||}} A_V, \quad l = -\frac{2}{3} A_T, \tag{6.62}$$

$$\kappa_{||} = i\frac{v_t}{k_{||}} B_T, \quad h = -B_V. \tag{6.63}$$

The relations of the transport coefficients for $\boldsymbol{\pi}^*$ and $\mathbf{q}^*$ will not be discussed since they are not used in practice.

6.8 Collisionless Closures

In the collisionless limit of $\Gamma_{ii} = 0$, the closures can be calculated exactly. The results reduce to the previously published [19] and are listed in the appendix. Figure (6.1) shows real and imaginary parts of the collisionless parallel viscosity $\eta_{||}$ and the collisionless parallel ion heat conduction coefficients $\kappa_{||}$. Chang [19] and Hammett [20] developed simpler approximations involving fewer terms of the plasma dispersion function $Z(\xi)$. We developed a fast numerical routine that evaluates $Z(\xi)$ for arbitrary values of ξ based on integral relations for $Z(\xi)$ [68]. This makes all evaluations of the collisionless terms very fast compared to the collisional ones which

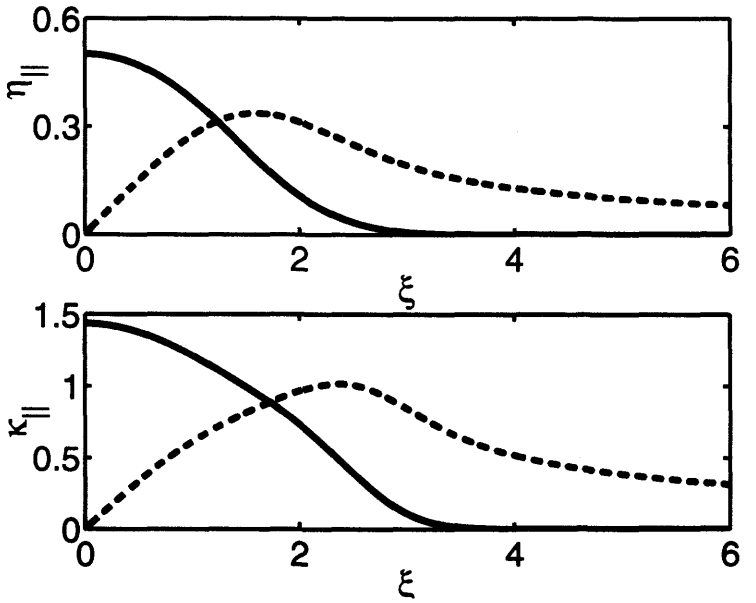

Figure 6.1 Real (solid lines) and imaginary (dashed lines) part closures for $k_{||} = 1$ as function of normalized frequency $\xi = \frac{\omega}{k_{||} v_t}$

require integrations. Therefore, simplified expressions for collisionless terms are not required for faster calculations of closures.

6.9 Simplified Expressions for $ZT_e \gg T_i$

Neglecting $e - e$ collisions in the description means $c_s \gg v_t$, or alternatively $ZT_e \gg T_i$. In this limit, the singular term in the integrals can be approximated by

$$\frac{1}{\xi - v_{||}} = \frac{1}{\xi}\left(1 + \frac{v_{||}}{\xi}\right) + i\pi\delta(\xi - v_{||}). \tag{6.64}$$

The second term proportional to $v_{||}/\xi$ is considered in those cases where the first term vanishes. This corresponds to the limit $\omega \gg kv_t$, which is true for ion acoustic waves in most relevant cases. The intermediate collisional regime can now be calculated exactly, using the developed closures. Numerical evaluation of the collisional moments is done once for the whole range of ξ, and then the closures can be easily calculated for any collisionality by a simple matrix inversion, since all collisional contributions are proportional to the previously defined collisional strength parameter Γ_{ii}. The simplified collisional integrals are summarized in the appendix. Figure

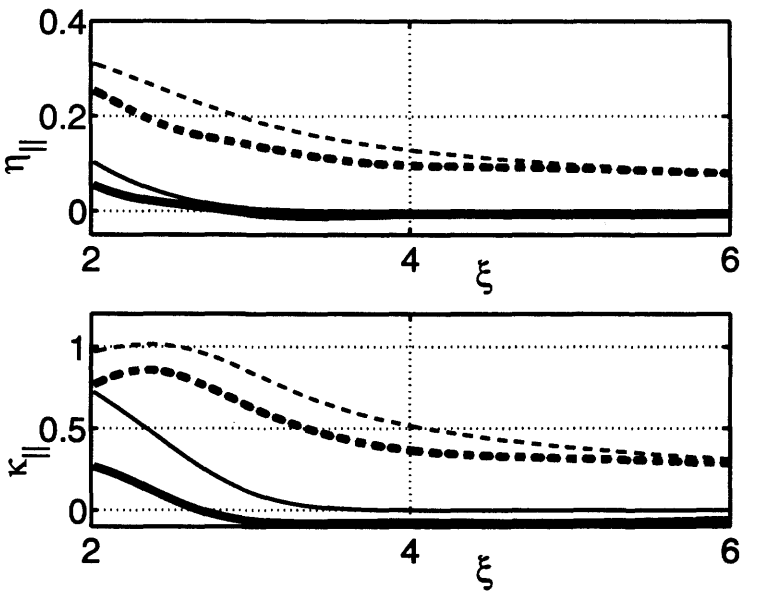

Figure 6.2 The real (solid lines) and imaginary (dashed lines) parts of the closures for $k_{||} = 1$ are shown as functions of the normalized frequency $\xi = \frac{\omega}{k_{||}v_t}$ for $\Gamma_{ii} = 1$. The thinner lines correspond to $\Gamma_{ii} = 0$ case.

(6.2) demonstrates the reduction of the transport coefficients compared to

the collisionless values (thin lines). Closures are calculated for values of $\xi \geq 2$, which is due to the simplifying assumption of "fast" waves compared to the ion thermal velocity.

6.10 Asymptotic Limit

In the limit of strong collisions, $\nu_{ii} \gg \omega \gg k_{||} v_t$, we recover Braginskii's limit correctly, if the 21-moment expansion in the collision operator is used. Braginskii [13] thermal parallel conductivity is $3.906 \times 3\sqrt{\pi} v_t^5 / \Gamma_{ii} = 20.77 v_t^5 / \Gamma_{ii}$. The Braginskii viscosity is $-0.96 \times 3\sqrt{\pi} v_t^3 T / \Gamma_{ii} = -5.1 v_t^3 T / \Gamma_{ii}$.

Figures 6.3 and 6.4 show the viscosity transport coefficient and the heat

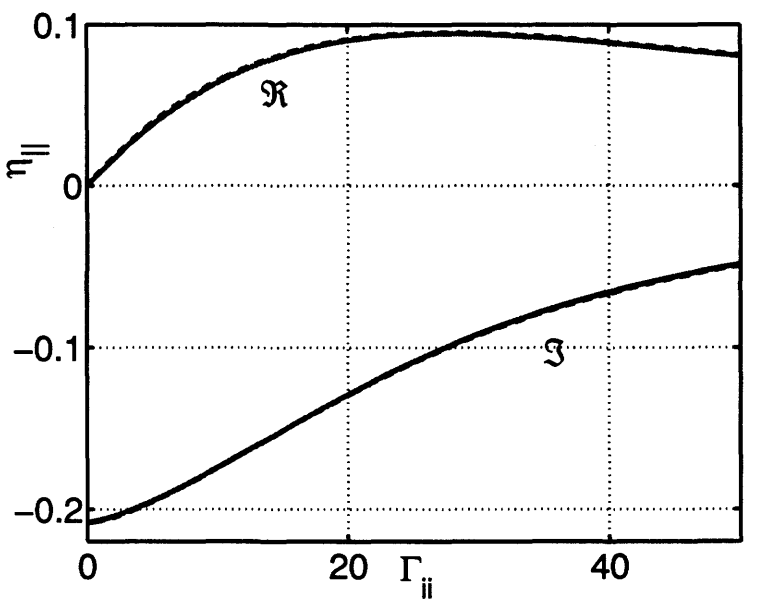

Figure 6.3 The real $\Re$ and imaginary $\Im$ part of $\eta_{||}$ for $k_{||} = 1$ are shown as functions of the collisional strength parameter Γ_{ii}. The solid lines correspond to 21 moments and the dashed lines to 13 moments.

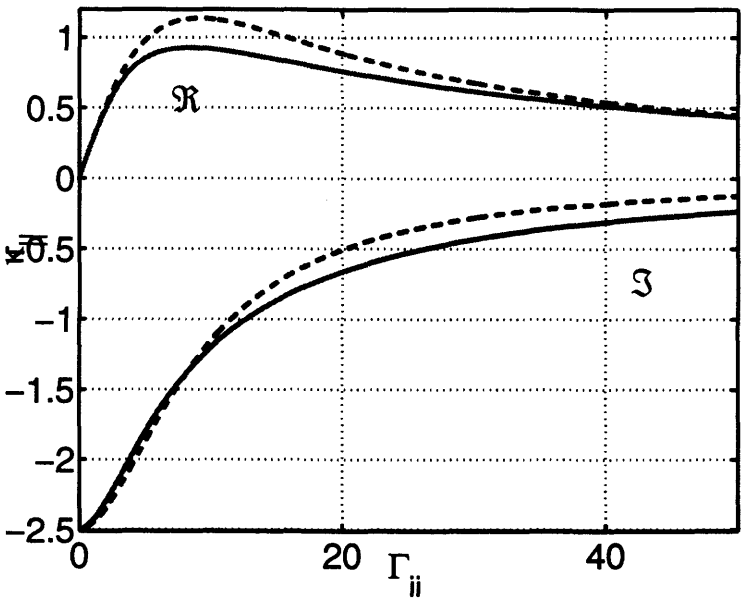

Figure 6.4 The real $\Re$ and imaginary $\Im$ part of $\kappa_{||}$ for $k_{||} = 1$ are shown as function of the collisional strength parameter Γ_{ii}. The solid lines correspond to 21 moments and the dashed lines to 13 moments.

conductivity as functions of the collisional strength parameter Γ_{ii} for $k_{||} = 1$ and $\xi = 4$. Viscosity is well represented with 13 moments but the heat conductivity changes significantly if 21 moments are used.

6.11 Conclusions

We have used a Chapman-Enskog like procedure to derive kinetic closures for the linearized fluid equations of an ion plasma. The closures are expressed as transport coefficients for the heat flow and viscous stress in terms of temperature gradient and plasma flow velocity. Within the collision operator the distribution function is expanded up to the moments of

energy weighted heat flow and energy weighted viscosity. This accuracy was found to be necessary to agree with classical results from Braginskii [13] in the collisional limit. The closures are calculated explicitly for the approximation that $ZT_e \gg T_i$, which is the case in most laser produced plasmas. Overall, an exact description of the plasma in the linearized case is found, which uses fluid equations, that take account of kinetic and collisional effects, for arbitrary ratio of mean-free-path to scale length.

7. Stability Analysis of Transverse Ion Modes

7.1 Introduction

In a plasma, a wide variety of nonlinear phenomena can occur. To this point we have studied transport and ion dynamics, with the motivation in mind that these are important for several classes of nonlinear phenomena. These are in particular resonant interactions among waves, which lead to exchange of energy between modes and parametric interactions (stimulated Raman and stimulated Brillouin scattering). For the study of nonlinear waves the relatively simple fluid description of ion acoustic waves provides a rich field in itself. Some of the results are used to obtain a better description of parametric instabilities. For example, stimulated Brillouin scattering in regimes of nonlinear ion acoustic waves has been elaborated by Rozmus[69].

This chapter is devoted to a generalization of a stability analysis developed by Petviashvili and Kadomtsev [70]. They studied solitons as a special class of nonlinear wave phenomena and use a general procedure to determine the stability of solitons to transverse oscillations (transverse to direction of propagation of the soliton). We generalize the procedure to general nonlinear potentials, which can occur in various plasma environments. As a test case, we choose the plasma-wall boundary region. For further

generalization, a second electron species with a different temperature is introduced. This situation is relevant for laser plasmas, where hot electrons travel ahead from laser heated hot spots into colder plasma regions. It may also apply in ionospheric plasmas, where hot electrons travel down magnetic field lines into colder plasmas. For certain parameters, these configurations lead to a double layer [71, 72]. In this case transverse modes are found that approach zero phase velocity.

7.2 Fluid Ion Acoustic Waves

In this chapter ion dynamics are studied in their simplest fluid form neglecting ion kinetic effects and electron inertia and collisional effects. We assume cold collisionless ions which can be described by the continuity equation and the momentum conservation equation,

$$\frac{\partial n}{\partial t} + \nabla \cdot n\mathbf{u} = 0, \tag{7.1}$$

$$\frac{\partial \mathbf{u}}{\partial t} + \mathbf{u} \cdot \nabla \mathbf{u} + \frac{e}{m}\nabla\varphi = 0. \tag{7.2}$$

These fluid equations are already closed since the assumption of cold ions eliminates higher moments. Electrons are also considered collisionless and also "hot", meaning $v_{te} \gg \omega/k$, compared to ion sound fluctuations. The electron thermal velocity is much larger than flows $v_{te} \gg u$. Thus, the electron momentum equation reads:

$$\frac{e}{m}\nabla\phi = \frac{1}{n}\nabla(nT). \tag{7.3}$$

The simple Boltzmann relation for electrons that relates density and potential can be derived,

$$n = n_0 exp\left(\frac{e\phi}{T}\right). \tag{7.4}$$

The description of the ion dynamics is then completed by Poisson's equation

$$\Delta\varphi = 4\pi e(n_0 \exp(\varphi) - n). \tag{7.5}$$

To lighten notation we use the following normalizations in the remaining sections. The electrostatic potential is expressed in units T_e/e, distances in $\lambda_{De} = \sqrt{T_e/4\pi e^2 n_0}$, velocity in a sound velocity $c_s = \sqrt{T_e/M_i}$ and time in an ion plasma period $\omega_p = \sqrt{4\pi e^2 n_0/M_i}$.

7.3 Stationary System

Since we are interested in highly inhomogeneous systems (e.g plasma sheath), we must first consider the stationary solution on which perturbations are allowed to occur. Density, flow and potential of the equilibrium system are denoted by capital letters. They are obtained by setting all time derivatives to zero. Furthermore, a plane geometry with all inhomogeneities in z-direction is considered.

$$\frac{\partial NU}{\partial z} = 0, \tag{7.6}$$

$$\frac{\partial}{\partial z}\left(\frac{U^2}{2} + \Phi\right) = 0, \tag{7.7}$$

$$\frac{\partial^2 \Phi}{\partial z^2} - \exp(\Phi) + N = 0, \tag{7.8}$$

The boundary conditions are defined in the bulk at $z = \infty$. At $z = \infty$ the potential vanishes $\Phi = 0$, the normalized density is 1 and the normalized flow is a which is the Mach number of the system and is a free parameter. For a sheath to exist the requirement is $a > 1$. For a simple discussion see for example the book of Chen [29]. We can then solve for U and N.

$$U = \sqrt{a^2 - 2\Phi} \qquad N = 1/\sqrt{1 - \frac{2\Phi}{a^2}}. \tag{7.9}$$

Poisson's equation can be integrated once using these boundary conditions to yield

$$\frac{1}{2}\Phi_z^2 = \left[\exp \Phi + a\,(U - a)\right], \tag{7.10}$$

where $\Phi_z = \partial\Phi/\partial z$.

In analogy to classical mechanics where

$$\frac{1}{2}m\left(\frac{dx}{dt}\right)^2 - (E - V(x)) = 0, \tag{7.11}$$

describes a particle moving in a potential V, one can think of Φ moving in a general potential $\Psi(\Phi)$, where Ψ is defined by Equation (7.10) and called Sagdeev potential. The form of the Sagdeev potential allows us to make qualitative statements about the solutions.

Figure 7.1 shows the Sagdeev potential of Equation (7.10). We can see that for $\Phi > 0$ bound "orbits" exist. If the potential starts at zero

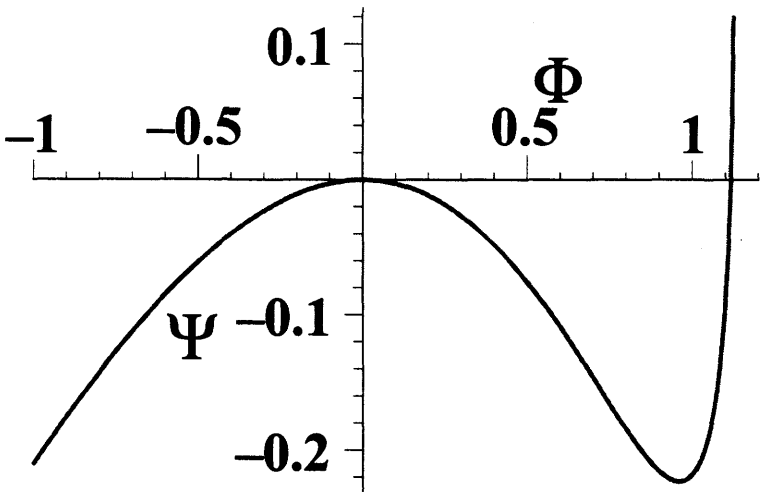

Figure 7.1 Sagdeev potential for single ion and single electron species. Same analysis as for soliton regime (right half) can be applied to left half of Sagdeev potential.

and moves to the right, it will reach a maximum at some Φ_m where Ψ crosses zero and Φ will be reflected and return to zero and stay there. This corresponds to the soliton solution. For the sheath plasma problem that we consider in this chapter, the potential Φ is always negative. It starts at zero in the bulk and stops at some negative value when it reaches the boundary. This negative value can be a fixed boundary potential or the floating potential which depends on the electron temperature.

7.4 Perturbative Solutions to Sheath Oscillations

For the transverse stability analysis, we look for a perturbative solution to the full set of equations. The wave vector k is in the direction perpendicular to z (in the x, y-plane). U, N, Φ are independent of x, y and t.

Here, $k^2 \sim \omega^2 \ll \omega$ is assumed. We have, thereby, restricted ourselves to considering long-wavelengths, low-frequency perturbations.

All parameters are expanded to third order

$$u = u_1 + u_2 + u_3, \tag{7.12}$$

$$n = n_1 + n_2 + n_3, \tag{7.13}$$

$$\phi = \phi_1 + \phi_2 + \phi_3. \tag{7.14}$$

The dynamics for the perturbations are written as follows:

$$-i\omega n + \frac{\partial}{\partial z}(Un + Nu) = 0, \tag{7.15}$$

$$-i\omega u + \frac{\partial}{\partial z}(Uu + \phi) = 0, \tag{7.16}$$

$$\frac{\partial^2 \psi}{\partial z^2} - \exp(\Phi)\psi + n - k^2\psi = 0. \tag{7.17}$$

In the following, we the analytic solutions, that we find for the first two orders, are given. First order:

$$\frac{\partial}{\partial z}(Un_1 + Nu_1) = 0, \tag{7.18}$$

$$\frac{\partial}{\partial z}(Uu_1 + \phi_1) = 0, \tag{7.19}$$

$$\frac{\partial^2 \phi_1}{\partial z^2} - \exp(\Phi)\phi_1 + n_1 = 0. \tag{7.20}$$

This system can be solved exactly.

$$u_1 = -\frac{\phi_1}{U} \qquad n_1 = \frac{N}{U^2}\phi_1, \tag{7.21}$$

$$\frac{\partial \phi_1}{\partial z^2} - \left(\exp(\Phi) - \frac{N}{U^2}\right)\phi_1 = 0, \tag{7.22}$$

with the solutions:

$$\phi_1 = \Phi_z \qquad u_1 = -\frac{\Phi_z}{U} \qquad n_1 = \frac{N}{U^2}\Phi_z. \tag{7.23}$$

Second order

$$\frac{\partial}{\partial z}\left(Un_2 + Nu_2\right) = i\omega\frac{N}{U^2}\Phi_z = i\omega\frac{\partial}{\partial z}\frac{1}{\sqrt{1-\frac{2\Phi}{a^2}}} = i\omega\frac{\partial N}{\partial z}, \tag{7.24}$$

$$\frac{\partial}{\partial z}\left(Uu_2 + \phi_2\right) = -i\omega\frac{\Phi_z}{U} = i\omega\frac{\partial U}{\partial z}, \tag{7.25}$$

$$\frac{\partial^2 \phi_2}{\partial z^2} - \exp(\Phi)\phi_2 + n_2 = 0. \tag{7.26}$$

Solving this system leads to:

$$u_2 = -\frac{\phi_2}{U} + i\omega\frac{U-a}{U}, \qquad n_2 = \frac{N}{U^2}\phi_2 + i\omega\frac{N}{U^2}\frac{2\Phi}{a}, \tag{7.27}$$

$$\frac{\partial \phi_2}{\partial z^2} - \left(\exp(\Phi) - \frac{N}{U^2}\right)\phi_2 = -i\omega\frac{N}{U^2}\frac{2\Phi}{a}. \tag{7.28}$$

Again, an exact solutions can be written down:

$$\phi_2 = i\omega\Phi_a, \qquad u_2 = -i\omega\frac{\Phi_a}{U} + i\omega\frac{U-a}{U}, \qquad n_2 = i\omega\frac{N}{U^2}\Phi_a + i\omega\frac{N}{U^2}\frac{2\Phi}{a}. \tag{7.29}$$

To find a dispersion relation $\omega(k)$ an expansion to third order is necessary. This introduces a term $\sim k^2$.

$$\frac{\partial}{\partial z}\left(Un_3 + Nu_3\right) = i\omega\frac{N}{U^2}\Phi_z = -\omega^2\frac{N}{U^2}\left(\Phi_a + \frac{2\Phi}{a}\right), \tag{7.30}$$

$$\frac{\partial}{\partial z}\left(Uu_3 + \phi_3\right) = -\frac{\omega^2}{U}\left(U - a - \Phi_a\right), \tag{7.31}$$

$$\frac{\partial^2\phi_3}{\partial z^2} - \exp(\Phi)\phi_3 + n = -k^2\Phi_z. \tag{7.32}$$

As we cannot find analytic solutions at this order, we write down the solutions in integral forms:

$$u_3 = -\frac{\phi_3}{U} + \frac{\omega^2}{U}\int_z^\infty \frac{U - a - \Phi_a}{U}dz, \tag{7.33}$$

$$n_3 = \frac{N}{U^2}\phi_3 - \frac{N\omega^2}{U^2}\int_z^\infty \frac{U - a - \Phi_a}{U}dz + \frac{\omega^2}{U}\int_z^\infty \frac{N}{U^2}\left(\Phi_a + \frac{2\Phi}{a}\right)dz, \tag{7.34}$$

$$\frac{\partial^2\phi_3}{\partial z^2} - \left(\exp(\Phi) - \frac{N}{U^2}\right)\phi_3 = -k^2\Phi_z + h(z), \tag{7.35}$$

where

$$h(z) = +\frac{N\omega^2}{U^2}\int_z^\infty \frac{U-a-\Phi_a}{U}dz - \frac{\omega^2}{U}\int_z^\infty \frac{N}{U^2}\left(\Phi_a + \frac{2\Phi}{a}\right)dz. \quad (7.36)$$

Earlier, we identified Φ_z as a solution of the homogeneous Equation (7.35). Substituting the Ansatz $\phi_3 = \Phi_z Z$ into (7.35), we obtain

$$\Phi_z Z_{zz} + 2\Phi_{zz}Z_z = h(z) - k^2\Phi_z, \quad (7.37)$$

or

$$\frac{d}{dz}(\Phi_z^2 Z_z) = h(z)\Phi_z - k^2\Phi_z^2. \quad (7.38)$$

After integrating, solving for Z and multiplying by Φ_z we can write down a general solution to Equation (7.35)

$$\phi_3 = C_1\Phi_z + C_2\Phi_z\int_z^\infty \Phi_z^{-2}dz - \Phi_z\int_z^\infty \Phi_{z'}^{-2}dz'\int_{z'}^\infty \left(h(z'')\Phi_{z''} - k^2\Phi_{z''}^2\right)dz''. \quad (7.39)$$

7.5 Stability of Transverse Oscillations in a Simple Sheath

In this section, we outline the steps of the stability analysis, which is done in analogy to the one performed within the Kadomtsev-Petviashvili equation [70]. Equation (7.35) can be written as

$$L\phi_3 = -k^2\Phi_z + h(\Phi). \quad (7.40)$$

This equation is inhomogeneous and, in general, does not have finite solutions for arbitrary terms on the right-hand side. After multiplying by Φ_z, a solution to the homogeneous equation, and integrating over z, the left-hand side vanishes. The right-hand side then yields a dispersion relation for small transverse oscillations.

$$\int_0^\infty dz \left(-k^2\Phi_z + h(z)\right)\Phi_z = 0, \tag{7.41}$$

which can be transformed into an integral in terms of Φ with $d\Phi = \Phi_z dz$ and $\Phi(\infty) = 0$ and $\Phi(0) = \phi_0$,

$$\int_{\phi_0}^0 d\Phi \left(-k^2\Phi_z + h(\Phi)\right) = 0, \tag{7.42}$$

where $h(\Phi)$ is proportional to ω^2.

7.5.1 Solving for the Dispersion $\omega(k)$

To determine $\omega(k)$, we first numerically solve Poisson equation for the stationary potential Φ. The boundary conditions used for the numerical solution are $\Phi(z = 0) = \Phi_0$ and $\Phi(z = z_{max}) = 0$, where z_{max} is a value chosen sufficiently large, so that variation of it does not change the solution significantly. Then, Equation (7.42) is integrated and solved for $v^2 = \omega^2/k^2$.

It turns out that, for positive ions, the dispersion is always positive and therefore stable. Figure 7.2 shows the phase velocity as a function of the Mach number a. The solution suggests that in this simple configuration the phase velocity of transverse oscillations is approximately proportional

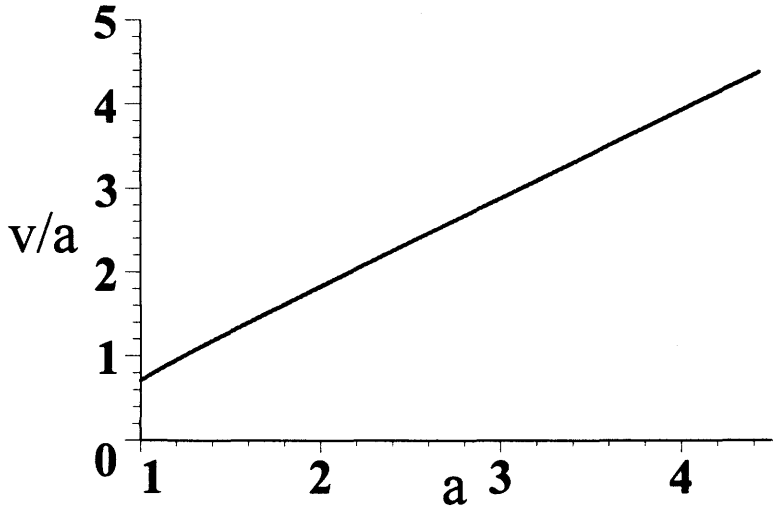

Figure 7.2 Phase velocity in Mach numbers for single ion species and single electron species.

to a^2, i.e. $\omega/k \propto a^2$, and always stable.

7.6 Double Layer with Two Boltzmann Species

As a simple extension of the model a second electron species is introduced into the system. In an ionospheric context these may originate from higher regions traveling down earth magnetic field lines into regimes with colder electrons. It may also be a simple approximation to the situation in laser heated plasmas, where a small group of very fast electrons travel ahead of the heat front into colder plasma regions.

With the second electron species, which can also be expressed by a Boltzmann distribution, two additional parameters are added to the system. One is the relative temperature T between the two electron species, and the other is the density n with respect to the ion background density so as to

maintain quasineutrality. The ion fluid equations remain the same and the only change is to Poisson's equation

$$\Delta\Phi = n\exp(\Phi) + (1-n)\exp\left(\frac{\Phi}{T}\right) - N. \tag{7.43}$$

The change to the Sagdeev potential follows directly. For certain combinations of the parameters a, n, T, so-called double-layer solutions are possible. The Sagdeev potential for a specific double-layer is shown in Figure 7.3.

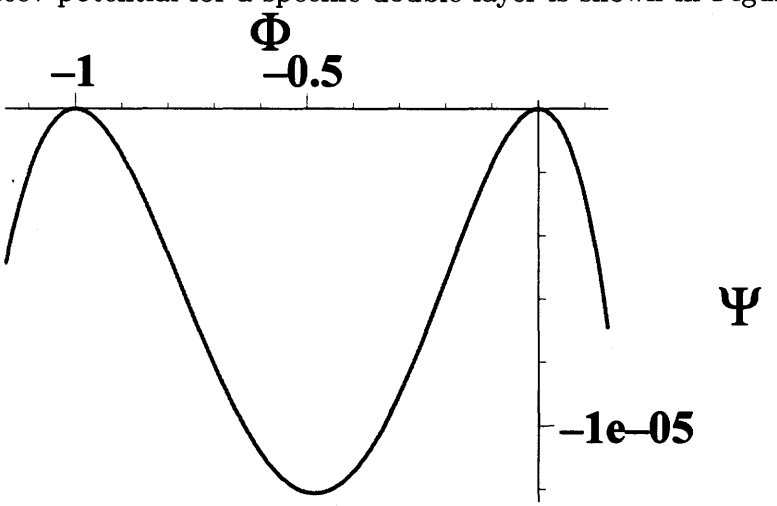

Figure 7.3 For two Boltzmann species supersonic double layer become possible with $a = 4.12 \quad T = 19.45$.

If we invoke the analogy of Φ moving in the potential Ψ again the following solution emerges. Φ starts at zero in the bulk and moves to a negative potential ($\Phi = -1$) at the other boundary of the system where it remains because of zero derivative in Ψ. This is know as the double-layer. With the aforementioned change in the Poisson's equation, the procedure for the stability analysis can be repeated analogously to the single electron

species case. It should be noted that, for a double-layer potential to occur, large sheath regions have to be used. A typical sheath for a single electron species is just a few λ_D wide, whereas a double layer only occurs if we allow for a transition region of several tens to few hundreds of λ_D. As a increases the solution smoothly transforms into a normal sheath potential. This occurs within a fractional change of a. Figure 7.4 shows the solution

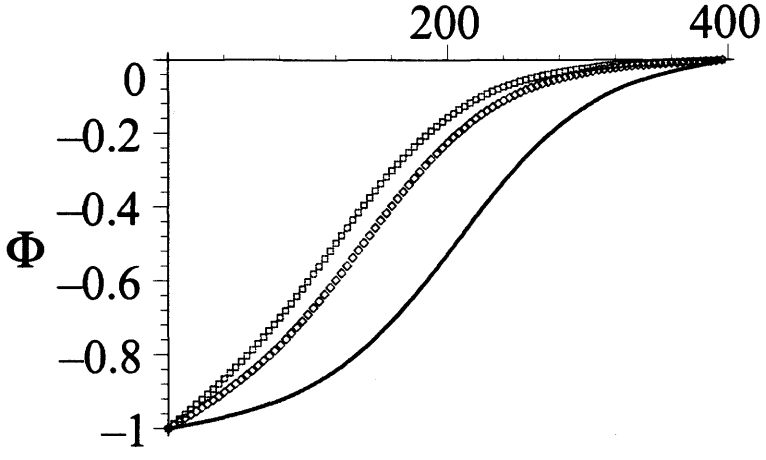

Figure 7.4 The transition to a double layer $a = 4, 4.0002, 4.0004$ (solid, diamonds, squares) is shown. The double layer solution exists for $a = 4$.

to Poisson equation for the stationary potential for three values of a. The value $a = 4$ corresponds to the exact double layer solution. We can see that the transition to a simple sheath happens for a fractional change in a of only 10^{-4}.

7.6.1 Dispersion for Two Boltzmann Species

The dispersion relation is again computed numerically for different values of a. For comparison, it is solved for a different relation of the two

electron species where only simple sheath solutions exist. Figure 7.5 shows the phase velocities for the two cases. It should be noted that for two electron species also the Bohm criterion for the occurrence of a sheath is modified [73]. For the case illustrated by the top dark line no solution exists for $a < 4$ due to that Bohm criterion.

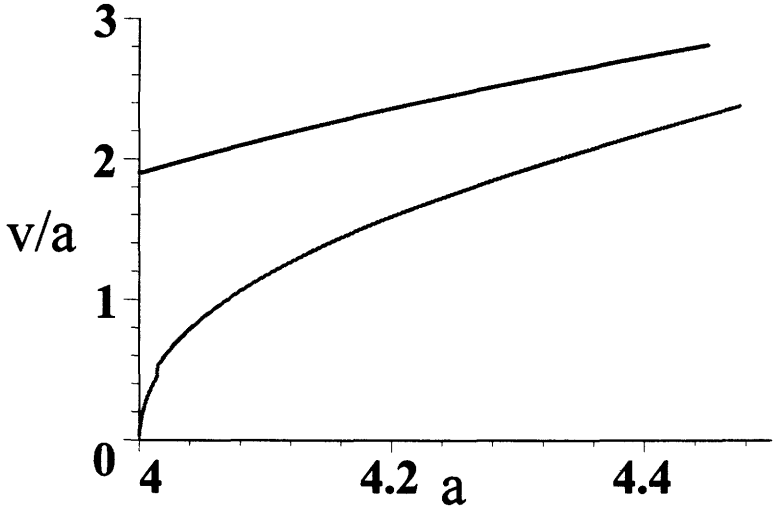

Figure 7.5 Phase velocities for density at which double layer occurs at $a = 4$ (gray, bottom line) and twice that density of colder electrons (black, top line).

Close to the double layer solution $a = 4$ stable transverse oscillations persist, but with phase velocities much slower than the typical ion sound velocity in the bulk. This indicates the possibility of oscillation phenomena that occur on time scales even slower than the ion sound waves.

7.7 Conclusions

In conclusion, we have found the dispersion for transverse ion oscillations in a sheath with one and two electron species. For two electron species double layers can occur which are associated with extreme low frequency oscillations of the ion acoustic type. A kinetic analysis is necessary to determine if these oscillations can persist in realistic conditions, when ion Landau damping might diminish all oscillations that can occur within this model.

8. Conclusions

One of the crucial aspects of plasma physics is the problem of transport of matter, momentum and energy in a plasma subject to temperature, pressure and velocity gradients. In particular, in fusion plasmas one needs to understand the mechanisms of transport of energy and matter from the region of the production or deposition of energy towards the boundaries of the plasmas. In laser plasma experiments the deposition of laser energy into small regions of the plasma leads to large temperature and pressure gradients. Powerful simulation codes, that solve hydrodynamic equations, have been developed to understand the evolution of laser plasma experiment in complex geometries. Recent works on transport in typical experimental parameters have shown that classical, local transport theory is not sufficient in describing the observed heat fluxes. Development of kinetic codes to study transport phenomena and other long time scale evolution is still an ongoing research (e.g. [17, 24]). One of the possible approaches are particle-in-cell (PIC) simulations, which we have chosen because of the straightforward adaptability to different geometries.

In the present thesis, we have developed a PIC simulation model QNPIC, that allows the study of long time phenomena in fully ionized plasmas. In QNPIC we employ an algorithm to determine the electric field E that is based on quasineutrality [30]. This is the first time quasineutrality condi-

tion is used in PIC to study transport phenomena. The advantages are the use of large time steps and the low noise compared to a standard Poisson solver at quasineutral conditions. Electron-electron and electron-ion collisions are included by a Monte-Carlo binary collision model based on work by Takizuka and Abe [26, 27]. Another novel feature to our PIC simulations, that was utilized to study collisional heating due to high-frequency laser light, is using a time averaged (over the laser period) kinetic equation. We have derived a Langevin equation corresponding to the Fokker-Planck equation. This Langevin equation allows inclusion of the time averaged effect of collisional heating in QNPIC [74]. The correct heating rate is reproduced and, additionally, the evolution of the distribution function towards a non-Maxwellian shape is found. The main advantage for this approach to represent heating in PIC is the acceleration of the simulation. The laser frequency, usually one of the smallest time scales, does not have to be resolved in this method. This makes heating and transport studies for realistic experimental parameters in PIC feasible.

We studied the absorption of laser light and the evolution of the distribution in homogeneous plasmas. Future work in the use of homogeneous plasma simulations should include careful studies of the absorption coefficient and the decay of the laser intensity within the plasma due to absorption. By using QNPIC, we verified a self-consistent nonlocal model of heat transport by electrons [16] for small temperature perturbations. We suggest a nonlinear version by allowing a spatial dependence in the collisional mean free path. The new nonlocal kernel, that describes heat conduction in temperature gradients with constant density and the initial electron veloc-

ity distribution (EDF) near Maxwellian, is successfully tested in QNPIC. Similarly to the linear theory it does not depend on any fitting parameter like other proposed nonlocal heat flux models [14, 15, 75]. We also use QNPIC to study the evolution of an inhomogeneously heated plasma towards a quasistationary temperature profile. The relation between heat flux and temperature gradient is found to be close to the classical results ($\propto x^{2/7}$) but with a significantly reduced heat flux. Continuing work will investigate the effect of non-Maxwellian EDF due to heating on the heat flux. Also allowing for density gradients we examined the influence of density gradients on the transport processes. We have obtained quasistationary states where ion motion results in inhomogeneous temperature and density profiles. However, a detailed study on the heat flux under these conditions remains to be done.

Correct ion sound wave dynamics within QNPIC have been verified. We have also confirmed the effects of ion turbulence on transport and heating. To this end, we have studied two-stream instabilities under various conditions. QNPIC is proven to be a useful tool to study ion plasma dynamics that include collisional effects ($e-e$ and $e-i$), collisional heating and wave-particle interactions. The implications for laser plasma experiments are addressed in preliminary studies on the long-known return current instability (RCI), that occurs in electron temperature gradients. The ion turbulence caused by RCI is thought to be the cause of electron heat flux inhibition, but experimental or simulation studies were still lacking. We have demonstrated that in realistic conditions the RCI is observed. Detailed numerical analysis of the instability and its effect on the heat flux

will be the subject of future work.

In the context of ion dynamics we have derived closure relations for the ion hydrodynamic equations. These closures are obtained from a Chapman-Enskog like procedure from the kinetic equation. To include collisional effects we have considered the ion-ion collision operator and derived the closure coefficients with a collisional limit corresponding to a 21 -moment Grad results. The closures are therefore self-consistent from the collisionless regime dominated by wave-particle interactions to the collisional regime where interparticle collisions dominate. We calculated explicit expressions for the closures in the approximation $ZT_e \gg T_i$, which is relevant to typical laser plasmas.

For ion oscillations transverse to the direction of the gradient of a non-linear inhomogeneity (in density) we have applied a stability analysis by Kadomtsev-Petviashvili [70] that was originally developed for solitons. We have demonstrated the applicability of this method to a cold ion sheath and to a double layer. We obtained the double layer solution by introducing a second electron distribution with a temperature different to the first one. For the double layer case we have shown that the phase speed of the transverse waves approaches zero as the exact double layer solution is reached.

References

[1] C. Yamanaka. *Handbook of Plasma Physics Vol3: Physics of Laser Plasma*, chapter Laser Plasma and Inertial Confinement Fusion, page 1. Elsevier Science Publishers B. V., 1991.

[2] V. N. Shlyaptsev, J. Dunn, K. B. Fournier, S. Moon, A. L. Osterheld, J. J. Rocca, F. Detering, W. Rozmus, F. Alouani-Bibi, J. P. Matte, H. Fiedorowicz A. Bartnik, and M. Kanouff. *ref. proc. of IFSA, Kyoto*, 2001.

[3] V. N. Shlyaptsev, J. Dunn, S. Moon, A. L. Osterheld, J. J. Rocca, F. Detering, W. Rozmus, J. P. Matte, A. Bartnik, and M. Kanouff. *SPIE proc.*, 14:4505, 2001.

[4] A. B. Langdon. Nonlinear inverse bremsstrahlung and heated-electron distributions. *Phys. Rev. Lett.*, 44:575, 1980.

[5] J. P. Matte, M. Lamoureux, C. Moller, R. Y. Yin, J. Delettrez, J. Virmont, and T. W. Johnston. Non-maxwellian electron distributions and continuum x-ray emission in inverse bremsstrahlung heated plasmas. *Plasma Phys. Contr. Fusion*, 30:1665, 1988.

[6] A. V. Brantov, V. Yu. Bychenkov, V. T. Tikhonchuk, and W. Rozmus. Nonlocal plasma electron hydrodynamics. *JETP*, 83(4):716, 1996.

[7] A. V. Brantov, V. Yu. Bychenkov, V. T. Tikhonchuk, and W. Rozmus.

Nonlocal electron transport in laser heated plasmas. *Phys. Plasmas*, 5(7):2742, 1998.

[8] A. V. Brantov, V. Yu. Bychenkov, and W. Rozmus. *Phys. of Plasmas*, 8(8):3558, 2001.

[9] H. de Kluiver, N. F. Perepelkin, and A. Hirose. *Physics Reports*, 199(6):281, 1991.

[10] J. M. Dawson. Particle simulation of plasmas. *Rev. Mod. Phys.*, 55(2):403–445, 1983.

[11] C. K. Birdsall and A. B. Langdon. *Plasma Physics via Computer Simulation.* IoP, 1998.

[12] L. Spitzer Jr. and R. Härm. *Phys. Rev.*, 89:977, 1953.

[13] S. I. Braginskii. *Reviews of Plasma Physics*, volume I, page 210. Consultants Bureau, New York, 1965.

[14] J. R. Albritton, E. A. Williams, I. B. Bernstein, and K. P. Swartz. Nonlocal electron heat transport by not quite maxwell-boltzmann distributions. *Phys. Rev. Lett.*, 57:1887, 1986.

[15] J. F. Luciani, P. Mora, and J. Virmont. *Phys. Rev. Lett.*, 51:1664, 1983.

[16] V. Yu. Bychenkov, V. N. Novikov, and V. T. Tikhonchuk. Theory of nonlocal transport for small perturbations in a plasma. *Sov. Phys. JETP*, 87:916, 1998.

[17] O. V. Batishchev, V. Yu. Bychenkov, F. Detering, W. Rozmus, R. Sydora, C. E. Capjack, and V. N. Novikov. *Phys. Plasmas*, 9:2302, 2002.

[18] V. T. Tikhonchuk, W. Rozmus, V. Yu. Bychenkov, C. E. Capjack, and E. Epperlein. Return current instability in laser heated plasmas. *Phys. Plasmas*, 2:4169, 1995.

[19] Z. Chang and J. D. Callen. *Phys. Fluids B*, 4:1167, 1992.

[20] G. W. Hammett and F. W. Perkins. Fluid moment models for landau damping with applications to the ion-temperature-gradient instability. *Phys. Rev. Lett.*, 64(25):3019–3022, 1990.

[21] J. Zheng, C. X. Yu, and Z. J. Zheng. The dynamic form factor for ion-collisional plasmas. *Phys. Plasmas*, 6(2):435, 1999.

[22] A. A. Batishcheva, O. V. Batishchev, M. M. Shoucri, S. I. Krasheninnikov, P. J. Catta, I. P. Shkarofsky, and D. J. Sigmar. *Phys. Plasmas*, 3:1634, 1996.

[23] V. N. Novikov, V. Yu. Bychenkov, and V. T. Tikhonchuk. *in Abstracts of the XXVIII Zvenigorod Conference on Plasma Physics and Controlled Nuclear Fusion, Zvenigorod, Russia*, (1923), 2001. in Russian.

[24] S. Brunner, E. Valeo, and J. A. Krommes. Collisional delta-f scheme with evolving background for transport time scale simulations. *Phys. Plasmas*, 6(12):4504, 1999.

[25] S. Brunner, E. Valeo, and J. A. Krommes. Linear delta-f simulations of nonlocal electron heat transport. *Phys. Plasmas*, 7:2810, 2000.

[26] T. Takizuka and H. Abe. A binary collision model for plasma simulation with a particle code. *J. Comput. Phys.*, 25:205, 1977.

[27] S. Ma, R. Sydora, and J. M. Dawson. Binary collision model in gyrokinetic simulation plasmas. *Computer Phys. Commun.*, 77:190, 1993.

[28] C. Kirkby. Master's thesis, University of Alberta, 2001.

[29] F. F. Chen. *Introduction to Plasma Physics.* Plenum, New York, 1974.

[30] G. Joyce, M. Lampe, S. P. Slinker, and W. Manheimer. Electrostatic particle-in-cell simulation technique for quasineutral plasma. *J. Comput. Phys.*, 138:540, 1997.

[31] K. Mima and K. Nishikawa. *in Basic Plasma Physics II*, page ch. 6.5, 1984.

[32] R. D. Jones and K. Lee. *Phys. Fluids*, 25:2307, 1982.

[33] R. Balescu. Heating of electrons and ions by inverse bremsstrahlung absorption: a self-similar state of the plasma. *J. Plasma Physics*, 27:553, 1982.

[34] Yu L. Klimontovich. *Kinetic Theory of Nonideal Gases & Nonideal Plasmas.* Pergamon Press, 1982.

[35] I. P. Shkarofsky, T. W. Johnston, and M. P. Backynski. *The Particle Kinetics of Plasmas.* Addison-Wesley, Mass., 1966.

[36] E. Fourkal, V. Yu. Bychenkov, W. Rozmus, R. Sydora, C. Kirkby, and C. E. Capjack. *Phys. Plasmas*, 8:550, 2001.

[37] C. W. Gardiner. *Handbook of Stochastic Methods.* Springer, 1994.

[38] van Kampen. *Stochastic Processes.* North-Holland, 1981.

[39] W. M. Manheimer, M. Lampe, and G. Joyce. Langevin representation of coulomb collisions in pic simulations. *J. Comput. Phys.*, 138:563–584, 1997.

[40] Y. Kato, K. Mima, N. Miyanaga, S. Arinaga, M. Nakatsuka, and C. Yamanaka. *Phys. Rev. Lett.*, 53:1057, 1984.

[41] R. H. Lehmberg and S. P. Obenschain. *Opt. Commun.*, 46:27, 1983.

[42] B. B. Afeyan, A. E. Chou, J. P. Matte, R. P. Town, and W. J. Kruer. *Phys. Rev. Lett.*, 80:2322, 1998.

[43] V. K. Senecha, A. V. Brantov, V. Yu Bychnekov, and V. T. Tikhonchuk. Temperature relaxation in hot spots in a laser-produced plasma. *Phys. Rev. E*, 57:978, 1998.

[44] A. R. Bell, R. G. Evans, and D. J. Nicholas. *Phys. Rev. Lett.*, 46:243, 1981.

[45] E. M. Epperlein and R. W. Short. Nonlocal heat transport effects on the filamentation of light in plasmas. *Phys. Fluids B*, 4(7):2211, 1992.

[46] S. I. Krasheninnikov. *Sov. Phys. JETP*, 67:2484, 1988.

[47] G. Murtazs, M. Mirza, and M. S. Qaisar. *Phys. Lett.*, 144:164, 1990.

[48] M. K. Prasad and D. S. Kershaw. Nonviability of some nonlocal transport modeling. *Phys. Fluids B*, 1(12):2430, 1989.

[49] M. K. Prasad and D. S. Kershaw. Stable solutions of nonlocal electron heat transport equations. *Phys. Fluids B*, 3(11):3087, 1991.

[50] V. Yu. Bychenkov, V. P. Silin, and S. A. Uryupin. Ion-acoustic turbulence and anomalous transport. *Phys. Reports*, 164(3):119–215, 1988.

[51] A. A. Galeev and R. Z. Sagdeev. volume 2 of *Handbook of Plasma Physics*, chapter 4.1 and 4.2. North-Holland, Amsterdam, 1983.

[52] R. Sydora. PhD thesis, University of Texas at Austin, 1986.

[53] E. Ahedo and V. Lapuerta. *Phys. Plasmas*, 8:3873, 2001.

[54] V. Lapuerta and E. Ahedo. *Phys. Plasmas*, 9:1513, 2002.

[55] R. J. Goldston and P. H. Rutherford. *Introduction to plasma physics.* Philadelphia, PA : Institute of Physics Pub., 1995.

[56] O. Buneman. *Phys. Rev.*, 115:503, 1959.

[57] O. Ishihara, A. Hirose, and A. B. Langdon. *Phys. Rev. Lett.*, 44(21):1404, 1980.

[58] O. Ishihara, A. Hirose, and A. B. Langdon. *Phys. Fluids*, 24(3):452, 1981.

[59] O. Ishihara, A. Hirose, and A. B. Langdon. *Phys. Fluids*, 25(4):610, 1982.

[60] A. B. Mikhailovskii. *Theory of Plasma Instabilities*, volume 1. Consultants Bureau, New York, 1974.

[61] J. Zheng and C. X. Yu. Ion-collisional effects on ion-acoustic waves: an eigenvalue technique via moment expansion. *Plasma Phys. Control Fusion*, 42:435–441, 2000.

[62] S. Chapman and T. G. Cowling. *The Mathematical Theory of Non-uniform Gases.* Cambridge Univ. Press, Cambridge, 1952.

[63] H. Grad. *Pure & Appl. Math.*, 2:311, 1949.

[64] A. B. Mikhailovskii and V. S. Tsypin. *Beitr. Plasmaphys.*, 24(4):335, 1984.

[65] R. Balescu. *Transport Processes in Plasmas Vol.1.* North-Holland, 1988.

[66] M. N. Rosenbluth, W. M. MacDonald, and D. L. Judd. *Phys. Rev.*, page 107, 1957.

[67] M. D. Tracy, E. A. Williams, K. G. Estabrook, J. S. de Groot, and S. M. Cameron. Eigenvalue solution for the ion-collisional effects on ion-acoustic and entropy waves. *Phys. Fluids B*, 5(5):1430–1439, 1993.

[68] B. D. Fried and S. D. Conte. *The Plasma Dispersion Function.* Academic Press, 1961.

[69] W. Rozmus, M. Casanova, D. Pesme, A. Heron, and J.-C. Adam. *Phys. Fluids B*, 4(3):576, 1992.

[70] V. Petviashvili and O. Pokhotelov. *Solitary Waves in Plasmas and in the Atmosphere.* Gordon and Breach Science Publishers, 1991.

[71] R. Roychoudhury and S. Bhattacharyya. *J. Plasma Physics*, 42:353, 1989.

[72] F. Verheest and M. A. Hellberg. *J. Plasma Physics*, 57:465, 1997.

[73] K.-U. Riemann. *J. Phys. D Appl. Phys.*, 24:493, 1991.

[74] F. Detering, V. Yu. Bychenkov, W. Rozmus, R. Sydora, and C. E. Capjack. *Comput. Phys. Comm.*, 143:48, 2002.

[75] E. M. Epperlein and R. W. Short. A practical nonlocal model for electron heat transport in laser plasmas. *Phys. Fluids B*, 3(11):3092, 1991.

A. Closure Moments

A.1 Integrals

The following integrals occur in the collisionless parts when taking the moments. They can be expressed in terms of the plasma dispersion function and its derivative

$$Z'(\xi) = -2(1 + \xi Z(\xi)). \tag{A.1}$$

The integrals $G_i(\xi)$ are defined as

$$G_i(\xi) = \int_0^\infty f_m(v_\parallel) \frac{(v_\parallel)^i}{\xi - v_\parallel}, \tag{A.2}$$

and they are

$$G_0(\xi) = -\frac{Z(\xi)}{\sqrt{2}} \tag{A.3}$$

$$G_1(\xi) = \frac{Z'(\xi)}{2} \tag{A.4}$$

$$G_2(\xi) = \xi Z'(\xi)\sqrt{2} \tag{A.5}$$

$$G_3(\xi) = -(1 - \xi^2 Z'(\xi)) \tag{A.6}$$

$$G_4(\xi) = -\xi(1 - \xi^2 Z'(\xi))\sqrt{2} \tag{A.7}$$

$$G_5(\xi) = -(3 + 2\xi^2 - 2\xi^4 Z'(\xi)) \tag{A.8}$$

$$G_6(\xi) = -\xi(3 + 2\xi^2 - 2\xi^4 Z'(\xi))\sqrt{2} \tag{A.9}$$

$$G_7(\xi) = -(15 + 6\xi^2 + 4\xi^4 - 4\xi^6 Z'(\xi)) \tag{A.10}$$

$$G_8(\xi) = -\xi(15 + 6\xi^2 + 4\xi^4 - 4\xi^6 Z'(\xi))\sqrt{2} \tag{A.11}$$

A.1.1 Collisionless Moments

The collisionless contributions to the moments are given in the following. M_{xy} is defined as taking the x moment (π, π^*, q or q^*) as defined in section

6.5 on the part proportional to $y = u_{||}, \nabla_{||}T, \pi, q$ in Equation (6.29).

$$M_{\pi u} = \frac{2}{3}(G_4 - 2G_2 + 2G_0) \tag{A.12}$$

$$M_{\pi T} = \frac{1}{2}(G_5 - 4G_3 + G_1) \tag{A.13}$$

$$M_{\pi^* u} = \frac{2}{3}(G_6 - 7G_4 + 8G_2 - 2G_0) \tag{A.14}$$

$$M_{\pi^* T} = \frac{1}{2}(G_7 - 9G_5 + 23G_3 - 11G_1) \tag{A.15}$$

$$M_{\pi\pi} = -\frac{2}{3}(G_3 - G_1) \tag{A.16}$$

$$M_{\pi q} = -\frac{1}{3}(G_4 - 2G_2 - G_0) \tag{A.17}$$

$$M_{\pi^* \pi} = -\frac{2}{3}(G_5 - 6G_3 + 3G_1) \tag{A.18}$$

$$M_{\pi^* q} = -\frac{1}{3}(G_6 - 7G_4 + 11G_2 - 6G_0) \tag{A.19}$$

$$M_{qu} = \frac{2}{3}(G_5 - 4G_3 + G_1) \tag{A.20}$$

$$M_{qT} = \frac{1}{2}(G_6 - 6G_4 + 13G_2) \tag{A.21}$$

$$M_{q^* u} = \frac{1}{3}(G_7 - 9G_5 + 21G_3 - 3G_1) \tag{A.22}$$

$$M_{q^* T} = \frac{1}{4}(G_8 - 13G_6 + 53G_4 - 69G_2) \tag{A.23}$$

$$M_{q\pi} = -\frac{2}{3}(G_4 - 3G_2) \tag{A.24}$$

$$M_{qq} = -\frac{1}{3}(G_5 - 4G_3 + 7G_1) \tag{A.25}$$

$$M_{q^* \pi} = -\frac{2}{3}\left(\frac{1}{2}G_6 - 6G_4 + \frac{15}{2}G_2\right) \tag{A.26}$$

$$M_{q^* q} = -\frac{1}{6}(G_7 - 9G_5 + 33G_3 - 39G_1) \tag{A.27}$$

A.2 Collisional Moments

For short notation the moments M_i of the distribution function are defined

$$M_i = \int_{\xi}^{\infty} f_m(v)^2 v^i dv \tag{A.28}$$

where $i = -3..5$ typically and the Maxwellian is

$$f_m(v) = \sqrt{\frac{2}{\pi}} \exp\left(\frac{-v^2}{2}\right). \tag{A.29}$$

In the collisional moments the following integrals occur frequently so we define the short form MP_i

$$MP_i = \int_{\xi/\sqrt{2}}^{\infty} f_m(v)\Phi\left(\frac{v}{\sqrt{2}}\right) v^i dv \tag{A.30}$$

where $i = -4..6$ typically and Φ is the error function. M_{xy} is defined as before where this time the integrals are only over the collisional parts of equation (6.29).

$$\begin{aligned} M_{\pi\pi} = -\frac{\Gamma_{ii}}{3k}\Bigg[& \left(\frac{3}{10\xi^2\sqrt{\pi}}\right) + \\ & + i\pi\xi\Big(36\xi^4 M_{-3} - 24\xi^2 M_{-1} + 4M_1 \\ & + 9\xi^4 MP_{-2} - 6\xi^2 MP_0 + MP_2 \\ & - 36\xi^4 MP_{-4} + 24\xi^2 MP_{-2} - 4MP_0\Big)\Bigg] \end{aligned} \tag{A.31}$$

$$M_{\pi q} = -\frac{\Gamma_{ii}}{5k}\left[\left(\frac{16}{15\xi^2\sqrt{\pi}}\right)+ \right.$$
$$+ i\pi\Big(15\xi^2 M_{-1} - 5M_1 + 3\xi^2 MP_0 - MP_2 \qquad \text{(A.32)}$$
$$\left. - 15\xi^2 MP_{-2} + 5MP_0\Big)\right]$$

$$M_{q\pi} = -\frac{2\Gamma_{ii}}{5k}\left[\left(\frac{4}{5\xi\sqrt{\pi}}\right)+ \right.$$
$$+ i\pi\xi^2\Big(12\xi^2 M_{-1} - 4M_1 - 60\xi^2 M_{-3}$$
$$+ 20M_{-1} + 3\xi^2 MP_0 - MP_2 - 15\xi^2 MP_{-2} + 5MP_0 \qquad \text{(A.33)}$$
$$\left. - 12\xi^2 MP_{-2} + 4MP_0 + 60\xi^2 MP_{-4} - 20MP_{-2}\Big)\right]$$

$$M_{qq} = -\frac{2\Gamma_{ii}}{5k}\left[\left(\frac{4}{3\xi\sqrt{\pi}}\right)+ \right.$$
$$\left. + i\pi\xi^2\Big(5M_1 - 25M_{-1} + MP_2 - 10MP_0 + 25MP_{-2}\Big)\right] \qquad \text{(A.34)}$$

$$M_{\pi^*\pi} = -\frac{\Gamma_{ii}}{3k}\left[\left(\frac{3}{20\xi\sqrt{\pi}}\right)+ \right.$$
$$+ i\pi\xi\Big(-252\xi^4 M_{-3} + \left(168\xi^2 + 36\xi^4\right) M_{-1}$$
$$- \left(28 + 24\xi^2\right) M_1 + 4M_3 + 252\xi^4 MP_{-4} \qquad \text{(A.35)}$$
$$- \left(99\xi^4 + 168\xi^2\right) MP_{-2} + \left(9\xi^4 + 66\xi^2 + 28\right) MP_0$$
$$\left. - \left(6\xi^2 + 11\right) MP_2 + MP_4\Big)\right]$$

$$
\begin{aligned}
M_{\pi^* q} = -\frac{\Gamma_{ii}}{5k}\Bigg[& \left(\frac{64}{15\xi^2\sqrt{\pi}}\right) + \\
& + i\pi\xi\Big(-105\xi^2 M_{-1} + \left(35 + 15\xi^2\right) M_1 \\
& - 5M_3 + 105\xi^2 MP_{-2} - \left(35 + 36\xi^2\right) MP_0 \\
& + \left(12 + 3\xi^2\right) MP_2 - MP_4\Big)\Bigg]
\end{aligned}
\tag{A.36}
$$

$$
\begin{aligned}
M_{q^* \pi} = -\frac{2\Gamma_{ii}}{3k}\Bigg[& \left(-\frac{33}{30\xi^2\sqrt{\pi}}\right) + \\
& + i\pi\xi\Big(210\xi^2 M_{-3} - \left(70 + 84\xi^2\right) M_{-1} \\
& + \left(28 + 6\xi^2\right) M_1 - 2M_3 - 210\xi^2 MP_{-4} \\
& + \left(70 + 136.5\xi^2\right) MP_{-2} - \left(45.5 + 27\xi^2\right) MP_0 \\
& + \left(9 + 1.5\xi^2\right) MP_2 - 0.5 * MP_4\Big)\Bigg]
\end{aligned}
\tag{A.37}
$$

$$
\begin{aligned}
M_{q^* q} = -\frac{2\Gamma_{ii}}{5k}\Bigg[& \left(-\frac{2}{\xi\sqrt{\pi}}\right) + \\
& + i\pi\xi^2\Big(52.5M_{-1} - 35M_1 + 2.5M_3 \\
& - 87.5MP_{-2} + 52.5MP_0 - 9.5MP_2 + 0.5MP_4\Big)\Bigg]
\end{aligned}
\tag{A.38}
$$

$$
\begin{aligned}
M_{\pi\pi^*} = -\frac{\Gamma_{ii}}{168k}\Bigg[&\left(\frac{3}{5\xi\sqrt{\pi}}\right)+ \\
&+ i\pi\Big(261\xi^4 M_{-3} - \left(174\xi^2 - 441\xi^4\right) M_{-1} \\
&+ \left(29 - 294\xi^2\right) M_1 + 49M_3 - 261\xi^4 MP_{-4} \\
&+ \left(174\xi^2 - 270\xi^4\right) MP_{-2} - \left(29 - 180\xi^2 - 45\xi^4\right) MP_0 \\
&- \left(30 + 30\xi^2\right) MP_2 + 5MP_4\Big)\Bigg]
\end{aligned}
\tag{A.39}
$$

$$
\begin{aligned}
M_{\pi q^*} = -\frac{\Gamma_{ii}}{140k}\Bigg[&\left(-\frac{32}{5\xi^2\sqrt{\pi}}\right)+ \\
&+ i\pi\xi\Big(-189\xi^2 M_{-1} + \left(63 + 105\xi^2\right) M_1 \\
&- 35M_3 + 189\xi^2 MP_{-2} - \left(63 + 108\xi^2\right) MP_0 \\
&+ MP_2\left(36 + 9\xi^2\right) - 3MP_4\Big)\Bigg]
\end{aligned}
\tag{A.40}
$$

$$
\begin{aligned}
M_{q\pi^*} = -\frac{\Gamma_{ii}}{84k}\Bigg[&\left(\frac{364}{15\xi^2\sqrt{\pi}}\right)+ \\
&+ i\pi\xi\Big(-435\xi^2 M_{-3} + M_{-1}\left(145 - 648\xi^2\right) \\
&+ M_1\left(216 + 147\xi^2\right) - 49M_3 + 435\xi^2 MP_{-4} \\
&- MP_{-2}\left(145 - 363\xi^2\right) - MP_0\left(121 + 165\xi^2\right) + MP_2\left(55 + 15\xi^2\right) - 5MP_4\Big)\Bigg]
\end{aligned}
\tag{A.41}
$$

$$M_{qq^*} = -\frac{\Gamma_{ii}}{70k}\left[\left(-\frac{8}{\xi\sqrt{\pi}}\right)+\right.$$
$$+ i\pi\xi^2\Big(315M_{-1} - 238M_1 + 35M_3 \qquad (A.42)$$
$$\left. - 315MP_{-2} + 243MP_0 - 51MP_2 + 3MP_4\Big)\right]$$

$$M_{\pi^*\pi^*} = -\frac{\Gamma_{ii}}{168k}\left[\left(\frac{561}{10\xi\sqrt{\pi}}\right)+\right.$$
$$+ i\pi\Big(-1827xi^4M_{-3} + M_{-1}\left(1218\xi^2 - 2826\xi^4\right)$$
$$+ MP_1\left(-203 + 1884\xi^2 + 441\xi^4\right) - M_3\left(314 + 294\xi^2\right) \qquad (A.43)$$
$$+ 49M_5 + 1827xi^4MP_{-4} - MP_{-2}\left(1218\xi^2 - 1629\xi^4\right)$$
$$+ MP_0\left(203 - 1086\xi^2 - 585\xi^4\right) + 5MP_6$$
$$\left. + MP_2\left(181 + 390\xi^2 + 45\xi^4\right) - MP_4\left(65 + 30\xi^2\right)\Big)\right]$$

$$M_{\pi^*q^*} = -\frac{\Gamma_{ii}}{140k}\left[\left(\frac{256}{5\xi^2\sqrt{\pi}}\right)+\right.$$
$$+ i\pi\xi\Big(1323\xi^2M_{-1} - M_1\left(441 + 924\xi^2\right)$$
$$+ M_3\left(308 + 105\xi^2\right) - 35M_5 - 1323\xi^2MP_{-2} + MP_0\left(441 + 945\xi^2\right)$$
$$\left. - MP_2\left(315 + 171\xi^2\right) + MP_4\left(57 + 9\xi^2\right) - 3MP_6\Big)\right]$$
(A.44)

$$M_{q^*\pi^*} = -\frac{\Gamma_{ii}}{84k}\left[\left(\frac{71}{3\xi^2\sqrt{\pi}}\right)+\right.$$
$$+ i\pi\xi\Big(1522.5M_{-3} - M_{-1}\left(507.5 - 1963.5\xi^2\right)$$
$$- M_1\left(654.5 + 985.5\xi^2\right) + M_3\left(328.5 + 73.5\xi^2\right) - 24.5M_5$$
$$- 1522.5\xi^2 MP_{-4} + MP_{-2}\left(507.5 - 966\xi^2\right) + MP_0\left(322 + 849\xi^2\right)$$
$$\left. - MP_2\left(283 + 150\xi^2\right) + MP_4\left(50 + 7.5\xi^2\right) - 2MP_6\Big)\right] \tag{A.45}$$

$$M_{q^*q^*} = -\frac{\Gamma_{ii}}{70k}\left[\left(\frac{60}{\xi\sqrt{\pi}}\right)+\right.$$
$$+ i\pi\xi^2\Big(1102.5M_{-1} + 1053.5M_1 - 276.5M_3 + 17.5M_5$$
$$\left. + 1102.5MP_{-2} - 1071MP_0 + 336MP_2 - 39MP_4 + 1.5MP_6\Big)\right] \tag{A.46}$$